A NOVEL CORE ANALYSIS METHOD FOR PRISMATIC HIGH TEMPERATURE GAS REACTORS

A Dissertation
Presented to
The Academic Faculty

By

Alexander J Huning

In Partial Fulfillment
Of the Requirements for the Degree
Doctorate of Philosophy in Nuclear Engineering

Georgia Institute of Technology
August 2016

A NOVEL CORE ANALYSIS METHOD FOR PRISMATIC HIGH TEMPERATURE GAS REACTORS

Approved by:

Dr. Srinivas Garimella, Chairman
George W. Woodruff School of Mechanical Engineering
Georgia Institute of Technology

Dr. Farzad Rahnema, Co-Advisor
George W. Woodruff School of Mechanical Engineering
Georgia Institute of Technology

Dr. S. Mostafa Ghiaasiaan
George W. Woodruff School of Mechanical Engineering
Georgia Institute of Technology

Dr. Thomas Fuller
School of Chemical and Bimolecular Engineering
Georgia Institute of Technology

Dr. Laurence Jacobs
George W. Woodruff School of Mechanical Engineering
Georgia Institute of Technology

Date Approved: 7/26/2016

ACKNOWLEDGEMENTS

I would like to thank my advisors Dr. Srinivas Garimella and Dr. Farzad Rahnema for giving me this opportunity to pursue graduate school and initiate my career. I am extremely grateful for their financial support, guidance, and mentoring. I am also very thankful for my Ph.D. committee who has raised valuable questions and provided advice.

I would like to thank the senior students at the Sustainable Thermal Systems Laboratory (STSL) for their guidance and helpful advice throughout graduate school. In particular, I would like to thank Alex Rattner, now Professor at Penn. State, and Brian Fronk, now Professor at Oregon State. I would also like to thank my current graduate school peers Daniel Kromer, who climbed into my same boat, and Dhruv Hoysall, who shares a very similar outlook as me.

I am very fortunate to have been part of two different research labs during my time at Georgia Tech. I believe I have experienced a very broad range of different research areas, advising styles, peer personalities, and ideas. I would like to thank all of the members of the Computational Reactor and Medical Physics Lab (CRMPL). It has been an enjoyable experience sharing our thoughts on the nuclear industry and energy politics.

Finally, I would very much like to thank my beautiful and capable wife Katie for both her financial and emotional support throughout graduate school. She is truly the only person in the world who understands me better than myself.

TABLE OF CONTENTS

LIST OF TABLES

LIST OF FIGURES

NOMENCLATURE

Symbols

as	unit cell surface area
c_P	constant pressure specific heat
ρ	density
D_H	channel hydraulic diameter
ε	surface roughness
e	fluid total energy per unit mass
f	friction factor
g	gravitational acceleration
h	heat transfer coefficient
i	fluid internal energy per unit mass
k	thermal conductivity, or core eigenvalue (multiplication factor)
l	unit cell conduction length
L	channel length
$\dot{m}$	mass flow rate
Nu	Nussult number
P	pressure
Pr	Prandtl number
q	heat flux
q'''_{gen}	volumetric energy generation rate
Q	heat transfer rate
R	universal gas constant
Re	Reynolds number
r_e	Reynolds number ratio, Re_P/Re_m

t	time
T	temperature
u	fluid velocity
V	volume
z	elevation

Sub-scripts and Super-scripts

(0)	iteration 0
(1)	iteration 1
(2)	iteration 2
ave	average
conv	convection
e	outlet
ent,hy	hydrodynamic entrance length
gen	generation
i	inlet, or mass centered fluid control volume number
j	momentum centered fluid control volume number
n	channel number
N	number of channels
s	surface index
tot	total

SUMMARY

A new transient thermal hydraulic method for simulating prismatic HTGRs during a loss-of-forced-circulation (LOFC) accident is presented. This expands upon the steady state thermal hydraulic methodology presented in the Author's MS Thesis. However, several key additions have been made. The largest is the addition of a transient analysis method that computes the fluid mass, velocity (momentum), and energy throughout a transient. This is achieved by using a well-documented, semi-implicit pressure-correction scheme. The fluid volumes are assumed to be 1-D to allow for the use of standard heat transfer and pressure drop correlations. Simple transient velocity and pressure boundary conditions are employed. Helium is assumed to be an ideal gas with constant specific heats, which allows for the use of simple thermodynamic relationships to close the fluid model. Models for reactor containment cooling (RCCS) heat transfer and decay heat generation have also been added.

Using the method developed here, both the pressurized (P-LOFC) and de-pressurized (D-LOFC) accident have been simulated. Results from these analyses confirm the HTGR's key safety advantage over all LWRs and most other advanced reactor designs, which is to have passive, indefinite cooling capability for the most limiting accident.

A RELAP model has also been developed and tested for the HTGR. This is done to highlight the limitations of existing methods for the simulation of the prismatic fuel and to emphasize the need and novelty of the method developed here. The newly developed method provides two significant advantages over available thermal hydraulic analysis techniques. The first is its ability to compute whole-core results and capture the important transient core-level phenomena such as bypass flow, and heat redistribution into the reflector assemblies after reactor SCRAM. The second is its ability to compute each fuel assembly in detail; computing the heat rates and temperature profiles for every fuel pin,

graphite, and coolant channel. These two factors combine to produce realistic, 3-D transient results for prismatic HTGRs during a LOFC.

1. INTRODUCTION

A new class of gas cooled reactors is being investigated for its many advantages over existing Generation II-III and Generation III+ (e.g., Westinghouse AP1000, G.E. ESBWR, Areva EPR) reactors. These high temperature gas cooled reactors (HTGRs) are being designed to have core outlet temperatures in excess of 850^{o}C. This is only now possible due to advancements in TRI-Isotropic (TRISO) coated fuels, which can sustain very high temperatures without cladding failure. Being able to produce a large, reliable, carbon emission free supply of high grade thermal energy opens new avenues for coupled process heat applications (e.g., hydrogen production).

In addition to the potential coupled process heat economic advantages, HTGRs also have substantial safety benefits over more traditional light water reactor and other advanced reactor designs. The passive safety features employed by HTGRs allow for indefinite heat removal for most accident scenarios including the type that crippled the Fukushima Daiichi plant in Japan.

The central component to the passive safety operation of HTGRs is the Reactor Containment Cooling System (RCCS). It is either an air-cooled or water-cooled system that operates without the use of pumps or electricity. Its purpose is to cool the containment walls, which in turn cool the reactor vessel wall through thermal radiation and conduction within the containment gas space. Cooling of the vessel wall subsequently cools the helium inside in the vessel. This action establishes a natural circulation loop from the core to the vessel wall.

The design and analysis of the RCCS has been well documented in recently published work, see Vaghetto and Hassan (2014). However, the core and vessel thermal hydraulics have not been analyzed in sufficient detail to certify the passive safety operation for the HTGR. The principal goal of this work is to develop a high fidelity method for HTGR core thermal hydraulics that would be more suitable for estimating the in-vessel

passive safety performance. The rest of this chapter is devoted to describing the geometry of the HTGR in more detail, as well as describing the accident scenarios of interest, and the scope of the current research. More information about the HTGR's historical background and the differences between specific HTGR designs can be found in Huning (2014).

1.1 High Temperature Gas Reactor (HTGR) Design Summary

HTGR development began in the mid-1960s with the operation of several prototype and commercial reactors in the US and UK. The developmental history of these early designs including the most recent commercial US HTGR, Fort St. Vrain Generating Station in Platteville, CO, can be found in a paper by August and Hunter (2008). Helium was selected as the coolant for its inert radioactive and chemical properties, and favorable high temperature thermal properties. Graphite was selected as the moderator due to its neutron moderating properties and resilience at high temperatures. Fuels were designed with both low enriched uranium and thorium options for breeding in advanced fuel cycles. Efficient usage and high burn rates of the fuel allows for less spent fuel or waste to be produced than in current reactors.

Current prismatic HTGR designs include the General Atomics GT-MHR, Areva ANTARES, and other conceptual designs by the US Department of Energy (DOE) and Korean Atomic Energy Research Institute (KAERI). The Modular High Temperature Gas Reactor (MHTGR-350), see Williams *et al.* (1989), proposed by the DOE, and designed with help from a number of different companies, including General Atomics, was selected as the reference design for the work presented here. The prismatic HTGR core layout is similar across all of the conceptual designs. A cross-sectional view of the MHTGR core is shown in Figure 1.1.

The MHTGR is smaller than designs being investigated today and is rated for 350 MWth. The active core consists of hexagonal graphite assemblies with holes for fuel

compacts and coolant channels of similar diameters at a ratio of two to one, respectively. The core is stacked 10 blocks high for a total height of eight meters. Coolant flows downward through the core. At initial fuel loading, control rods are axially withdrawn upward and power/temperature peaks in the lower half of the core.

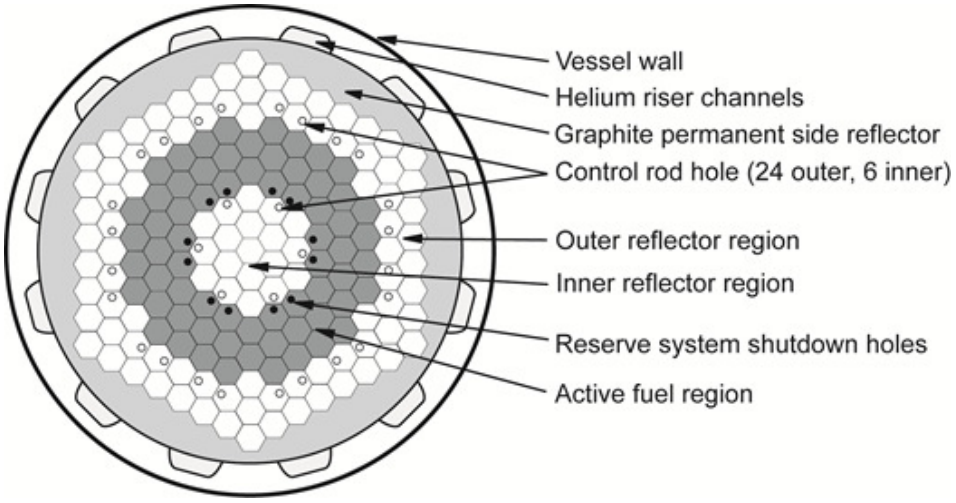

Figure 1.1 MHTGR Core Arrangement, Adapted from Williams *et al.* (1989)

While the core arrangement and thermal-fluid parameters may differ between specific HTGR designs, the assembly and fuel designs are similar. The inner and outer reflector block regions are solid graphite. The active fuel region consists of regular fuel and control rod fuel assemblies. The regular fuel assemblies contain 108 circular coolant channels, 210 cylindrical fuel pins containing TRISO particles imbedded in a graphite matrix, and locations for six burnable poison pins. Prismatic HTGR fuel and control rod assemblies are identical in geometry and dimensions across most designs (GT-MHR, Areva, MHTGR). The regular fuel and control rod fuel assembly geometries are shown in Figure 1.2, see Williams *et al.* (1989).

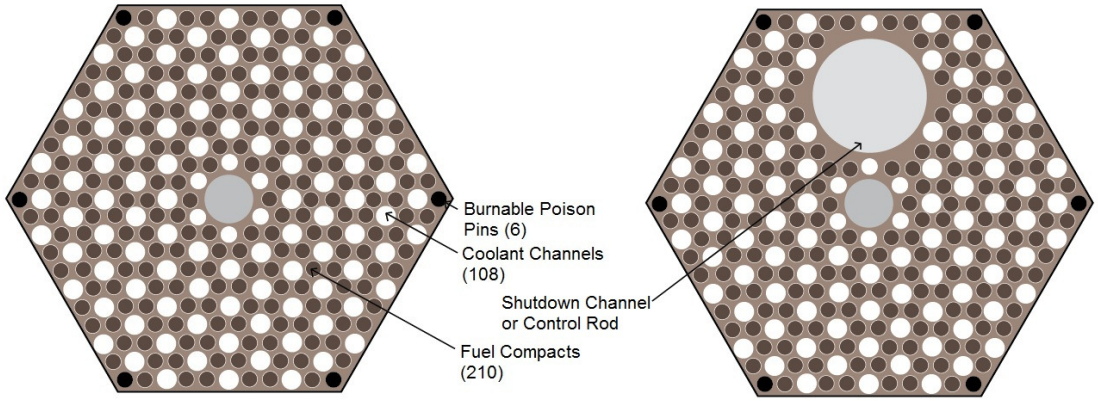

Figure 1.2 Regular Fuel (Left) and Control Fuel (Right) Assemblies, Adapted from Williams *et al.* (1989)

The MHTGR is rated at 350 MW_{th} while most other HTGR designs are rated between 500 MW_{th} and 600 MW_{th}. This is compensated for by having a smaller core, fewer assemblies, and a slightly lower power density. The remaining thermal-fluid design parameters are listed below in Table 1.1, see Williams *et al.* (1989).

Table 1.1 MHTGR Thermal Design Parameters, see Williams *et al.* (1989)

Parameter	MHTGR
Core Thermal Power	350 MW
Power Density	5.9 MW/m^3
Operating Pressure	6.4 MPa
Inlet Temperature	260 °C
Outlet Temperature	690 °C
Core Flow Rate	157.1 kg/s

HTGRs are expected to have several active normal operation and safety systems designed to shut down the reactor. During normal operation, control rods are inserted and hot helium gas is cooled by a connected intermediate heat exchanger such as a steam generator, as is the case for the AREVA HTGR design. If this is not available or not properly functioning, it is expected that there will be a low pressure water-cooled heat exchanger connected at the base of the vessel. For the MHTGR, this is called the Shutdown

Cooling System (SCS). If this does not operate, for example, if there is no electricity to drive the pumps for the water, then heat removal is expected to occur by the Reactor Containment Cooling System (RCCS). A diagram of a generalized HTGR reactor vessel is shown in Figure 1.3.

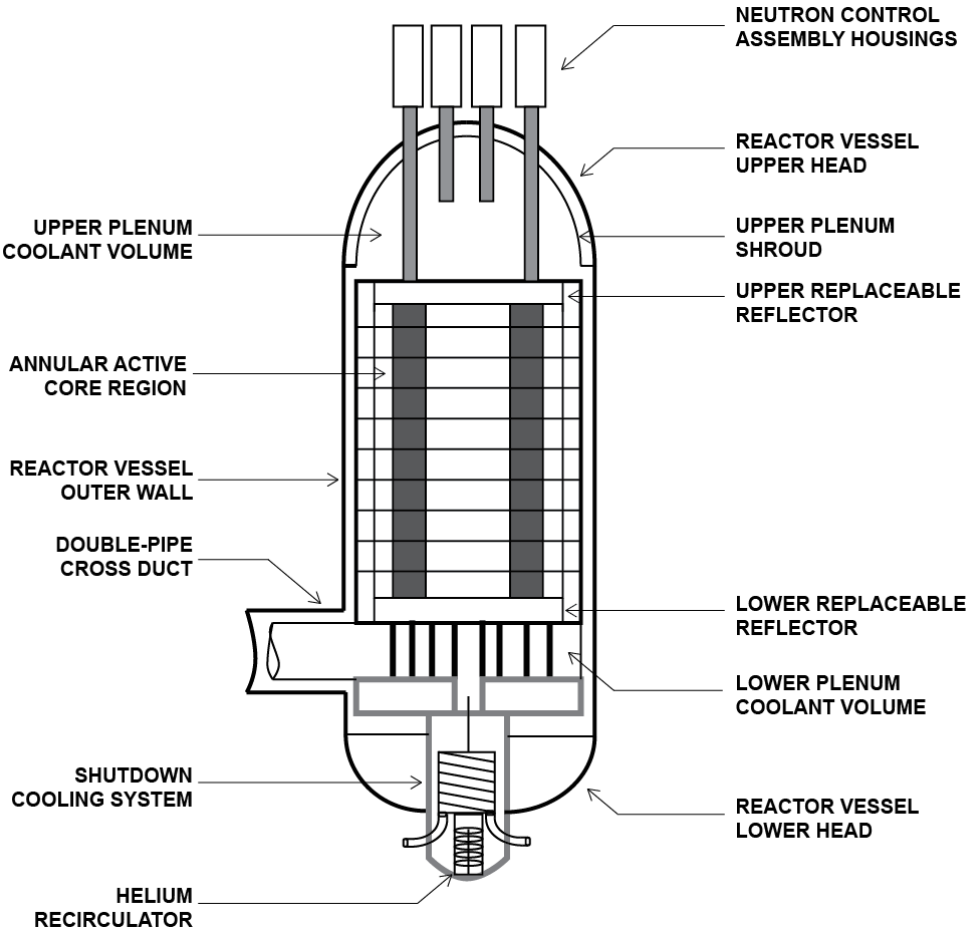

Figure 1.3 HTGR Vessel Elevation View

The RCCS can either be air- or water- cooled. For either case, no pumps or circulators are required. The system is highly reliable since there are no moving parts and it is always open to the environment. The RCCS operates by cooling the containment walls which cools the vessel by heat conduction and radiation. For the core to successfully cool down, helium natural circulation within the vessel must be established to convectively cool the graphite fuel blocks. Depending on the specific accident, this recirculation may or may

not occur, which could lead to fuel failure. The design safety basis case for HTGRs is the Loss-of-Forced-Circulation (LOFC) accident.

1.2 Loss-of-Forced-Circulation (LOFC) Accidents

Early safety evaluation documents by Williams *et al.* (1989) and General Atomics (1996) set the foundation for prismatic HTGR safety analysis. In these reports, a set of bounding design basis events (DBEs) evaluated the use of low order plant dynamics models. For example, the fluid transport models typically ignore fluid inertia and unique core flow paths such as bypass channels.

In the case of the MHTGR, DBEs include loss of heat transport and shutdown cooling systems (DBE-1), moisture ingress (DBE-6), primary coolant leak (DBE-10), primary coolant leak without heat transport and shutdown cooling systems (DBE-11), and others. DBE-1 is particularly important today because this reflects an extended station blackout (SBO) scenario in which no electrical power is available. DBE-1 is commonly known today as a pressurized loss-of-forced-convection (P-LOFC) scenario. DBE-11 is commonly known today as a depressurized loss-of-forced-convection (D-LOFC) scenario. For both cases, a reactor trip is assumed to occur at the start of the accident and thus core power decreases according to the decay heat curve. For all cases, the reactor cavity cooling system (RCCS) is assumed to operate. Figure 1.4 shows the helium flow path within the vessel for each LOFC case.

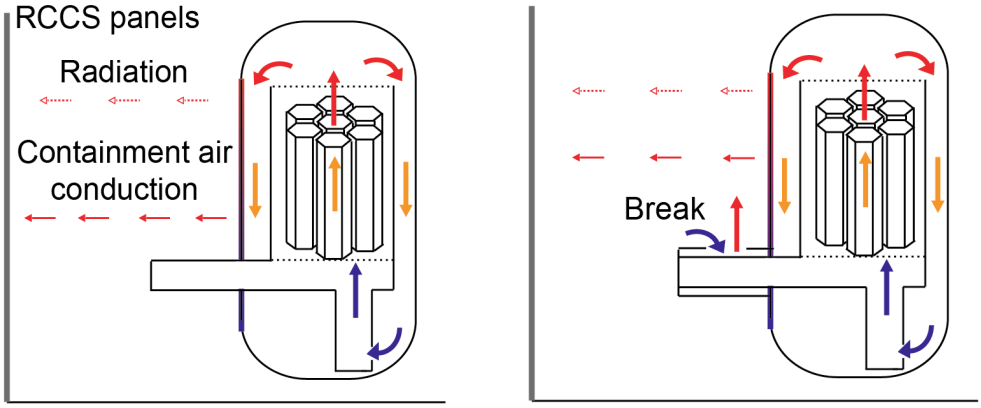

Figure 1.4 P-LOFC (Left) and D-LOFC (right) Vessel Flow Paths

The accident progression for these accidents is typically as follows:

- Loss of all onsite and offsite electrical power (Station Blackout)
- Control rods insert due to power failure
- Helium circulators stop and flow ceases
- Fuel temperatures initially decreases as core power rapidly decreases
- Graphite and fuel temperatures slowly increase over time as helium flow is reduced
- As core helium temperature begins to increase:
  - Helium natural circulation flow increases
  - Vessel wall temperature begins to rise
  - RCCS heat removal to the environment increases
- After some time (around 24-48 hours, also referred to as, t_{eq}), RCCS heat removal rate outstrips the core heat generation rate
- Core temperatures begins to decrease to a stable condition

The key question for these accidents is, "Does the peak fuel temperature over the length of accident exceed the fuel failure temperature?" For the D-LOFC accident, the pressure is reduced to approximately 1 MPa, compared to the P-LOFC case that remains

near the nominal 6.4 MPa. This leads to a reduction in helium density for the D-LOFC case. Therefore, a larger temperature difference between the core and the vessel wall is needed to drive natural circulation at an adequate mass flow rate for the D-LOFC case. In the MHTGR safety evaluation document by Williams *et al.* (1989), the PANTHER code was used to simulate the D-LOFC accident. Figure 1.5 contains a plot of the heat generation, RCCS heat removal, and vessel temperature over the D-LOFC accident.

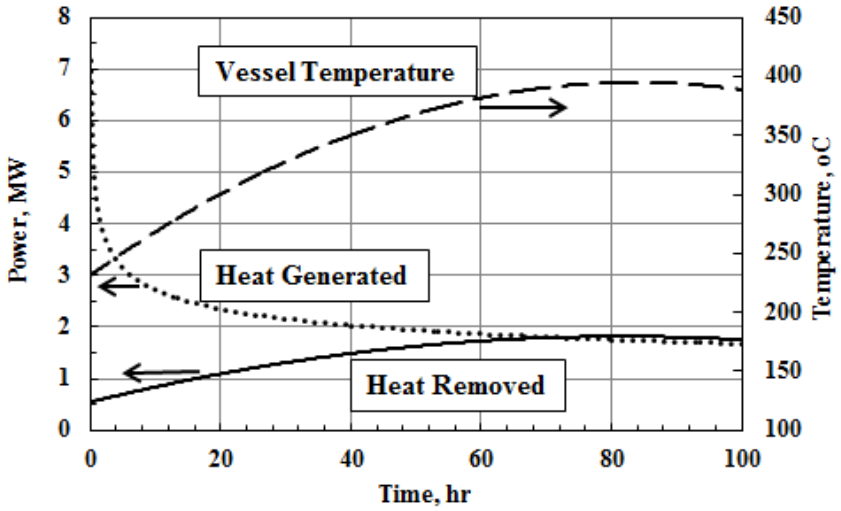

Figure 1.5 D-LOFC Energy Balance from Williams *et al.* (1989)

For TRI-ISOtropic (TRISO-coated) fuels, the expected fuel failure temperature is 1600ºC based on early TRISO fuel safety and performance data, Williams *et al.* (1989). In Figure 5, at approximately 70 hours from the initiation of the accident sequence, the heat generation matches the heat removed by the RCCS. At this time, the peak fuel temperature is just below 1600ºC. However, many assumptions and approximations are made in the simulation with the PANTHER code, which may lead to higher predicted fuel temperatures. Since there is very little predicted safety margin for the D-LOFC accident with low-order calculations, higher fidelity calculations are needed to ensure that safety margins are still met. Some of the most critical assumptions associated with coarse or low-order thermal hydraulic tools include:

- Single (sub-channel) approach
- Graphite/fuel/helium homogenized thermal unit cells
- Bypass flow neglected

The difficulty in using available transient simulation tools is that the HTGR assembly geometry is not well modeled. This leads to incorrect estimates for heat conduction within the graphite and ultimately incorrect peak fuel temperature estimations. More detailed core modeling and LOFC analyses are needed to help certify the HTGR's passive safety features for the design safety basis cases.

1.3 Scope of Present Research

In the present investigation, a transient-fluid thermal hydraulic method capable of predicting the whole-core, 3-D, temperature, pressure and mass flow distribution is developed. This investigation primarily focuses on the active core region, but also includes simple models for the other vessel volumes. RCCS heat removal is approximated as a simple linear function versus vessel wall temperature. Although radiation heat transfer from a grey or black body is a fourth-order function of temperature, as the vessel wall temperature increases, the RCCS or containment wall temperature also increases, leading to a nearly linear increase in total heat removal as vessel wall temperature increases. Additionally, there are conduction and convective heat transfer effects within containment. Because of the modeling complexities associated with RCCS heat removal and containment geometry uncertainty, a simple model for heat removal vs. vessel wall temperature based on predetermined RCCS performance is used. The predetermined RCCS performance is based on the MHTGR air-cooled RCCS design as described in Williams *et al.* (1989).

Decay heat generation is approximated using standard ANSI decay heat curves for UO_2 fuel in a thermal spectrum reactor. The TRISO fuel used in HTGR is expected to be

low-enriched UO_2. The neutron energy spectrum is also expected to be thermal thus this assumption is deemed valid.

The initial temperature and power profile is supplied by a steady sate coupled calculation documented in Connolly *et al.* (2016). The method is then applied to the MHTGR and both Pressurized and Depressurized LOFC accidents are investigated. The results from these simulations are then compared with the predictions of a RELAP5-3D model of the MHTGR as well as with results published in the literature.

The method presented here expands on the steady state method described in detail in Huning et al. (2016), which has been successfully used for a number of different HTGR designs and cases. The MHTGR geometry, LOFC boundary and initial conditions used for the present work are taken from the MHTGR safety evaluation report by Williams *et al.* (1989).

The method presented here will be able to predict whole-core temperature profiles that capture the temperature gradients within each assembly block and fuel compact. The coupled semi-implicit fluid solver is able to predict the helium density, mass flow rate, and heat removal from each individual coolant channel. The thermal hydraulic models offer unique advantages over other available tools. It is currently not feasible to perform whole-core CFD analyses for the LOFC accidents. In contrast, the method developed here can perform whole-core transient calculations with much greater detail than systems level codes such as RELAP. This is demonstrated in a subsequent chapter in the dissertation when the LOFC results are compared against a RELAP5 model of the MHTGR and the prismatic fuel.

1.4 Organization of Dissertation

The remainder of this dissertation is organized as follows:

- Chapter 2 presents an overview of the available literature on HTGR safety and transient modeling methods.

- Chapter 3 presents the physical modeling aspects of the method, such as the core thermal unit cells and transient fluid procedure.
- Chapter 4 describes the numerical scheme, implementation, and use of auxiliary calculations to obtain the needed boundary and initial conditions
- Chapter 5 presents a summary of the P-LOFC and D-LOFC results using the developed method.
- Chapter 6 describes the development of the RELAP model of the HTGR and comparisons with the predictions of the method developed here.
- Chapter 7 presents conclusions based on the transient results and suggests areas of future research.

2. LITERATURE REVIEW

Over the years, research on HTGR thermal hydraulics has been conducted by many different domestic and international organizations. Today, HTGRs have received renewed interest due to their ability to provide a clean source of high temperature heat for industrial process applications, in addition to electrical power generation. The need for high efficiency process heat inspired the selection of AVERA's prismatic HTGR design to be the ideal candidate for the Next Generation Nuclear Plant (NGNP) by the NGNP Industry Alliance in 2012. Since then, companies such as AREVA, General Atomics, and others have been exploring potential licensing paths for the HTGR. One major step for licensing is the demonstration of successful passive safety operation of HTGRs for the design safety basis cases. For HTGRs, these are the P-LOFC and D-LOFC cases.

Other accident scenarios important to the safety and licensing of the HTGR include air and water/moisture ingress. While peak fuel temperature is still a major concern, material and structural issues involving graphite oxidation are equally as important for these scenarios. However, most analyses show that even for extreme cases, absent of core structural concerns, peak fuel temperature is no worse than for the LOFC accidents.

Several different thermal hydraulic analysis tools exist to compute the core transient information to demonstrate LOFC safety margin. These principally fall into three different categories: (a) CFD, (b) system level, and (c) unit cell or intermediate level. CFD techniques are well equipped to compute the detailed assembly temperature profiles but are unable to perform whole-core calculations due to computational costs. System-level codes such as RELAP are well equipped to compute core-level temperature profiles but are usually restricted to just a few fuel pins or assemblies. It is also difficult to approximate the assembly geometry correctly using simple equivalent cylinder or slab models. Unit cell and intermediate level techniques, such as the one presented in the following chapters, have

the highest potential since whole-core calculations are possible with computed pin or near-pin-level temperature gradients for the hexagonal fuel assembly geometry.

The lower and upper plenum volumes within the vessel are also important for both steady state and transient safety. Analyzing coolant flow entry and mixing into the lower plenum is important for identifying hot spots and investigating any material or mechanical concerns due to excessive heating. The upper plenum is primarily important for accident situations without forced circulation. Mixing and formation of turbulent eddies act to inhibit natural circulation through the vessel.

This chapter discusses in detail the current research on RCCS performance as well as for LOFC accidents, upper and lower plenum phenomena, and the available core thermal hydraulic tools to estimate LOFC transient behavior.

2.1 HTGR Thermal Hydraulic Analysis Codes

For Light Water Reactors (LWRs), the U.S. Nuclear Regulatory Commission (NRC) does not mandate a specific thermal hydraulic safety analysis code or package of codes but instead offers regulatory guidance on standard expectations of analysis tools. Popular thermal hydraulic and severe accident codes for LWRs in the nuclear industry include:

- RELAP5/SCDAP, Idaho National Laboratory (2005),
- MAAP, Electric Power Research Institute (2010),
- MELCOR, Gauntt *et al.* (2000), and
- TRACE, U.S. Nuclear Regulatory Commission (2001).

Due to the significantly different flow and core geometry for gas reactors, these LWR codes may not be suitable for the analysis of HTGRs. One option could be to couple CFD core heat transfer calculations to systems level calculations by RELAP. Another option for modeling secondary side transient analysis is to use MELCOR-H2, which is extends MELCOR's standard primary side and containment severe accident capabilities.

In addition to these options, the GAMMA+ code, Kim *et al.* (2010), is a new code developed specifically to analyze air ingress events and hydrogen plant transients. The GAMMA+ code solves the conservation equations for a mixture of many gas species and solid nodes. It also contains a turbomachinery model for integrated plant response.

The methodology for calculating core temperatures during transients is significantly different than for calculating steady state temperatures. The main difference between modeling the two operating modes is spatial resolution. Larger, more encapsulating, computational unit-cells must be used to increase the speed of the transient calculations since VHTR transients can typically progress for hundreds or thousands of hours. Transient modeling also typically requires thermal hydraulic feedback or inputs from various other models such as neutronics or structural calculations.

2.1.1 CFD Analyses

CFD codes such as:

- Trio_U, Bieder and Graffard (2008),
- FLUENT, FLUENT (2005),
- Fuego, Sandia National Laboratories (2008),
- CFX 11, ANSYS Inc. (2006), and
- STAR-CCM+, CD-adapco (2008),

have been used to determine steady state temperature profiles for a number of HTGR cases. A brief list of some of these studies can be found in Table 2.1.

Table 2.1 Steady State CFD Analyses

Study	Code	Note
Anderson *et al.* (2008)	STAR-CCM+, CD-adapco (2008)	Coupled RELAP core model, CFD lower plenum flow
Cioni *et al.* (2006)	Trio_U, Bieder and Graffard (2008)	Partial coolant channel blocking
Johnson (2008)	FLUENT, FLUENT (2005)	RANS vs URANS comparison for CFD HTGR experimental validation
Karaismail and Celik (2010)	FLUENT	Lower plenum flow for a simplified experimental model
Rodriguez and El-Genk (2010)	FUEGO, Sandia National Laboratories (2008)	Analysis of lower plenum helical coil inserts
Sato *et al.* (2010)	FLUENT	0, 3, and 5 mm bypass gap width
Tak *et al.* (2008)	CFX 11, ANSYS Inc. (2006)	1 and 5 mm bypass gap width
Wang *et al.* (2014)	STAR-CCM+	Bypass and cross-flow estimation

A few consistent conclusions can be drawn from the various CFD studies of the core and lower plenum flows. The first is that boundary conditions and core power profiles are important. In a study by Anderson *et al.* (2008), coupling to RELAP5 proved important for matching boundary conditions in the lower plenum. Without whole-core modeling, computed individual mass flow distributions for partial assembly cases were based on average core assembly flow rates instead of their exact values. This leads to under predicted fuel temperatures for the particular assemblies that had lower flow rates than the average. Power profiles for all core assembly and bypass cases were assumed to be uniform or flat axially. This also leads to lower computed assembly temperatures.

The second conclusion is that there is still disagreement on which turbulence models and CFD methods are more suitable for HTGRs. Most studies, like Sato *et al.* (2010) or Tak *et al.* (2008), used the realizable k-ε model. However, this was estimated by Johnson (2008) to not predict unsteady vortex shedding correctly and he recommended that

the Reynolds stress model (RSM) should be used for HTGR assembly problems. CFD modeling differences, as described in Johnson (2008), have been found to yield differences in peak fuel temperature by as much as 100°C.

Finally, for all lower plenum and core cases, the minimum number of computational cells for a single assembly was found to be between 500,000 for a 2-D calculation and 2 million cells for a 3-D calculation. Most of the reported calculation times for the CFD cases listed in Table 2.1 were between 50 hours to a week. Extrapolating to a whole-core calculation (e.g., the MHTGR), the mesh would need at least 85 million cells (169 × 500,000) not including cells for the connected vessel volumes such as the plenums and riser channels. This computational analysis method is not practical for commercial reactor safety analysis.

2.1.2 Unit Cell and Non-CFD Core Thermal Hydraulic Analyses

Unit-cell methods typically include 2D or 3D core heat transfer geometry models and simplified iterative thermal hydraulic schemes. This method allows for larger fractions of the core to be modeled with less computational effort than similar CFD models. Because of the added fuel assembly complexity, new methods beyond standard LWR sub-channel approaches (e.g., COBRA-TF, Salko and Avramova (2015)) are needed for prismatic gas cooled reactor design and analysis.

Since the initial introduction of the HTGR and VHTR designs based on the MHTGR and GT-MHR cores respectively, a thermal hydraulic and neutronic analysis study was performed by MacDonald (2003) at INL and General Atomics. The NGNP point design considers both the pebble bed and prismatic type VHTR designs. The goal of the analysis was to perform parametric sensitivity studies to establish an analytical starting point for future evaluations by quantifying the impact of variations to key design parameters such as core power, power density, assembly geometry, fuel configuration and others. The parametric studies investigated the impact of bypass flow, flow distribution, and total reactor power. RELAP5-3D/ATHENA calculations were performed for P-LOFC

and D-LOFC accidents. The results of the simulated LOFC accidents are discussed in the next section.

The core heat transfer methodology of the point design study involves using a number of triangular unit-cells to approximate one third of the core. Each unit-cell contains graphite, one sixth of a coolant channel, and one third of a fuel pin. Core power density is determined using Monte Carlo (MCNP) reactor physics calculations from the initial neutronics point design studies as part of the NGNP report. The power profile used for the thermal hydraulic calculations resembles a chopped cosine that is peaked in the lower half of the core. This shape is due to the insertion of control rods from the top to the critical mid plane of the core. Values for total coolant flow, inlet pressure and temperature are assumed. The fraction of flow that bypasses the coolant channels and the fraction of heat removed by the bypass flow are also assumed. One important assumption was neglecting cross flow between coolant channels. Cross flow could occur do to small cracks within the graphite assembly and the pressure difference between channels at given axial locations. Once the problem was bounded, calculations were performed to estimate the impact of critical parameters. The main recommendations of the thermal hydraulic point design studies were:

- Continue to perform nuclear design and core configuration studies such that power peaking could be reduced.
- Use a finer resolution and local power densities for the thermal hydraulic calculations to capture 3D effects.
- Develop a more detailed flow network that explicitly determines bypass and cross flow. Using the detailed model, determine core locations for fixed orifices that minimize transverse pressure gradients. Also use the detailed model to analyze mechanical solutions that minimize total bypass flow and correspondingly, maximum fuel temperatures.
- Additional recommendations, but not investigated in the parametric studies include, possibly switching to annular fuel compacts to reduce the compact

thermal resistance, reducing the gap space between the compact and graphite block, and reducing the diameter of the compacts while increasing the number of compacts per assembly. Another recommendation not investigated would be to possibly increase the surface roughness of the coolant channels by balancing the additional heat transfer benefit against the allowable pressure drop.

Since the NGNP point design, there have been some neutronic and thermal hydraulic studies that are more detailed and offer as many design insights as the initial point design report. One such similar design study was performed by F. Damian (2008) in support of the European Union RAPHAEL project. The VHTR core characteristics presented are most similar to the GT-MHR with inlet and outlet temperatures of 490 and 850°C, respectively. Thermal hydraulic and neutronic trade-off studies were performed using the 3-D thermal hydraulic code CAST3M, Studer *et al.* (2003), and neutronics calculation scheme NEPHTIS, Cavalier *et al.* (2006). The thermal calculations were performed in detail for a "hot spot" assembly. Several fuel and assembly geometry configuration changes were tested in an attempt to reduce maximum fuel temperature. The results indicate that minor improvements are possible but the results would not likely warrant the modifications. Reducing the radial peaking factor was the most successful method to reduce the maximum fuel temperature. To reduce radial peaking, several fuel burn-up, fuel loading, and enrichment options were analyzed. The fuel element management scheme using fresh fuel in the middle active core ring, second cycle fuel in the outer ring, and third cycle fuel in the inner ring provided the largest reasonable reduction in peaking factor.

2.2 LOFC Analyses

Conduction cool-down or LOFC cases were among the first scenarios analyzed for early HTGR designs. During a P-LOFC scenario, a reactor trip is assumed to occur at the start of the accident. For the D-LOFC scenario, a primary system break is assumed to occur

followed immediately by a reactor trip at the start of the accident. However, this does not necessarily have to occur as the core will begin shutting down upon fuel heat-up. In that case, recriticality would be a concern but not until core temperatures fall back below their initial values. This could be hundreds of hours after the accident initiation, at which point operators could use standard reactivity control mechanisms.

Under normal circumstances (*i.e.*, electrical systems operational and no station black-out), the power conversion system (PCS) will continue to operate and remove decay heat with the shutdown cooling system (SCS) in standby. For the direct Brayton cycle, the PCU/PCS consists of a turbine/compressor/generator unit, recuperator, precooler, and an intercooler. Heat is rejected through the water cooled precooler and intercooler. For an indirect Rankine cycle, the power conversion unit consists of a steam generator and associated feedwater components. In some designs, the power conversion unit contains a helium cooled intermediate heat exchanger for an additional protective loop separate from the reactor. If the PCS is not available, then the SCS will cause closure of the main loop shutoff valve. The SCS consists of a circulator, heat exchanger, and shutdown loop shutoff valve. The SCS heat exchanger is water cooled by a single loop that serves all plant modules requiring cooling. The peak cooling capacity of the SCS is typically 10 times that of long term decay heat levels of only a few MW. When the power conversion and shutdown cooling systems fail to remove decay heat from the coolant, the reactor cavity cooling system (RCCS) will passively remove heat from the vessel by thermal radiation and natural convection as temperatures rise. The RCCS, first implemented by the MHTGR, is designed to prevent core damage for both the P-LOFC and D-LOFC cases.

The NGNP point design analysis, see MacDonald (2003), indicates that maximum fuel and vessel temperatures for both pressurized and depressurized cases are sensitive to the decay heat rate, effective graphite conductivity, vessel emissivity, and insulation value for the upper plenum among the other normal reactor design values. Several studies have been performed to investigate the peak fuel and vessel temperature over both the P- and D-

LOFC accident scenarios. The P-LOFC is less challenging than the D-LOFC case due to the coolant remaining at high pressure. The higher pressure is beneficial for core heat transfer and natural circulation. Therefore, it is more important from a safety perspective to investigate core and vessel integrity over the life of a D-LOFC accident. Williams et al. (1989) suggests that P-LOFC accidents should be considered simply as a single variation of the D-LOFC. While the studies vary in the choice of reactor design, power level, core dimensions, and choice of analysis tool, some similar trends are observed and are discussed here. Three different D-LOFC studies are reviewed here.

The first is the study of MTHGR cases presented in Williams *et al.* (1989), which uses an ORNL code called "MORECA", Ball (1991), as the LOFC analysis tool. The MHTGR as presented in the Safety Evaluation document has a core thermal power of 350 MW and initially has an average fuel temperature 690^{o}C. The accident is initiated with a hot-duct pipe break into containment followed by insertion of control rods. The second case is the Japanese conceptual GTHTR-300 presented in Sato *et al.* (2013). This reactor design has a core thermal power of 600 MW and the fuel is initially 850^{o}C. This D-LOFC analysis was performed using the RELAP5-3D code with the enabled Point-Reactor-Kinetics (PRK) model. The accident is similarly initiated with a primary depressurization near the hot duct but without control rod insertion. The reactor core quickly reduces in power to decay power levels for a major part of the scenario. The enabled PRK model allows for the calculation of when recriticality occurs. This is estimated to occur well beyond 300 hours into the accident. The third D-LOFC study, by Lommers *et al.* (2014), investigates the AREVA SC-HTGR. It has a core thermal power of 625 MW and an initial fuel temperature near 625^{o}C. The porous-media based thermal hydraulic solver Star-CD version 4.14, CD-adapco (2014), was used in this analysis. Nominal decay heating was assumed (*i.e.*, control rods inserted or fuel temperature reactivity feedback/shutdown).

For the nominal core configuration and operating conditions typical of each reactor design [MHTGR, Williams *et al.* (1989), SC-HTGR, Lommers *et al.* (2012), and

GTHTR300, General Atomics (1996)], the average and maximum fuel temperatures over the D-LOFC accident are plotted in Figure. 2.1.

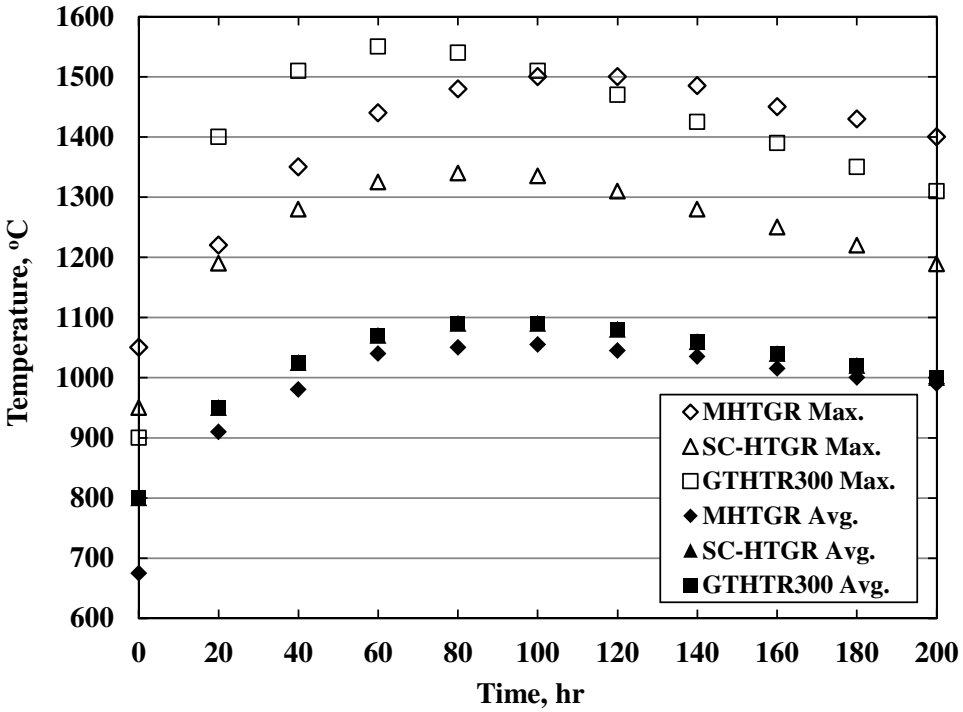

Figure 2.1 D-LOFC Fuel Temperature Comparison

The Japanese GTHTR-300 has the highest fuel temperature. However, it is still below the expected fuel failure condition of 1600°C. The fuel assembly configuration of the GTHTR-300 is substantially different than either the AVERA SC-HTGR or MHTGR, which could account for the difference. For all cases, the temperatures reach a peak between 60-120 hours. This is due to the lag between the vessel heat removal and decay heat generation. As the vessel heats up, more heat is removed from the vessel to auxiliary cooling systems such as the RCCS. As time passes, heat generation decreases until it matches vessel heat removal.

D-LOFC cases have the potential to challenge internal structures such as the core barrel and reduce the structural integrity of graphite support structures by oxidation. Sensitivity studies by Kim *et al.* (2010) underscore the potential weakness of the VHTR

for D-LOFC cases when the RCCS fails to operate. The highly reliable system could fail by introducing an air-flow blockage in the intake, exhaust, or cooling panel structures as could be the case during a large pipe break. Transient analysis was performed with the GAMMA+ code. Cases with reactor cavity insulation, without insulation, and with large thermal conductivities for soil and concrete were analyzed for the D-LOFC with no RCCS available. Some transient cases were simulated for 2500 hours or more. A key finding in the analysis is that the reactor cavity insulation serves as a dominant obstacle against heat transfer where heat is transferred primarily by conduction from the fuel to the soil surrounding containment. The limiting maximum temperatures may not occur in the fuel but in the vessel material. In just a few hours, the vessel temperature exceeds the recommended limit of 560°C for reactor vessel steel (9Cr1Mo). Fuel temperatures exceed 1600°C around 50 hours when reactor vessel temperatures are near 800°C. Opportunity exists to turn around core and RPV temperatures at 100 hours if the soil and concrete have thermal conductivity values 10 times the standard values. Based on these findings, there is a need for an alternate reactor cavity heat removal mechanism for the VHTR for a D-LOFC case with no RCCS availability. It should be noted that the AREVA SC-HTGR design utilizes a water cooled RCCS. However, it is just as prone to blockage or worse leakage as the air-cooled system. For instances with the failure of either RCCS system, alternate cooling mechanisms will be required.

Instead of cooling the reactor cavity, it may be possible to directly cool the reactor vessel through a variety of methods. Options include: external cooling by an active fan system placed beneath the vessel, an internal vessel cooling system by segregating the primary coolant helium from vessel cooling helium, and placing an additional insulation layer between the core and vessel wall. Of the three options, Kim *et al*. (2008) found that the insulation layer was the most viable and offered the greatest reduction of RPV temperatures. Possible insulation options include Microtherm or Superwool 607 materials between 0.5 and 5 mm thick placed just inside the core barrel or just inside the vessel wall.

The penalty of adding an insulation material layer is seen in the associated increase in fuel temperatures. There is a tradeoff between decreasing vessel temperatures and increasing fuel temperatures. As mentioned earlier, some increase in fuel temperatures could be acceptable as vessel temperatures generally exceed their respective limits before the fuel does.

In summary, P-LOFC and D-LOFC scenarios when the RCCS operates normally are not expected to raise fuel temperatures beyond their limits. If the RCCS does not operate or only partially operates, then vessel temperatures could quickly exceed their limit suggesting that a backup or alternate method for reactor cavity cooling should be investigated. Vessel cooling options such as adding an insulation layer could mitigate the need for an alternate reactor cavity cooling system. Although P-LOFC scenarios are not as challenging from a fuel perspective as the D-LOFC cases, one remaining issue could be that upper head and vessel temperatures increase beyond their acceptable limit. Therefore, it is still necessary to simulate this event. Additional insulation could be placed in these regions to reduce the inner wall temperatures. In that case, the RCCS, either water or air-cooled, should be sized accordingly.

2.3 Upper Plenum LOFC Implications

To establish whether natural circulation will be present in the HTGR during a loss-of-forced-convection accident, the flow in both the core and upper plenum must be experimentally verified. Buoyancy forces result in hot gases flowing upward through the core and into the upper plenum above the core. Flow in the core coolant channels is important since it establishes the inlet velocity and temperature condition into the upper plenum. Once in the upper plenum, the amount of mixing, and the specific flow patterns that develop will determine the heat transfer to the vessel upper head and into the riser channels along the vessel wall. Finally, heat transfer away from the vessel wall is critical for energy balance and for the core to maintain a safe and stable temperature distribution.

Experimental facilities for testing vessel and plenum flows have been constructed at Oregon State University and at Idaho National Laboratory, Johnson and ASME (2009). These test facilities have been designed to measure flows similar to those expected in HTGRs at shutdown with and without forced circulation. Natural circulation is particularly important to measure since it is critical in transferring heat away from the core to the vessel wall, where it can then be removed by the RCCS. To properly scale these facilities so that similar flow behavior can be observed, fluid Richardson and Reynolds numbers for the experiment must match the HTGR high temperature helium conditions. In most cases, low temperature water is chosen to be the experimental working fluid since the fluid properties of both fluids are similar enough that both the Richardson and Reynolds numbers can be matched (*i.e.*, $\mathrm{Ri}_m = \mathrm{Ri}_p$ and $\mathrm{Re}_m = \mathrm{Re}_p$) with similar characteristic diameters (D_H). A schematic of the PIV upper plenum flow experiment at INL is shown in Figure 2.2.

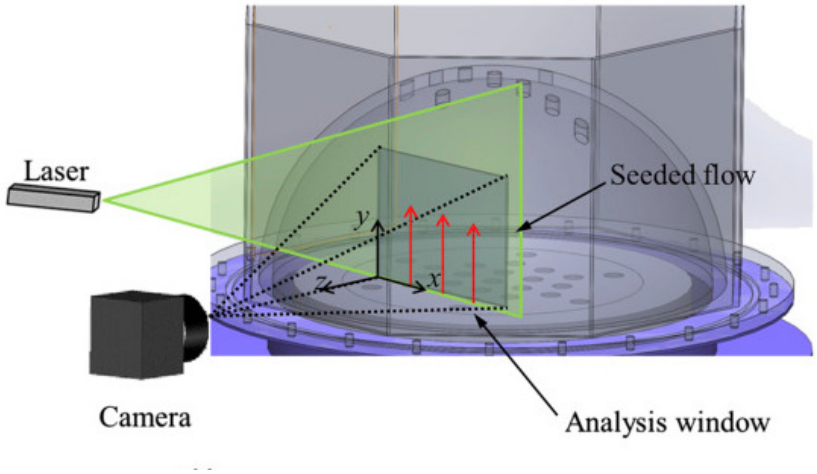

Figure 2.2 INL Upper Plenum PIV Experimental Schematic Reproduced from McVay *et al.* (2015)

Using the channel diameter as the characteristic dimension and the channel temperature rise, corresponding HTGR helium temperatures can be computed using the flow and temperature results from McVay *et al.* (2015). Complete matching of the

Richardson and/or Reynolds numbers may not be possible for all locations within vessel. In particular, when the channel dimensions and temperatures are used to match Richardson numbers, expected helium channel Reynolds only numbers differ by a factor of 0.4 to 1.0. Assuming that the Richardson number is the more relevant parameter to match between the experiment and the HTGR, for some particular Reynolds numbers, the corresponding HTGR helium temperatures are plotted in Figure 2.3.

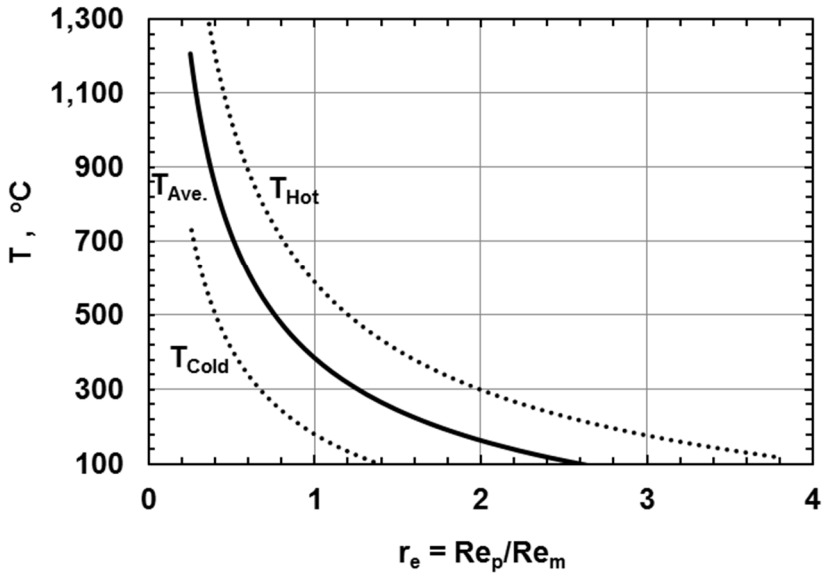

Figure 2.3 Helium Coolant Channel Temperatures as a Function of Reynolds Number Ratio for the Experiment in McVay *et al.* (2015)

From Figure 2.3, for realistic core helium temperatures, the Reynolds number ratio should be between 0.4 and 1.0. This corresponds to channel average temperatures between 390 and 820ºC. Outside this range, peak (hot) helium temperatures greater 1,300ºC could challenge internal vessel structures and cold temperatures below 120ºC would require inner vessel wall temperatures well below expected values during RCCS operation.

For the same working fluid, very few adjustments could be made to the experiment to better match helium conditions in the coolant channels during a LOFC accident. Under natural circulation, mass flow cannot be altered without changing channel power or fluid

properties. Similar to mass flow, temperature rise also cannot be easily modified without changing power. Considering channel power is strictly chosen to reflect certain decay power conditions, it should not be modified unless a different accident time-frame is selected. Water properties are predominantly affected by the average temperature and not pressure. Thus, increasing or decreasing system pressure will not likely alter the fluid property values in the Richardson and Reynolds numbers. Finally, it is possible that other fluids could have more favorable properties and be a better substitute, but then PIV may or may not be possible. Consequently, only the water average temperature and channel diameter can be reasonably adjusted.

If the channel diameter is increased, (e.g., $D_{H,m} = 0.03\ m$), then the applicable helium Reynolds numbers are reduced to 0.45 – 0.6 that of water. Decreasing channel diameter (e.g., $D_{H,m} = 0.012\ m$) has the opposite effect of expanding possible helium Reynolds numbers to 0.3 – 1.3. Minor experimental channel diameter changes lead to either Reynolds number ratios too small or the range being too broad. Thus, current experimental channel diameters are best suited to model helium conditions using water.

Matching Richardson numbers in upper and lower plenums is more of an approximation than for the channels due to mixing and complex flow behavior. The difficulty arises in defining a suitable characteristic length or hydraulic diameter ($D_H = 4 \cdot A_F / P_W$), as well as the temperature difference that is represented. In an INL report by McCreery and Condie (2006), it has been suggested that the distance and outlet temperature between channels be used for both the upper and lower plenums. Unlike the case of the core coolant channels, a range of possible upper plenum average temperatures is possible for a single specified Reynolds number ratio. Based on the same upper plenum experiment, and assuming the model temperature difference is 0.5°C, which was the thermocouple uncertainty since each channel was mentioned to have around the same

outlet temperature, the prototype (HTGR) outlet temperature difference between channels is plotted in Figure 2.4.

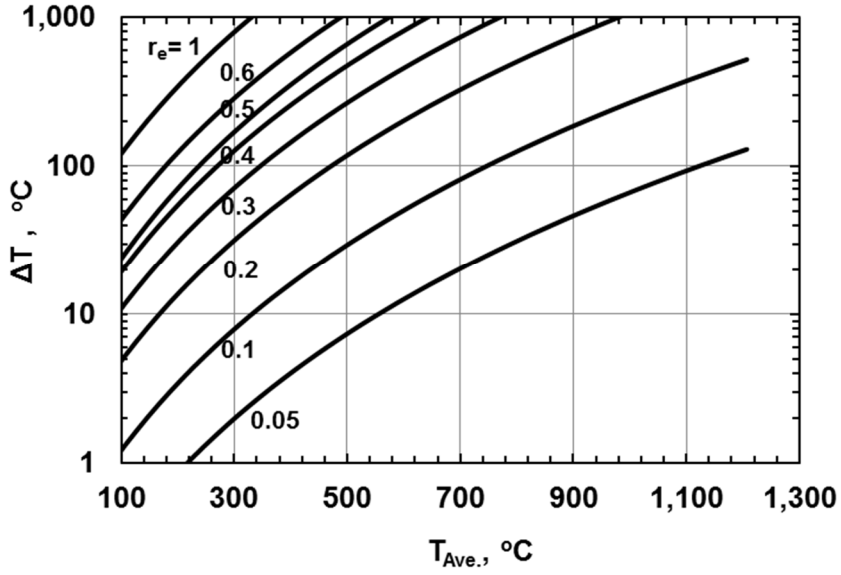

Figure 2.4 Upper Plenum, Helium Temperature Difference between Channels

One constraint on the upper plenum is the temperature of the coolant entering the upper plenum. From Figure 2.3 it is observed that the hot temperature could vary between 600 and 1,300ºC. This forces the upper plenum Reynolds number ratio to a maximum of 0.15 to 0.2. This is a slight underestimation since the average temperature is expected to be slightly below the hot temperature due to heat loss. If the water temperature difference is smaller, at 0.1ºC, the curves in Figure 2.4 shift down and the maximum upper plenum Reynolds number ratio is closer to 0.5 to 0.6. For Reynolds number ratios closer to unity, the estimated temperature difference between channels is larger than what is reasonably expected for the HTGR.

For either the channel or plenum case, with matching Richardson numbers and channel powers, the observed water flow patterns best resemble helium flows with Reynolds numbers that are a factor of 2 to 8 smaller in the upper plenum and only 1 to 2

smaller in the channels. The expected helium velocity is nearly constant for any of the cases in Figure 2.3 or Figure 2.4. If the distorted helium Reynolds numbers do not significantly impede helium flow, from Figure 2.3, anticipated helium core temperature rise is between 400 – 700ºC. For stable core temperatures, this core temperature rise must be offset by the temperature drop along the vessel wall and upper plenum due to operation of the Reactor Cavity Cooling System (RCCS). Therefore, in addition to verifying vessel flow and corresponding core temperature rise, temperature drop along the vessel and RCCS performance must be verified to ensure LOFC and transient safety.

2.4 RCCS Performance Studies

For the VHTR, there are two RCCS designs currently under discussion. The first is an air-cooled system that was initially proposed by General Atomics, as reported in Thielman *et al.* (2005). The second type is an active, cold (< 30ºC), constant water flow system proposed by AREVA, as reported in Lommers *et al.* (2012). For the second type, if forced circulation is lost, heat is removed by boiling and enough water inventory is present in the system to maintain vessel heat removal for 72 hours. The main benefit of the first system over the second is its reduced failure probability associated with any loss of fluid inventory, and indefinite capacity without forced circulation. For both systems, radiation and heat conduction occurs from the outer vessel wall, across the reactor cavity, to the RCCS risers where heat is carried away to the environment either via natural circulation open air ducts, as in the case of the General Atomics design, or via an intermediate heat exchanger connected to the environment, as in the case of the AREVA design. Both RCCS designs, adapted from Williams *et al*. (1989) and Lommers *et al*. (2012), are shown in Figure 2.5.

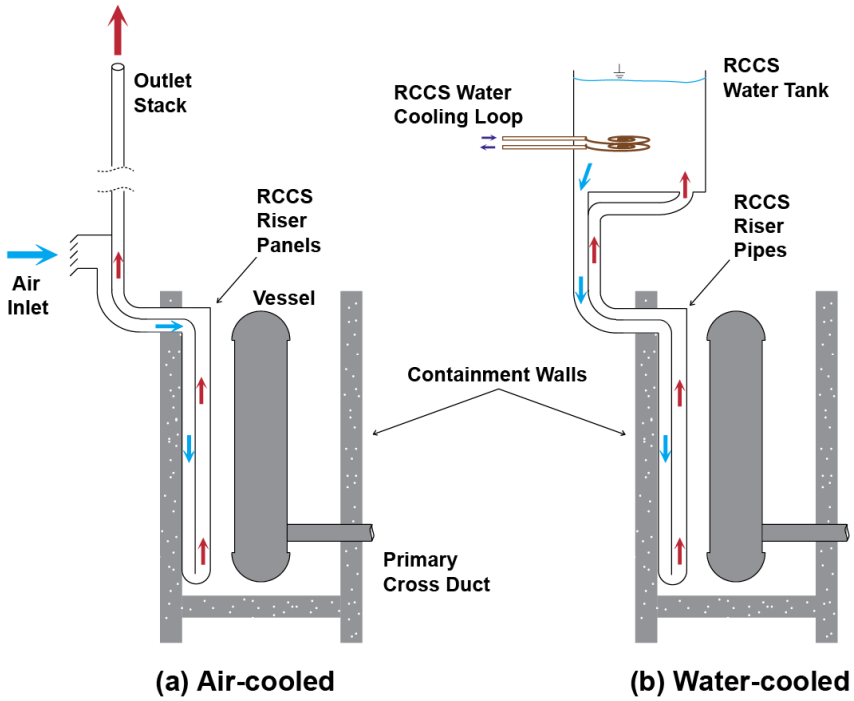

Figure 2.5 Passive RCCS Designs for HTGRs, (a) Adapted from Williams *et al.* (1989) and (b) Adapted from Lommers *et al.* (2012)

A small-scale (1:23) RCCS experimental test facility based on the water-cooled AREVA system was constructed at Texas A&M University. The purpose of this facility is to measure representative heat duties by the RCCS and to observe the flow distribution in the RCCS riser channels. Experimental results by Vaghetto and Hassan (2014) seem to confirm the ability of the RCCS to passively remove the required heat from the reactor vessel. Figure 2.6 shows a schematic of the experimental facility.

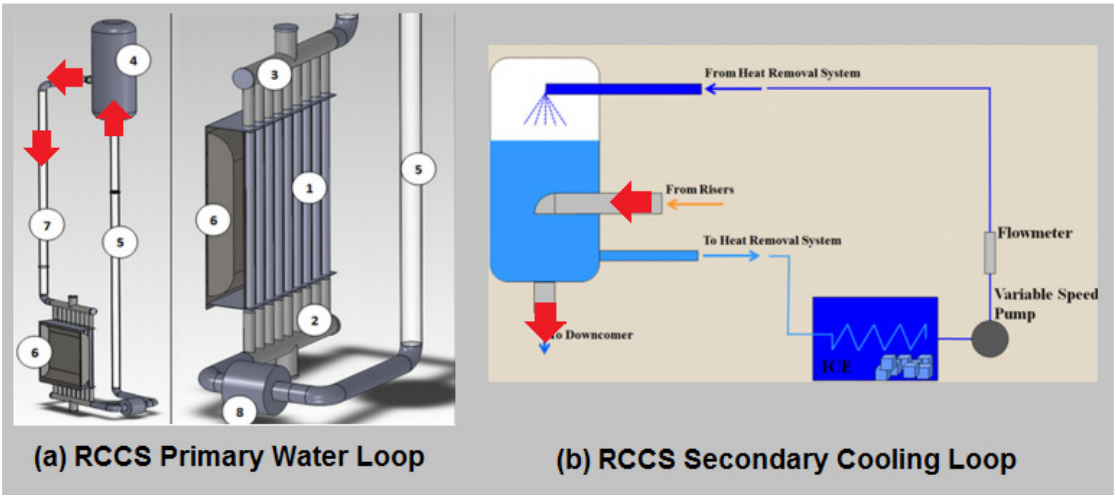

Figure 2.6 Experimental RCCS Facility as Described in Vaghetto and Hassan (2014).

RCCS water temperatures and flow rates were measured as $6\ kW$ of heat was applied to the vessel wall from electric heaters. Accounting for heat losses, about ~ $4.8\ kW$ was transferred across the test apparatus. A secondary loop connected to an ice-bath was used as the heat sink. Once steady state was achieved, secondary inlet and outlet temperatures were maintained around 27 and 31°C respectively, while primary RCCS water was measured at 31 and 33°C. These temperatures are not unique as they could be adjusted by increasing or decreasing the secondary flow rate through the ice-bath. The critical value of interest was the measured primary coolant flow rate through the loop. For these temperatures, at steady state, the flow rate was found to be ~32 $l/\min$. This corresponds to an average water velocity of $0.029\ m/s$ through each riser channel. However, there was non-uniform flow across the riser distribution manifolds due to flow geometry, and possible non-uniform heating due to thermal radiation.

Qualitative flow visualization at the riser inlet and outlet manifolds was performed to assess the flow distribution through each of the riser channels. It was observed that channels closer to the riser outlet have higher flow than channels closer to the riser inlet. This is most likely a result of the manifold or plenum geometry used in the experiment. Nevertheless, these observations could be valuable for VHTR RCCS design and possibly

selecting those channels with a higher imposed heat flux to have a higher flow rate. This would lower the average outer surface temperature, which is important for maximizing radiation heat transfer from the vessel. However, it may be more beneficial to minimize the total flow resistance of the system without preference to individual channels. More study is needed to adequately address all of the potential design tradeoffs for developing the RCCS.

A RELAP5-3D simulation was performed by Vaghetto and Hassan (2014) using the RCCS experimental configuration described above and in Figure 2.6. The purpose of this simulation was to support computer code verification and identify weaknesses and/or limitations of the code. One unique aspect of the study was the computation of radiation view factors using the NEVADA^{TM} software, T.A.C. Technologies (2000), and the combined mode heat transfer modeling of the RCCS panels and riser pipe fins. For the same experimental conditions, simulated cavity flowrates and temperatures were found to be in satisfactory agreement with the experimental data. Thus, it was judged by the authors that RELAP5-3D is acceptable for RCCS and vessel heat removal prediction.

Additionally, CFD simulations of the upper plenum vessel wall and RCCS cavity were performed by Frisani and Hassan (2014). This study had a similar purpose, to verify the commercial CFD software and its models (STAR-CCM+/V5.02.009) for RCCS simulation and vessel heat removal prediction. One benefit of CFD over experiments and RELAP5-3D is that detailed temperature distributions over the vessel and riser pipes can be computed. This could allow for optimization of RCCS panels and riser pipes. Seven cases were analyzed with varying system size/power, and pipe configurations. Six of the seven cases had a uniform inner vessel heat flux boundary condition of 3.75 kw/m^2. Five cases assumed a riser pipe uniform temperature boundary condition of 100^{o}C which corresponds to boiling of the RCCS riser water coolant. The other two assume forced convection in the riser pipes, one with a low flowrate (U_0 = 0.0114 m/s) and one with a high flowrate (U_0 = 0.0772 m/s). For all of the stagnant flow cases, maximum RPV wall

temperature ranged from 341 – 478ºC depending on riser pitch-to-diameter ratio, number of pipes and panel length modeled.

Using the outer vessel temperatures and heat flux values from the reference CFD simulations, inner wall and vessel helium conditions are estimated by hand calculation here. For the expected vessel steel, SA533, the thermal conductivity at 600ºC is around 43 W/m-K. This increases with lower temperatures, and is therefore a conservative value for the temperature range described here. The expected upper head vessel thickness is 15.6 cm. For the RPV outer wall temperatures above, and treating the RPV wall as a plane wall, this corresponds to steady state inner wall temperatures between 355 – 492ºC. The upper plenum helium temperature, based on the calculations and observations from experiments, is expected to be in the range of 600 – 1300ºC. For a heat flux of 3.75 kW/m^2, this corresponds to a necessary minimum helium convective heat transfer coefficient in the range of 4 – 12 W/m^2-K, assuming the helium can interact directly with the inner surface of the vessel head. Since average outer vessel wall temperatures are lower, roughly around 275ºC, the necessary minimum convective heat transfer coefficients are slightly lower.

For the VHTR at a decay power of 0.5% total operating power, a total of 1.75 MW must be removed from the vessel. Using the temperatures and expected heat transfer coefficients as described above, the fraction of heat removed by the upper vessel head is estimated by hand calculation here. The upper plenum inner surface area can be approximated as a half-sphere with only a faction available for active heat removal. Some of the upper head area is covered by control rod drive and fuel handling components. Conservatively, if 50% of the area is available (A ≈ 83 m^2), this leads to ≈ 311 kW or only 18% of the total heat generated being removed in the upper plenum. However, helium convective heat transfer coefficients should be slightly higher, at around 18 – 20 W/m^2-K. This would lead to slightly higher vessel surface temperatures and larger heat flux values through the upper plenum wall. If the wall heat flux is closer to 5 kW/m^2, then 23% or more of the total heat generated can be removed in the upper plenum. For either case,

considering the height of the vessel (h ≈12 m) and corresponding total vessel surface area, there is sufficient margin to remove the necessary power using the saturated water-cooled RCCS. Additional experimental testing is needed to verify these CFD models, as well as with higher or varying heat flux values through the upper head and vessel wall.

2.5 Additional Safety Concerns

For the HTGR, pressurized and de-pressurized LOFC accidents are the principal design basis accident scenarios, Ryskamp (2003). For these events to be successful (*i.e.*, fuel temperature does not exceed specified failure limits), there must be sufficient circulation in the vessel to transfer heat from the core to the vessel walls, and the RCCS must be capable of removing heat from the vessel wall to the environment. Preliminary experimental and CFD results, as described in the previous sections, show that this is possible for select steady state power levels, RCCS temperatures, and different RCCS designs. However, the core power is initially much higher than the powers used in the studies mentioned in the previous sections. There is also some transient heatup, and spatial variations are not considered in the previous studies. Additionally, there are some more complex material and chemical interaction accidents that could pose safety challenges for the HTGR. See papers by Oh and Kim (2010) for discussion and analysis of air ingress accidents and Zhang *et al*. (2005) for water ingress accidents.

The primary risk for air ingress occurs during a loss of coolant (LOCA) or pipe break scenario. The primary risk for water ingress occurs during a break of a connected system barrier (e.g., shutdown cooling system pipe) into the primary system. For either of these accidents, similar D-LOFC accident behavior is expected but with the addition of graphite oxidation reactions within the core. For air-ingress, cold environmental air, at 20-25^{o}C, is assumed to circulate through the vessel. Recent work by Haque (2008) shows that this lower temperature inlet air leads to lower expected maximum fuel temperatures, even with exothermic oxidation reactions, than for the D-LOFC accident without air ingress.

Similarly, for water-ingress accidents, core decay heat is still principally removed by the RCCS and the additional low temperature water sources act to reduce peak fuel temperatures. Reactivity is only a concern for water-ingress cases when the control rods fail to insert. For the MHTGR, small leak sequences (0.05 kg/sec) were found to have no or bounded calculation of radionuclide releases. Moderate leak sequences (5.7 kg/sec) force a reactor trip very early into the accident sequence on either moisture monitor detection or high power-to-flow ratio.

Based on the results presented by Oh and Kim (2010, 2011), Zhang *et al*. (2005), Haque (2008), Williams *et al*. (1989), fuel heat-up and peak fuel temperatures are not a larger concern for the air/water ingress cases than for the standard D-LOFC accidents. However, there are many other valid non-core thermal hydraulic concerns with these ingress accidents. Possibly the largest concern is the structural integrity of the lower plenum graphite post-oxidation, NGNP Moisture Ingress Assessment Committee (2011). Cracks and other defects could develop as a result of oxidation potentially leading to failure of core support structures. This could then lead to a number of different flow blockages and geometrical configurations that prohibit decay heat removal.

For the steam generator configured HTGR, this represents a significant water source if a break were to occur into the primary system. A potential hazard with water-ingress accidents is the generation of hydrogen gas. This phenomenon has been a thoroughly assessed issue for most LWR plants. For HTGRs, this has not been investigated and without hydrogen mitigation systems, hydrogen combustion could occur in the containment leading to failure of RCCS and other vital systems.

Fortunately a CFD study by Oh *et al.* (2011) showed that these safety concerns could be mitigated by an economically affordable and simple helium injection system. As little as 0.5 m/s helium injected in the lower plenum could reduce air concentrations from 50% to 15% or less. A 200 m^3 helium storage tank was estimated to last six days at that rate.

Considering all the possible safety solutions for non-LOFC accidents, it is critical to ensure that safety criteria are met for the LOFC accidents. Therefore, the principal effort in this dissertation is to model and simulate the HTGR under both D- and P-LOFC accidents. This work is significant considering: (1) there is a lack of non-CFD HTGR thermal-hydraulic methods that model the prismatic fuel assemblies in their original hexagonal arrangement, (2) fine mesh CFD methods are not equipped to simulate the whole core and primary system over the course of a long transient (100+ hours), and (3) realistic power profiles have not been fully employed in the various LOFC safety studies. The next chapter presents the transient unit-cell method and fluid procedures to simulate the core and the primary coolant system for the LOFC accidents.

3. PHYSICAL MODELING

The transient HTGR thermal hydraulic method developed here can be divided into two key areas: (1) the solid and fluid node heat transfer models, which are discussed in this chapter, and (2) the numerical scheme and associated boundary models, which are discussed in the following chapter. The key physical models described in this chapter include: (a) solid node graphite and fuel unit cell models, (b) transient core channel and vessel fluid models, and (c) the vessel heat structures, mainly the vessel wall for RCCS heat removal estimation.

The solid node graphite and fuel unit cell models are essentially the same as those described in Huning *et al.* (2016) and in Huning (2014). The transient fluid models are substantially different than those used for the steady state analysis. For steady state calculations, a simple uniform pressure drop condition across all the core channels dictated the mass flow distribution. It was also assumed that the RCCS did not impact the steady state temperature distribution; therefore, the vessel wall and other heat structures such as the cross duct, Shutdown Cooling System (SCS) walls, and connected Primary Conversion System (PCS) were not modeled.

There are many advantages of using the unit cell method and 1-D transient fluid models. The primary advantage is the ability of this method to compute whole core temperature distributions at any given time during the transient accident. This is not currently possible using CFD. Coarse systems-level codes such as RELAP can do this, but as will be shown in Chapter 6, significant fuel geometry assumptions must be made. Computational time is still a moderate concern as simulations can take a week or longer using a small cluster (8-24 nodes). Therefore, reducing the cell model dimensions beyond what are described here is not practical.

3.1 Unit Cell Modeling Approach

The solid node graphite and fuel unit cell modeling approach is described here. The purpose of this modeling approach is to compute the transient temperature profile within the graphite and fuel of the active core hexagonal fuel assembly blocks and solid reflector blocks. The prismatic HTGR reactor core consists of stacked hexagonal graphite assembly blocks with inner and outer reflector regions and a middle active core region as shown in Figure 1.1. Each fuel assembly has alternating fuel and coolant channels and is either a standard fuel assembly or a control fuel assembly with a single large hole reserved for a system shutdown or control rod. Both fuel assembly types are shown in Figure 1.2. Fuel and reflector assemblies also contain a central handling hole used to position blocks around the core. Burnable poison pins, which control reactivity over the fuel cycle, are placed on the corners of assemblies. The unit-cell discretization methodology is shown schematically in Figure 3.1, while representative unit cell geometries containing a fuel pin are shown in Figure 3.2.

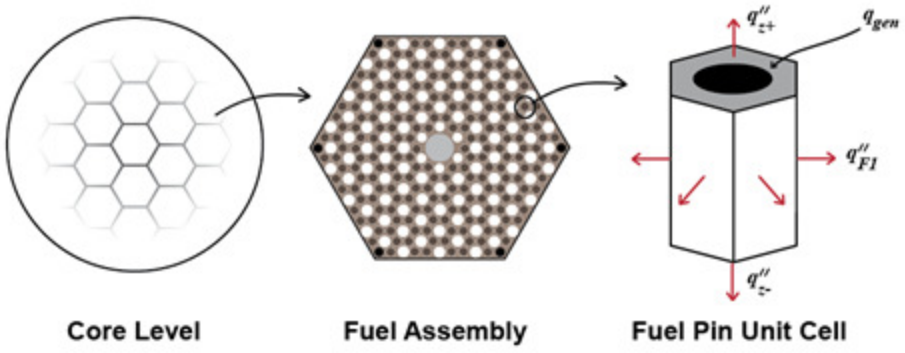

Figure 3.1 Unit Cell Discretization Methodology

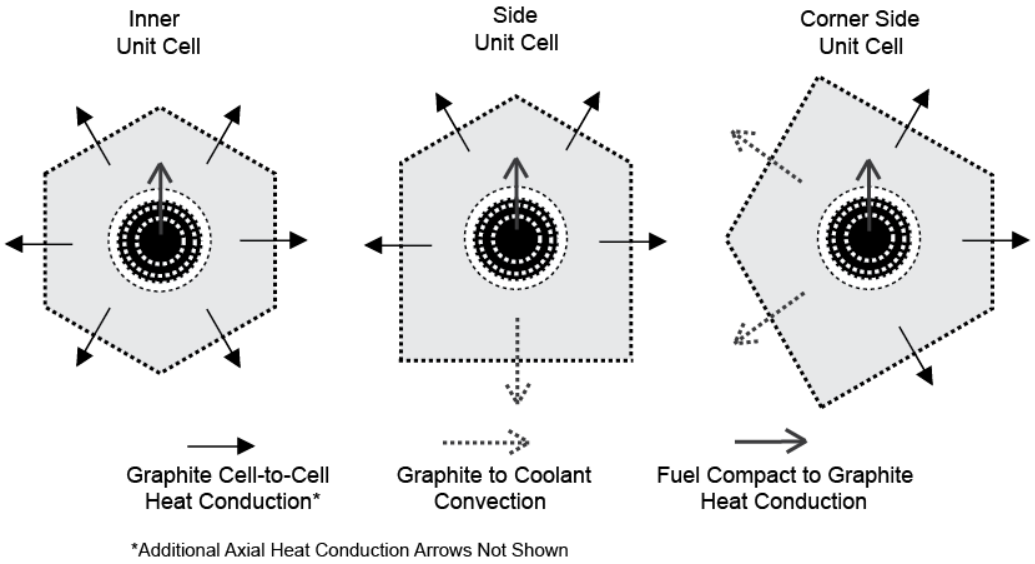

Figure 3.2 Representative Unit Cell Geometries Containing a Fuel Compact

The differential thermal energy equation within a graphite or cylindrical fuel cell is given by Eq. (3.1) where T is the temperature at some spatial point, t is time, $\mathbf{q}$ is heat flux, ρ is density, c_P is specific heat and q'''_{gen} is volumetric energy generation rate.

$$\rho c_P \frac{\partial T}{\partial t} = -\nabla \cdot \mathbf{q} + \mathrm{q}'''_{gen} \tag{3.1}$$

Averaging over the unit cell volume, the differential thermal energy equation is transformed into Eq. (3.2). For Eq. (3.2), an inner unit cell geometry is assumed since the number of sides for heat conduction is eight (six radially and two in the axial direction). The unit cell interfacial area is denoted by $\mathbf{a}_s$, and the unit cell volume is denoted by V.

$$\rho c_P \frac{\partial T_{ave}}{\partial t} = -\frac{1}{V}\sum_{s=1}^{8} \mathbf{q}_s \cdot \mathbf{a}_s + \mathrm{q}'''_{gen,ave} \tag{3.2}$$

The heat flux between unit cells is approximated using a first-order Fourier's law approximation given in Eq. (3.3).

$$\mathbf{q}_i = -k_{ave} \frac{T_2 - T_1}{l} \tag{3.3}$$

Thus for a given initial temperature distribution, the new temperature distribution can be found by substituting Eq. (3.3) and integrating both sides of Eq. (3.2). More information about the time integration scheme employed can be found in the next chapter. Specific design values and dimensions for the MHTGR core, vessel and unit cell discretization can be found in Table 3.1.

Table 3.1. Relevant MHTGR Design Parameters

Core and Vessel Configuration		
# Fuel Compacts	13572	-
# Large Coolant Channels	6564	-
# Small Coolant Channels	408	-
# Bypass Gaps	751	-
Upper Plenum Flow Area	4.24	m^2
Riser Flow Area	1.21	m^2
Lower Plenum Flow Area	3.45	m^2
Upper Plenum D_H	0.143	m
Riser D_H	0.247	m
Lower Plenum D_H	0.586	m
Riser Height	11.9	m
Fuel Assembly Design		
Assembly Flat-to-Flat Diameter	0.36	m
Fuel Compact Diameter	12.45	mm
Fuel Compact Gap Width	0.30	mm
Large Coolant Channel Diameter	15.86	mm
Small Coolant Channel Diameter	12.70	mm
Unit Cell Discretization Parameters		
Unit Cell Pitch	18.80	mm
Inner Unit Cell Side Length	10.85	mm
Inner Unit Cell Side Surface Area	$8.604 \cdot 10^{-3}$	m^2
Number of Axial Zones	10	-
Unit Cell Axial Height	0.793	m

3.2 Initial Temperature and Power Distributions

For steady state calculations, the volumetric energy generation rate is held to the constant design specified level. An arbitrary initial temperature distribution is assumed and the final converged, steady state temperature distribution is achieved after a number of

time-steps when the heat generation rate matches the heat removal rate by core helium convection. For transient calculations, this computed steady state temperature distribution is used as the initial temperature distribution. The temperature distribution then changes over time as the heat generation rate changes.

The initial temperature distribution used for all of the transient LOFC cases presented here is the result of a detailed coupled neutronics analysis by Connolly *et al.* (2016). In this paper, the movement of control rods was investigated and a near-critical configuration for the MHTGR was found. The specific control rod configuration is shown in Figure 3.3.

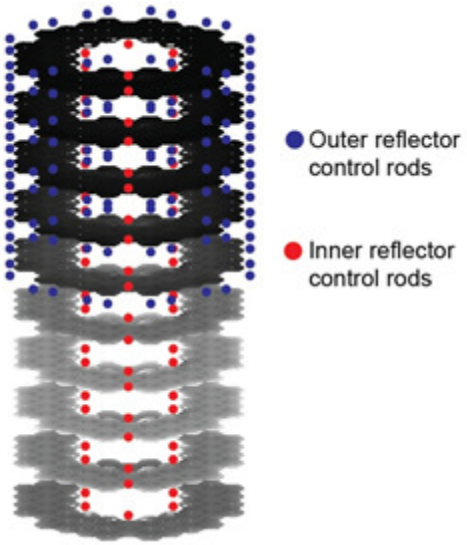

Figure 3.3 MHTGR Near-Critical Control Configuration

This configuration was found by first performing a steady state coupled thermal-hydraulic and neutronics analysis with a reactor configuration with no control rods inserted. Control rods are grouped into two batches: inner reflector rods, and outer reflector rods. After performing several separate steady state coupled analyses with different control rod patterns, it was determined that the configuration shown in Figure 3.3 was the most optimal. This was determined to be the most optimal since it was the case with a core-eigenvalue closest to unity ($k \approx 1$). Rods were inserted in $1/10^{th}$ increments to minimize

the number of potential coupled analysis cases while still having enough movement resolution to achieve near-criticality.

From the coupled analysis with control rods inserted as shown in Figure 3.3, the 3-D power and temperature distributions were obtained. The power distribution is shown in Figure 3.4. For the transient analysis, this represents the initial power distribution at time zero.

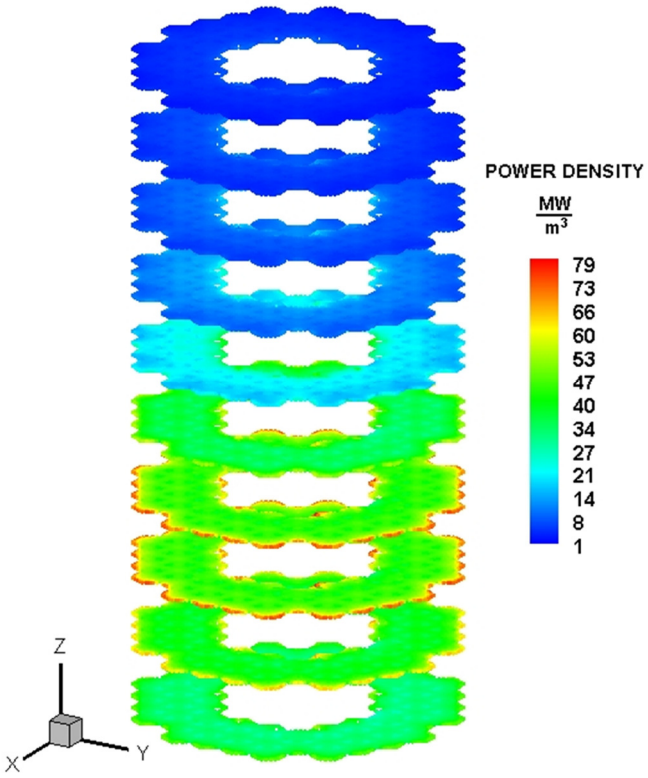

Figure 3.4 MHTGR Initial Fuel Power Level and Distribution

Without inner control rods inserted completely, the power peaks significantly along the inner reflector block fuel region. As shown in Figure 3.4, the power now peaks along the outer reflector block fuel region. This is expected since the outer control rods are removed at this location in the core. Since the MHTGR is a thermal spectrum reactor, the graphite reflector blocks are considerably important for thermalizing the fast neutrons emitted during fission. As neutrons become more thermalized, their mean-free-path, or

their ability to penetrate material, becomes smaller and they are subsequently absorbed by the Uranium based TRISO fuel along the outer reflector block periphery. The fuel temperature distribution corresponding to this case is shown in Figure 3.5.

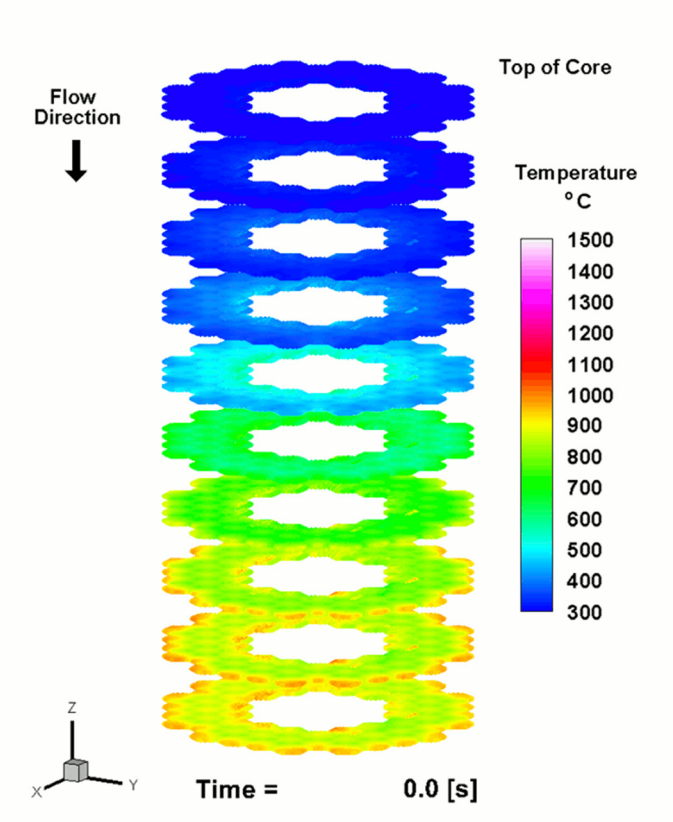

Figure 3.5 MHTGR Initial Fuel Temperature Distribution

Coolant enters the top portion of the core and exits at the bottom. Thus, the fuel temperature, as shown in Figure 3.4, also increases from top to bottom. It can be clearly seen that the steady state fuel temperature distribution is influenced by the power distribution. Steady state results for a variety of different sensitivity studies and expanded discussion can be found in Huning *et al*. (2016). For the transient cases, this influence is minimized since the overall decay power level drops to a fraction of the steady state power.

3.3 Transient Fluid Modeling

For steady state, the coolant distribution entering the core at the top of the vessel is determined by preforming a pressure drop balance, and then setting it equal across all the

channels and bypass gaps. For the MHTGR, a standard CFD procedure is used to compute both the pressure and flow distribution across the core. The complete procedure is described in Matrineau and Berry (2004). The main difference between that work and the method described here is the approximation of 1-D channels for MHTGR fluid volumes.

The fluid volumes for the MHTGR include: small and large coolant channels within the graphite assembly blocks, flat channel bypass gaps between the hexagonal assembly blocks, the upper and lower plenums, and a riser channel. These volumes are shown in Figure 3.6.

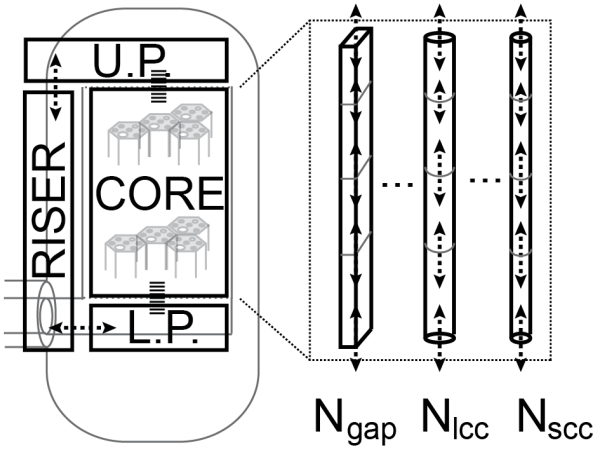

Figure 3.6 MHTGR Fluid Volumes

The core fluid volumes are discretized into increments similar to the solid nodes, typically ten axial segments. The nodes are approximated as 1-D since the flow in either normal operation or shutdown is primarily in one loop direction. In Figure 3.6, for steady state normal operation, the junction linking the lower plenum (L.P.) and the riser does not exist. Instead, the L.P. connects to an outlet plenum. However, since shutdown and loss of flow accident cases are the ones primarily considered here, this L.P. to riser junction was introduced to simplify the fluid transport around the vessel. In the MHTGR, and it is expected for other HTGR designs as well, there will be additional lower volumes in the base of the vessel for forced circulation, shutdown cooling systems. These are not expected

to be functional for any of the events considered here, and can be safely neglected since these additional volumes do not participate in heat transfer away from the core nor are they large enough to significantly impede the recirculation flow.

The goal of the transient fluid modeling is to provide convective heat transfer estimates in the core as well as to the vessel wall. This is accomplished by using standard heat transfer correlations for the applicable flow regime. This convective heat removal rate is then subtracted/added to surrounding core graphite as well as added/subtracted from the helium energy. The helium energy calculation is performed simultaneously with other fluid equations for mass and momentum. The solid node energy calculations are performed independently during a larger time-step. A description of the time-step implementation for the fluid and solid node calculations is included in the next chapter.

The general method is adapted from Matrineau and Berry (2004). In this paper, the pressure-corrected implicit continuous-fluid Eulerian finite element method (PCICE-FEM) for compressible ideal gas, 2-D geometry is described in detail. The main benefit of this computational fluid dynamics (CFD) scheme compared to other semi-implicit or fully implicit schemes, is that the energy equation is sufficiently coupled to the pressure equation through the equation of state, or ideal gas equation, to avoid excessive outer iterations common to other schemes without energy equation coupling.

Several simplifications and assumptions are made to this method to allow for HTGR, whole-vessel flow distributions to be calculated. The first assumption is that fluid volumes can be treated as 1-D. This significantly reduces the number of meshes and calculations. It also allows for well-established heat transfer and pressure drop correlations to be used. The second assumption is that finite difference versions of the governing equations are solved, instead of finite-elements. The third is that smoothing of explicit predictor terms with artificial dissipation is neglected. In this section, a summary of the PCICE method as applied to HTGRs is presented.

A staggered grid is used for the momentum equation. The mass and energy equations are solved using the discretization shown in Figure 3.6. However, for the momentum equation, volumes are positioned over the inlet and outlets of the volumes used for the mass and energy calculations. The primary benefit is that the fluid velocity at the inlet/outlets, which is more critical to the mass and energy conservation, can be computed. This is shown in Figure 3.7.

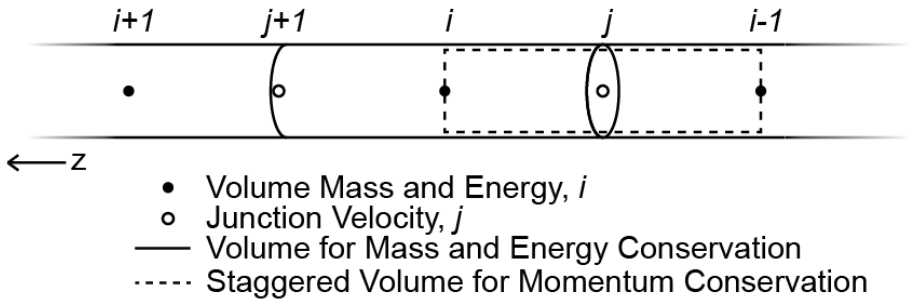

Figure 3.7 Staggered Grid Fluid Discretization

Additional velocities, such as the ones at points "i" or "i+1", can be computed from linear interpolation. Similarly, for mass and energy, interpolation is used for the values at points "j" or "j+1". It should be noted that the fluid pressure (P) is computed on the same grid as the mass/energy (the "i" points).

The fluid governing equations for mass, momentum, and energy are listed in Eq. (3.4) through Eq. (3.6). The principal variables of interest are: density (ρ), velocity (u), and specific fluid energy (e) where: $e = i + u^2/2 + gz$, $i =$ "internal energy", and $gz =$ "gravitational energy".

$$\frac{\partial \rho}{\partial t} + \nabla(\rho u) = 0 \qquad \text{Eq. (3.4)}$$

$$\frac{\partial(\rho u)}{\partial t} + \nabla(\rho u \cdot u) = \rho g_z - \nabla P - F_f \qquad \text{Eq. (3.5)}$$

$$\frac{\partial(\rho e)}{\partial t} + \nabla(\rho u \cdot e) = q_{H.T} \qquad \text{Eq. (3.6)}$$

Several assumptions are made to present the governing equations in this form. These include: (1) single component, single phase helium, (2) the viscous and surface frictional forces are encapsulated in the variable, F_f, (3) no thermal dissipation, and (4) heat transfer between the fluid and surface is captured by the variable, $q_{H.T.}$. Additionally, helium is assumed to be a perfect, ideal gas with constant specific heats (at constant pressure, $c_P = 5193$ [J/kg-K], and at constant volume, $c_V = 3116$ [J/kg-K]). This assumption allows for easy determination of the fluid temperature via the internal energy ($\Delta i = c_V \Delta T$). The corresponding pressure can also be easily computed from Eq. (3.7) which is derived from the ideal gas law.

$$P = \left({}^{c_P}\!\!\diagup\!\!{}_{c_V} - 1 \right) \cdot \rho \cdot i \qquad \text{Eq. (3.7)}$$

The volumetric heat transfer variable, $q_{H.T.}$, for some volume "j" is shown below in Eq. (3.8) where: $A_{H.T.}$ and T_{surf} are the surface area and temperature respectively, V_j and $\overline{T}_j$ are the fluid volume and average fluid temperature respectively, and $\overline{h}_{conv}$ is the average convective heat transfer coefficient for the corresponding flow regime in the volume.

$$q_{H.T.} = \frac{A_{H.T.}}{V_j} \overline{h}_{conv} \left(T_{surf} - \overline{T}_j \right) \qquad \text{Eq. (3.8)}$$

The heat transfer coefficients for laminar ($\mathrm{Re} < 2100$) and turbulent flow ($\mathrm{Re} \geq 2100$) for the core coolant channels can be computed from the laminar constant heat flux expression or the Churchill (1977) equation shown in Eq. (3.9) and Eq. (3.10), respectively.

$$\overline{Nu} = \frac{\overline{h}_{conv} D_H}{k} = 4.364 \qquad \text{Eq. (3.9)}$$

$$\overline{Nu}^{10} = \left(4.364^{10} + \left[\frac{exp\left(\frac{2200 - \mathrm{Re}}{365} \right)}{4.364^2} + \left(6.3 + \frac{0.079 \cdot \left(f/8 \right)^{0.5} \cdot \mathrm{Re} \cdot \mathrm{Pr}}{\left(1 + \mathrm{Pr}^{0.8} \right)^{5/6}} \right)^{-2} \right]^{-5} \right) \quad \text{Eq. (3.10)}$$

For Reynolds numbers less than 2100, Eq. (3.10) reduces to Eq. (3.9), but Eq. (3.9) is used instead to reduce the mathematical operations associated with Eq. (3.10). The frictional pressure drop variable, F_f, in Eq. (3.5) and friction factor (f) used in Eq. (3.10) can be determined from Eq. (3.11) and either Eq. (3.12) or Eq. (3.13) for laminar and turbulent flow respectively.

$$F_f = \frac{f}{D_H} \frac{\rho u^2}{2} \quad \text{Eq. (3.11)}$$

$$f_{\text{lam.}} = 64/\mathrm{Re} \quad \text{Eq. (3.12)}$$

$$f = 8 \cdot \left[\left(\frac{8}{\mathrm{Re}_{D_H}} \right)^{12} + \left\{ \left(2.457 \ln \left(\left[\left(\frac{7}{\mathrm{Re}_{D_H}} \right)^{0.9} + 0.27 \frac{\varepsilon_s}{D_H} \right]^{-1} \right) \right)^{16} + \left\{ \frac{37{,}530}{\mathrm{Re}_{D_H}} \right\}^{16} \right\}^{-3/2} \right]^{1/12} \quad \text{Eq. (3.13)}$$

Graphite surface roughness (ε_s) is dependent on various factors; therefore, an approximation of $\varepsilon_s = 10[\mu m]$ is used in this method for simplicity.

As is common to many computational fluid dynamics methods, the fluid pressure cannot be explicitly determined from the solution of just the governing equations in Eq. (3.4), Eq. (3.5), and Eq. (3.6). The pressure distribution is determined simultaneously through the use of a "pressure – correction" (Poisson) equation. This equation is derived in Matrineau and Berry (2004) and is shown here in Eq. (3.14) as a starting point along with the already presented fluid conservation equations and thermodynamic relationships. Key variables shown in Eq. (3.14) and used throughout the method are listed in Table 3.2.

$$\frac{\delta \mathrm{P}}{\varphi R\hat{T}} - \varphi \Delta t^2 \underline{\nabla} \cdot \underline{\nabla}\left(\delta \mathrm{P} + \mathrm{P}^n\right) = \frac{\hat{\rho}}{\hat{T}}\left(T^* - T^n\right) - \Delta t \underline{\nabla} \cdot \left(\left(\rho \underline{u}\right)^{*,n+\varphi}\right) \qquad \text{Eq. (3.14)}$$

Table 3.2. Transient Fluid Variables and Parameters

Discretization Parameters

Variable	Description	Units
Δt	Time-step size (typically ~0.001s)	s
n	Current time-step number (these are known quantities)	-
φ	Partial time-step advancement size ($0 < \varphi < 1$, typically ~0.5)	-
$n+\varphi$	Next partial time-step	-
$n+1$	Next time-step number	-
x^*	Explicitly computed next time-step scalar quantity "x"	x
$\hat{x}$	Explicit partial time-step scalar quantity "x": $\hat{x} = \varphi x^* + (1-\varphi) x^n$	x
δx	Explicit change of "x": $\delta x = \left(x^{n+\phi} - x^n\right) \cdot \varphi^{-1}$	x

Fluid Variables and Properties

P^n	Current time-step (mass-centered) pressure	Pa
$\overline{\mathrm{P}}$	Corrected next time-step pressure	Pa
$\delta \mathrm{P}$	Hybrid pressure, defined as: $\delta \mathrm{P} = \varphi\left(\overline{\mathrm{P}} - \mathrm{P}^n\right)$	Pa
T	Temperature (mass-centered)	K
ρ	Density (mass-centered)	kg/m^3
R	Helium ideal gas constant: $R = c_P - c_V = 2077$	$J/kg \cdot K$
$(\rho \underline{u})$	Mass flux (staggered grid)	$kg/m^2 s$
(ρe)	Fluid volumetric energy (mass-centered)	J/m^3

Eq. (3.14) is then interpreted for the specific fluid volumes of interest. These include: core coolant channels with similar flow areas and lengths, and upper/lower plenums, which connect to the core coolant channels but have differing geometric parameters. Each core coolant channel is assumed to have only one "inlet" and "outlet". For this simple case, the Poisson equation in Eq. (3.14) is transformed into Eq. (3.15) with the flow/node length (L) subscripts: $j-1$ representing the upstream node, j being the

current node, and $j+1$ being the downstream node. Staggered grid (boundary) mass flux subscripts j_{in} and j_{out} refer to the inlet and outlet respectively.

$$\frac{L_j \cdot \delta \mathrm{P}_j}{\varphi R \hat{T}_j} + \varphi \Delta t^2 \left(\frac{2}{L_{j-1} + L_j} \right) \left(\delta \mathrm{P}_j - \delta \mathrm{P}_{j-1} \right) + \varphi \Delta t^2 \left(\frac{2}{L_{j+1} + L_j} \right) \left(\delta \mathrm{P}_j - \delta \mathrm{P}_{j+1} \right) = \frac{L_j \hat{\rho}}{\hat{T}_j} \left(T_j^* - T_j^n \right) + \Delta t \left(\rho \underline{u} \right)_{j_{in}}^{*,n+\varphi} - \Delta t \left(\rho \underline{u} \right)_{j_{out}}^{*,n+\varphi} + \varphi \Delta t^2 \left(\frac{2}{L_{j-1} + L_j} \right) \left(\mathrm{P}_{j-1}^n - \mathrm{P}_j^n \right) + \varphi \Delta t^2 \left(\frac{2}{L_{j+1} + L_j} \right) \left(\mathrm{P}_{j+1}^n - \mathrm{P}_j^n \right) \quad \text{Eq. (3.15)}$$

If the core coolant channel nodes are the top or bottom, then the appropriate plenum lengths and pressures are substituted into Eq. (3.15). The Poisson equations for the upper and lower plenum are similar, but boundary conditions for mass flux or pressure are used to put the system into a solvable system for all the mass-centered hybrid pressure terms (δP_j). The set of Poisson equations is then combined into a linear system of the form: $[A] \cdot [\delta P] = [B]$. The system is solved using a simple Gaussian elimination method. Once all the hybrid pressures are known, the corrected pressure is computed ($\overline{\mathrm{P}} = \varphi^{-1} \cdot \delta P + \mathrm{P}^n$). The corrected values for density, junction mass flux, and fluid energy can then be computed using Eq. (3.16) through Eq. (3.18) respectively. The complete procedure is outlined in Table 3.3.

$$\rho^{n+1} = \rho^{*,n+\varphi} - \varphi \Delta t \cdot \nabla \cdot \left[\left(\rho \underline{u} \right)^{n+1} - \left(\rho \underline{u} \right)^* \right] \quad \text{Eq. (16)}$$

$$\left(\rho \underline{u} \right)^{n+1} = \left(\rho \underline{u} \right)^* - \Delta t \cdot \nabla \left(\delta \mathrm{P} + \mathrm{P}^n \right) \quad \text{Eq. (17)}$$

$$\left(\rho e \right)^{n+1} = \left(\rho e \right)^{*,n+\varphi} - \varphi \Delta t \cdot \nabla \cdot \left[\left(\rho \underline{u} \right)^{n+1} \left\{ \frac{\left(\rho e \right)^{*,n+\varphi} + \overline{\mathrm{P}}}{\rho^{n+1}} \right\} - \left(\rho \underline{u} \right)^* \left\{ \frac{\left(\rho e \right)^n + \mathrm{P}^n}{\rho^n} \right\} \right] \quad \text{Eq. (18)}$$

Table 3.3 Transient Fluid Procedure

Beginning of time-step "n"

1	Solve for the explicit partial time-step values: $\rho^{n+\varphi}$ and $(\rho\underline{u})^{n+\varphi}$ from Eq. (3.4) and Eq. (3.5)
2	Compute $\delta\rho$ and $\delta(\rho\underline{u})$
3	Estimate convective heat transfer, $q_{H.T.}$, at $n+\varphi$
4	Solve for the explicit energy terms: $\delta(\rho e)$ and $(\rho e)^{*}$ using Eq. (6)
5	Compute all remaining fluid properties (ex. $\hat{T}, T^{*}, \hat{\rho}, \rho^{*}, \ldots$)
6	Solve for δP and $\overline{\text{P}}$ using the appropriate forms of Eq. (14)
7	Solve for the "corrected" values: ρ^{n+1}, $(\rho\underline{u})^{n+1}$, and $(\rho e)^{n+1}$
8	Compute all new time-step thermodynamic and fluid property quantities from the newly computed density and energy using their respective relationships

Proceed to next fluid time-step "n+1"

The key accident scenarios of interest are the pressurized and depressurized LOFC accidents. For each case, it is assumed that pressure and flow equilibrium is quickly established after the forced circulation ceases. For the pressurized case, this means that the vessel is initially at the normal operating pressure (6.39 MPa) and the velocity is zero. For simplicity, the initial helium temperature is set to the graphite surface temperature of that node. The pressure distribution in the core initially is computed during the first fluid time-step as outlined in Table 3.3.

For the depressurized case, the vessel pressure is set to 1 MPa. The equilibrium pressure for the D-LOFC case is highly dependent on the containment volume and thermal-fluid conditions. Containment design for the MHTGR is unclear and is an ongoing engineering project for many other HTGR designs. Therefore, it is preferable to assume a break boundary pressure rather than a specific containment design to generalize the transient and accident sequence. To determine what the vessel boundary pressure and thermal conditions during a D-LOFC will be, the following principal containment

parameters of interest should be specified: free gas volume, failure pressure, gas composition (helium/air/nitrogen), initial pressure, initial temperature, vessel and break elevation relative to the containment, break orientation and size, and containment height. Other geometry factors could be important, depending on the specific containment-vessel interaction and fluid flow. If the complete containment specifications and break geometry are known, the best method for determining the boundary conditions within the vessel would be to perform a detailed CFD simulation within the containment which includes a RCCS heat removal model.

Without knowing the containment geometry, another critical assumption for the D-LOFC is made. This assumption is to neglect mass, energy and momentum transfer between the vessel fluid and the containment fluid. This implies that the fluid exiting the vessel is immediately returned at the same state. This is a conservative estimate since some of the fluid energy exiting the vessel will be transferred to the containment walls and ultimately the environment. Thus for the D-LOFC case, it is assumed that all the heat from the core must be removed from the RCCS and not by any external containment gas or cooling system.

However, if complete containment failure does occur (pressure drops to 1 atm) and helium recirculation back to the vessel fails, this could ultimately lead to fuel failure. The containment of any nuclear reactor design or type is typically designed to withstand any vessel or primary system pipe break. Thus, these very low pressure conditions are less probable, will ultimately be classified as “beyond design basis”, and are outside the scope of the analyses presented here.

3.4 RCCS Modeling

The Reactor Containment Cooling System (RCCS) is responsible for cooling the reactor in the event the Power Conversion Unit (PCU) and Shutdown Cooling System (SCS) are unavailable. The SCS consists of a helium circulator that forces the primary

coolant through a heat exchanger that is cooled by low-temperature water on the secondary side. The PCU also consists of a helium circulator that forces the primary coolant through a heat exchanger (either a steam generator or turbo-generator) which is externally cooled. For a loss of all onsite and offsite power, neither the PCU nor SCS will be operational. Realistically, this will require the failure of onsite diesel power generators, batteries, or the electric transmission system in addition to the loss of offsite power. There are several possible, low probability initiating events that could lead to this configuration, also called a Station Blackout (SBO). The most recent, highly observed SBO event was the earthquake and subsequent tsunami that crippled the Fukushima Daiichi nuclear plant. Under an SBO, the RCCS is responsible for cooling the reactor to prevent a severe accident.

The RCCS operates by removing heat from the core by either air or water circulation along the containment walls. The air-cooled RCCS is a natural circulation system that draws cool air from the environment at a low elevation, it heats up along the containment wall that is underground, and then travels upward out an exhaust stack at a higher elevation. Figure 3.8 shows the air-cooled RCCS arrangement.

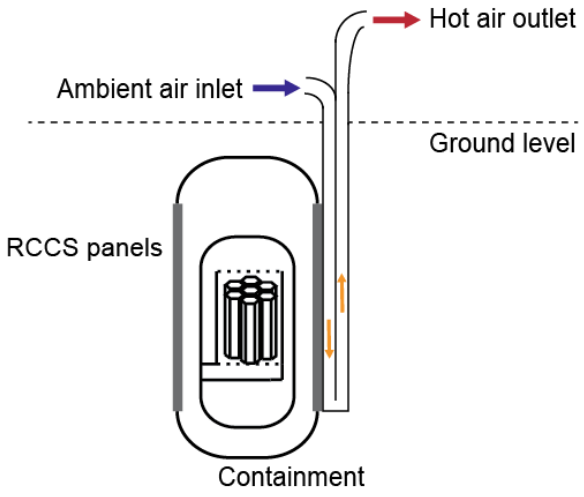

Figure 3.8 Air-Cooled RCCS Arrangement

The water-cooled RCCS design relies on a large water volume above the containment walls at atmospheric pressure. As the containment walls heat up, the water evaporates and is released to the environment. The water volume is designed to be large enough to cool the containment walls for an extended period of time, typically around 3-7 days. It should be noted that this water-cooled system is similar to what the Westinghouse AP-1000 design relies on for passive containment cooling.

In an LOFC, the reactor core and vessel heats up, thermal radiation and heat conduction occur in the containment between the vessel and containment walls. As the containment walls are cooled, the vessel cools down accordingly. Thus for a fixed containment, RCCS, and vessel design, heat removal from the RCCS is only coupled to the vessel wall. For simulating the transient and LOFC accidents, RCCS heat removal can be assumed to occur at the external vessel wall surface. This assumes the RCCS and containment materials have negligible thermal capacitance. For long or slowly progressing transients, the temperatures within these materials are assumed to be near steady state.

The MHTGR-350 design is assumed for the analyses presented here. In that reactor design, the air-cooled RCCS design is used. Using the assumption that the RCCS heat removal occurs at the vessel wall, RCCS performance is correlated as a function of external vessel wall temperature only. Using the LOFC results in the MHTGR preliminary safety documents, see Williams *et al*. (1989), the RCCS performance is correlated to vessel temperature as shown in Figure 3.9.

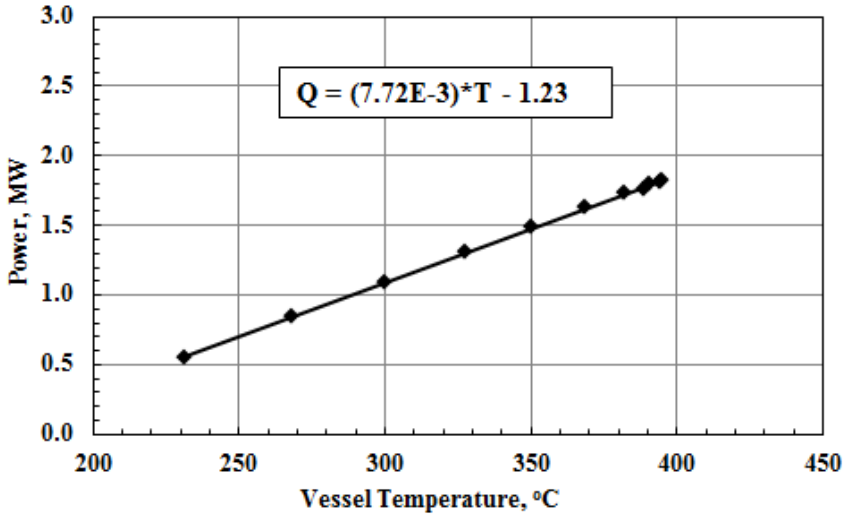

Figure 3.9 RCCS Performance as a Function of Vessel Temperature

This correlation for RCCS performance is used for the LOFC analyses presented here. This is done for a multitude of different reasons. The primary reason is that verifying RCCS performance and containment design can be achieved independently without considering the response from the core during an LOFC. Since RCCS performance is only coupled to the vessel wall, thermal-fluid experiments and CFD studies can easily be performed to verify RCCS heat removal. Several studies by Vaghetto and Hassan (2014) and others have shown that a sufficiently designed RCCS is capable of removing the necessary heat from the vessel wall.

The linear relationship in Figure 3.9 is somewhat unexpected since thermal radiation for a blackbody is function of surface temperature to the fourth power. Since this is an air-cooled RCCS design, the containment wall temperature increases as the vessel wall temperature increases. This is in contract to the water-cooled RCCS design which maintains a nearly constant containment wall just above 100°C. Heat transfer between the vessel and containment wall is not exclusively by thermal radiation. Heat conduction is also present, which is linear with increasing temperature for constant thermal properties.

These two effects are the principal contributors to the RCCS performance relationship shown in Figure 3.9.

For future HTGR designs, this curve presents some motivation for using a water-cooled RCCS design that would in principle have better performance at higher vessel temperatures than the air-cooled design. The major concern with the water-cooled RCCS is maintaining an intact source or volume of water. However, this may not be a concern if other water sources are nearby. Since this water would not come into contact with the reactor core, it can be assumed that there would be fewer restrictions on water quality than for typical LWR cooling systems. This could allow for common sources such as a lake or river possibly for RCCS cooling in the event the onsite volume of water was disrupted. However, to consider this as a passive system, a gravity driven system must be employed between the source and the RCCS. Additionally, there may be some concern with the air-cooled system if the exhaust stack were destroyed. Without the additional height, recirculation could be affected. These RCCS issues are still a concern and should be addressed before any HTGR is certified.

3.5 Summary of Critical Assumptions

Most of the assumptions up to this point have been discussed along with the particular method being described in their representative chapter/section. This section reviews some of the more critical assumptions and lists some not previously mentioned.

These assumptions are categorized by: modeling decision, neutronic, thermo-fluid, and numerical assumptions. Modeling decision assumptions refer to potentially important components and structures that were not chosen to be modeled in the LOFC simulations. Any components or structures not listed in this table are already modeled, such as the core fuel, graphite, select vessel volumes and walls, are not considered to be important to the safety of the HTGR. These could include features such as reactor building volumes not part

of containment, non-safety related pumps, balance-of-plant components that would be isolated from the primary system during accidents, and other plant systems.

Neutronic assumptions refer to what the initial and transient power distribution and magnitude are at steady state and shutdown conditions. The core neutronics and the coupled thermal hydraulic-neutronics work presented here, as well as in Huning (2014), and in Connolly *et al.* (2016), are focused on the computation of realistic steady state power and temperature distributions. The transient (shut-down) power distribution is assumed to be identical to the steady state distribution, since the heat that is generated is primarily due to the decay of fission products produced during normal operation. The total core heat generation rate is a function of time as the fission products decay. This specific function used for decay power is listed as a critical assumption.

Thermo-fluid assumptions include those relating to the manner in which the solid material temperatures, and thermo-fluid parameters are computed for the selected components and structures.

Table 3.4 describes the most critical assumptions used in the analysis of HTGR – LOFC accidents. Each successive assumption within each of the three sections is less important than the previous one. Therefore, Table 3.4 can also be used to aid in the selection of future improvements to the method developed here and the corresponding LOFC analyses.

Table 3.4 List of Critical Assumptions

Modeling decision assumptions

No.	Description	Impact
1	Model only convective heat transfer by the helium coolant in the riser channel between the vessel wall and core	Higher predicted core temperatures since radiation and conduction across gap will aid in vessel heat removal
2	Static D-LOFC containment –vessel equilibrium pressure of 1 MPa	Containment volume modeling will allow for additional heat removal to containment gas
3	RCCS heat removal as a function of outer vessel wall temperature	Along with containment modeling, this would reduce the number of external calculations and models
4	SCS or connected primary conversion system doesn't interact with core helium	Additional material (mass) would reduce core helium temperatures

Neutronics assumptions

5	No coupled fuel-depletion calculations	Initial power distributions are typically under-peaked compared to end-of-cycle distributions
		Standard (LWR) ANSI decay heat generation curves must be used instead of HTGR specific decay heat generation profiles

Themo-fluid assumptions

6	1-D vessel volume models	3-D fluid modeling in the non-core, vessel volumes would yield a more accurate heat transfer estimate to the vessel wall and ultimately the RCCS
7	Material properties are independent of radiation fluence	Graphite density, thermal conductivity decreases as radiation exposure is increased
8	Single component gas fluid	Helium will not be 100% pure during normal operation
		Oxygen and water vapor can cause graphite oxidation which would alter the local heat transfer performance
9	Fuel dimensions are "as-manufactured"	During normal operation the fuel compacts will shrink, swell, and crack. This will lead to higher local peak temperatures
10	Helium is an ideal gas with constant specific heats	Over the temperature range of interest, c_P does not change by more than 0.06%

The importance of each assumption is assessed in Chapter 7. In particular, Table 7.1 should be referred to when deciding the assumptions that must be refined for future work. The particular numerical assumptions, such as time-step size and discretization, are discussed in the next chapter, which discusses the numerical implementation of the physical models discussed above.

4. NUMERICAL APPROACH

This chapter describes the connections between the fluid model, the unit cell energy balance, and the other connected physical models such as the decay heat generation and RCCS heat removal over the course of the transient simulation. The specific time-steps are discussed for the fluid and solid unit cell models. Finally, since a cluster of processors are used to reduce the computational time, the specific Message Passing Interface algorithm is also discussed.

4.1 Solid Node Time Integration

The semi-implicit time integration scheme for the fluid method was discussed in Section 3.2. Different time-step sizes are used for the fluid calculations and the solid node calculations that are discussed in Section 4.2. The solid node (unit-cell) time integration scheme is discussed here in this section. This is because it is different than that used for the fluid calculations. This leads to the computation of different physical quantities at different intervals. The resolution of this computational mismatch is also discussed in this chapter.

A fully explicit time integration scheme was previously used for the steady state unit cell calculations without the incorporation of the transient fluid model. This led to small time-step sizes (0.01 to 0.001s) to ensure numerical stability. However, for a transient simulation with time-dependent heat generation, as is the case for the LOFC accidents that assume a reactor trip from full power at t = 0, the numerically stable time-step size changes over time and could lead to non-physical simulations late in the transient computation. Therefore, a more stable time integration scheme is implemented to ensure numerical stability and decrease the overall computational time.

The selected time integration technique for the unit cell energy balances is a Fourth-Order Runge-Kutta (RK4) scheme. The unit cell energy balance equation (see Eq. 3.2) has the explicit and implicit forms: $T_{n+1} = T_n + \Delta t \cdot f(t_n, T_n)$ and $T_{n+1} = T_n + \Delta t \cdot f(t_{n+1}, T_{n+1})$,

respectively, where n is the current time and $n+1$ is the new time. The RK4 method used here computes the new unit cell temperature using Eq. (4.1) through Eq. (4.5).

$$T_{n+1} = T_n + 1/6 \cdot \left[\Delta T_1 + 2 \cdot \Delta T_2 + 2 \cdot \Delta T_3 + \Delta T_4\right] \quad \text{Eq. (4.1)}$$

$$\Delta T_1 = \Delta t \cdot f\left(t_n, T_n\right) \quad \text{Eq. (4.2)}$$

$$\Delta T_2 = \Delta t \cdot f\left(t_n + \Delta t/2, T_n + \Delta T_1/2\right) \quad \text{Eq. (4.3)}$$

$$\Delta T_3 = \Delta t \cdot f\left(t_n + \Delta t/2, T_n + \Delta T_2/2\right) \quad \text{Eq. (4.4)}$$

$$\Delta T_4 = \Delta t \cdot f\left(t_n + \Delta t, T_n + \Delta T_4\right) \quad \text{Eq. (4.5)}$$

The solution method consists of solving a fully explicit estimate of the new temperature distribution, ΔT_1, within the reactor core. Then, new whole core temperature distributions are computed for each successive ΔT_i estimate. Thus for each time-step, a minimum of five whole core temperature distributions are computed using Eq. (4.1) through Eq. (4.5) and stored in memory to determine the RK4 new temperature distribution, T_{n+1}.

Since the RK4 method offers enhanced numerical stability over the explicit method, a longer time-step is used. The time-step size used for the unit-cell temperature calculations is ~0.5 s. This has been demonstrated for the MHTGR to be the longest stable time-step size over the entire LOFC simulations. One assumption used in the RK4 method described here is that convective heat transfer rates, which contribute to the functions, $f\left(...\right)$, for graphite unit cells that contain a coolant channel, are constant over the time-step. This is done to preserve heat addition to and heat removal from the helium and graphite respectively. This prevents having to re-compute or iterate between the solid unit cell computations and the fluid calculations over the time-step.

Ideally, longer time-step sizes could be used for the solid node calculations if the convective heat transfer rates were updated as the RK4 method progressed. This would require recalculation of the fluid equations using updated surface temperatures from the

solid node calculations. It should be noted that the solid node time-step size was selected to be stable without the need for iteration in concert with the fluid method, which would be computationally prohibitive for whole-core calculations. The next section describes the computational process in more detail.

4.2 Computational Process

There are principally two different time regimes operating in this method: (1) the unit-cell (solid graphite and fuel) heat conduction and energy balance time regime, and (2) the transient fluid time regime. Calculations for RCCS heat removal and heat generation rate also occur within one of the two regimes. Additionally, there are time-steps for data handling such as writing whole-core temperature distributions to output files. A general procedure illustrating the computational flow is shown in Figure 4.1.

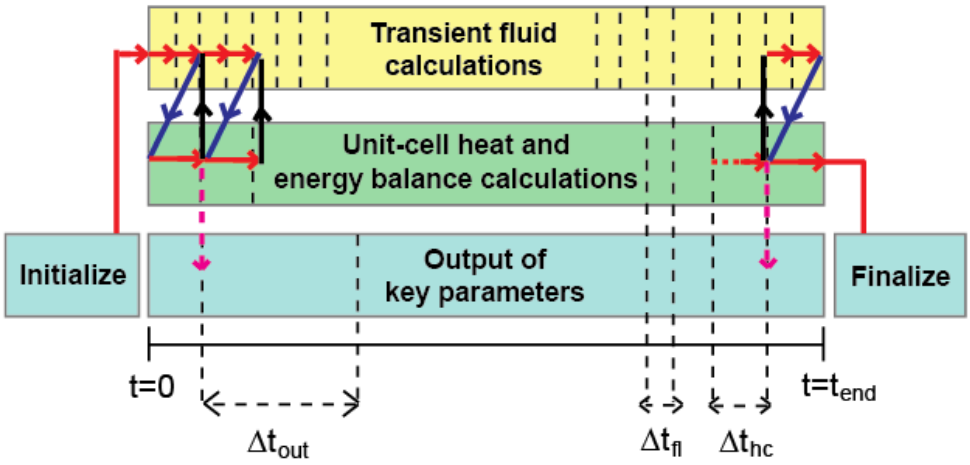

Figure 4.1 General Computational Flow Diagram

The two different time regimes, transient fluid calculations and the unit-cell heat and energy balance calculations can be observed in Figure 4.1. The red line represents the time difference calculations for each regime. The blue lines represent convective heat transfer estimates over the time-step for use in the unit-cell energy balance calculations. The black lines represent new graphite surface temperature estimates for the transient fluid

calculations. Finally, the dashed magenta lines represent the steps at which the output of the key thermal fluid parameters of interest is required.

For the first time-step, the basic process is:

(1) initialize all thermal fluid parameters including initial temperature and power distributions that are described in Section 3.2,

(2) solve the transient fluid equations for multiple fluid time-steps (Δt_{fl}) until the simulation time is greater than the unit-cell energy balance time-step ($t > t_0 + \Delta t_{hc}$),

(3) collect convective heat transfer rates over the fluid time-steps and transfer the time-averaged rates over Δt_{hc} to the unit-cell heat and energy calculations,

(4) compute the new whole-core graphite and fuel temperature distributions,

(5) transfer the new time fluid node graphite surface temperatures back to the transient fluid calculations,

(6) continue steps (2) through (5) until some output time-step (Δt_{out}) has passed and then write output files,

(7) continue steps (2) through (6) until the final simulation time (t_{end}) has passed and then finalize the simulation.

RCCS heat removal is estimated and applied to the fluid riser channel during step (2). Decay heat generation is estimated and applied to the fuel heat transfer calculations during step (4).

The time-step sizes are carefully chosen so that unit-cell energy balance calculations always occur at the end/beginning of a new fluid time-step. Similarly, the output time-steps are carefully chosen so that they coincide with the end/beginning of a new unit-cell energy balance time-step. Thus, the number of fluid time-steps per unit-cell step and the number of unit-cell time-steps per output time-step are always integer values.

If overlapping time-steps were used, incorrect or poorly estimated values could be reported. This also allows for a repeatable or fixed data communication structure between processors for high performance computing application.

4.3 High Performance Computing Implementation

To reduce the computational time associated with the numerical approach discussed in the previous section, domain decomposition is used to parallelize the unit-cell energy balance and fluid calculations. For the unit-cell calculations, the core is decomposed at the assembly block level. This is chosen because during each time-step, the heat conduction and energy balance calculations are primarily self-contained within each assembly. For the transient fluid calculations, each core coolant channel is treated independently (assuming no core cross-flow), which allows for a simple equal parsing of coolant channels between the available processors. The remaining fluid volumes such as the upper plenum, riser, and lower plenum are treated by a single processor.

Parallelization is achieved through the use of MPI and a Linux server cluster of anywhere between 8 and 128 processors. The optimal number of processors used for parallelization is dependent on a number of different factors including: the number of tasks that can be performed in parallel, and the communication cost for each processor added. For the unit-cell calculations, the number of parallel tasks is proportional to the number of active fuel assemblies (66 for the MHTGR). This is due to domain decomposition at the assembly level. This was chosen because only a limited amount of information about the eight neighboring assemblies (six radial and two axial) is needed. The reflector block assemblies do not contain any fuel or coolant channels and their temperature distribution can be computed much faster than for the active fuel assemblies. This implies that the optimal number of processors should be around 66 for the MHTGR. However, with communication cost, the actual optimal number of processors is around 16 for the MHTGR.

A diagram of the communication scheme for a single unit-cell energy balance time-step is shown in Figure 4.2. For illustration purposes, four processors are assumed. Node 0 is referred to as the "host node" since it computes the MPI parameters and controls the simulation process. Nodes 1 through 3 are referred to as "work nodes" since they are responsible for the bulk of the computations. The process numbers associated with Figure 4.2 are described in Table 4.1.

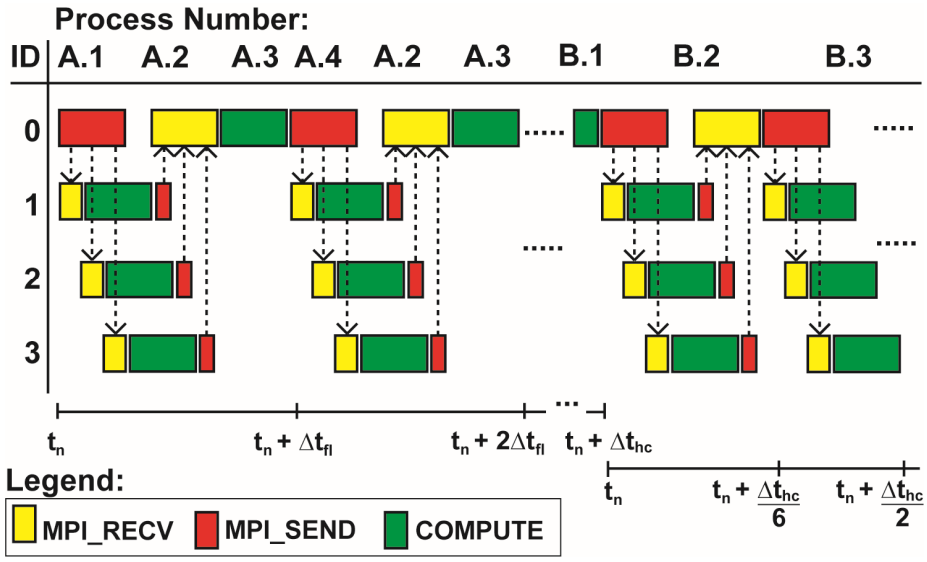

Figure 4.2 Example MPI Communication Scheme for Four Processors

Table 4.1. Process Number Descriptions for Figure 4.2

Process #	Description
A.1	For the current time, t_n, the "host" node sends the graphite surface temperatures for each fluid node to each "work" processor
A.2	Each "work" node computes the explicit and half step fluid quantities for each assigned fluid node and then sends this data back to the "host" node
A.3	The "host" proc. computes the hybrid pressure distribution, and the updated, new time-step quantities
A.4	The next fluid time-step is advanced and the new fluid values are passed back each "work" node
B.1	After all the fluid time-steps within a unit-cell energy balance time-step are complete, the average convective heat transfer rate over Δt_{hc} is passed to each "work" node
B.2	For each graphite and fuel compact unit-cell, ΔT_1 given in Eq. (4.2) is computed and passed back to the "host" node
B.3	For each graphite and fuel compact unit-cell, ΔT_2 given in Eq. (4.3) is computed and passed back to the "host" node
B.4 through B.5	Not shown on Figure 4.2. Similar to B.2 and B.3, ΔT_3 and ΔT_4 are computed and passed back to the "host" node. The "host" node then computes the new time-step temperature distribution from Eq. (4.1). The process then repeats with the next step A.1

The communication and computation boxes shown in Figure 4.2 are exaggerated to clearly show the communication processes. The chosen time-steps, unit-cell, and fluid node discretizations yield about equal computational demand between the fluid calculations ("A" steps) and the unit-cell energy balance calculations ("B" steps).

Typical calculation times for MHTGR P-LOFC simulations are around 146 hours for 16-24 processors. For the D-LOFC simulations, the total computational time is around 220 hours. For 18 processors, the computational speedup over a single processor is a factor of 7.8. This is due to the added communication time associated with distributed memory, parallel algorithms. Additional processors add communication work and ultimately, speedup decreases.

Normally, the computational time could be reduced by increasing the mesh size or lengthening the time-step size. In practice however, the chosen time-step size is fixed to be the largest numerically stable value, which is determined by a set of trail-and-error simulations. These preliminary stability simulations have clear outputs indicating whether the numerical results are stable or not. As soon as the method becomes unstable at some location within the core, the non-physical numerical results quickly propagate throughout the rest of the core and vessel. If the fluid model is not stable, it leads to errors in both the pressure drop and heat transfer coefficient calculations. This in turn leads to solid node energy balance errors. If the solid unit cell model is not stable, then non-physical new core temperatures are quickly observed. For all of the present results, the simulations are stable at all core locations over the entire transient.

For the present method, the mesh size for the prismatic HTGR and the associated fuel assemblies is also fixed, for the most part, due to the original choice of the unit cell to be containing either a single fuel pin or coolant channel. There is some choice regarding the axial height of the fluid channels and solid nodes. However, this also was chosen to reflect the physical height of the fuel assemblies and the height used in the neutronics calculations. Thus, the only substantial or practical option for reducing the computational time is by improving the high performance computing aspects.

Several improvements could be made to reduce the total computational demand. The first is to parallelize the A.3 step in Table 4.1. This would require implementing a linear equation solver parallel algorithm for the hybrid pressure distribution and then passing the hybrid pressure back to the “work” nodes. The “work” nodes could then compute all the new updated fluid variables and thermodynamic quantities and pass these data back to the “host” node. Another improvement would be to group core coolant channels by assemblies and keep the computed new fluid parameters local to that processor, which would then compute the unit-cell energy balance rates using those new convective heat transfer rates.

5. ACCIDENT SCENARIO RESULTS

This chapter presents the results for the two principal design basis accidents for the HTGR using the physical method and numerical approach outlined in the two previous chapters. The two principal design basis accidents include the pressurized loss-of-forced circulation (P-LOFC) and the depressurized loss-of-forced-circulation (D-LOFC) accidents. The primary difference between the two is that the P-LOFC is maintained around the normal operating pressure of 6.39 MPa and the D-LOFC accident is assumed to reach equilibrium with the containment around 1.0 MPa.

The initial conditions for each accident are the same, with the exception of the pressure condition. The initial temperature and power distributions are described in Section 3.2. The power distribution over the transient is constant; however, the magnitude drops as decay power decreases. The decay power decrease is assumed to be similar to the ANSI low enriched UO_2 decay heat curve for LWRs. The neutron energy spectrum is expected to be slightly different for the prismatic HTGR than for an LWR, leading to a slightly different fission product, and decay power magnitude. These neutronic effects are not expected to significantly alter the decay power over time for the MHTGR.

The decision to analyze LOFC accidents in this work over other accidents such as air or water ingress was based on the available research, which is discussed in more detail in Chapter 2. Additionally, the LOFC accidents are fundamental to all other accident categories. For example, air-ingress accidents progress in similar fashion to the D-LOFC, with the exception of possible graphite oxidation reactions. Similarly, water-ingress or other positive reactive insertion accidents follow the same D-LOFC progression until recriticality occurs which is typically much later in the accident, when core temperatures have cooled to some low temperature. The most limiting accidents are then dependent on the results of the P-LOFC and D-LOFC accidents.

It will be shown in the following sections that the RCCS plays a vital role for the LOFC accidents since it is the only system available to remove decay heat. It is assumed that for sufficiently elevated vessel temperatures, the RCCS is able to remove a certain amount of heat directly from the vessel according to the model outlined in Section 3.4. One important assumption to note is that below 230°C, the RCCS does not remove any heat from the vessel. This a conservative assumption but it should not be too conservative since the helium density at 230°C is only 25% lower than the density at 100°C and 1 MPa, which is the primary driving mechanism for natural recirculation. For a water-cooled RCCS, the minimum vessel wall temperature is expected to be just above 100°C for low heat removal rates.

It should also be noted that during normal operation, the flow direction is downward through the core. Helium enters the vessel through a lower elevation cross-duct. It then travels upward through a riser channel, down through the core into the lower plenum, then out of the vessel through the inner double tube cross-duct. During an LOFC accident, the PCU is assumed to isolate (a main shutoff valve closes on loss of power), and a lower plenum valve opens connecting the lower plenum to the riser channel. This lower plenum valve can either be electronically controlled, which would fail open on loss-of-power, or it could fail open due to the loss of pressure difference between the inlet helium and the outlet helium. During normal operation, the outlet helium will be about 30-40 kPa lower than the inlet helium. During an LOFC when natural circulation is occurring, the core helium pressure drop will be much less than this, around 1 kPa for a P-LOFC, and 0.16 kPa for a D-LOFC. This pressure drop is balanced by the gravitational head difference along the vessel wall and in the core. Since helium is a low-density gas, the temperature difference needed to produce this gravitational head difference could result in peak fuel temperatures being exceeded. Core temperature results for both LOFC cases are presented and discussed in this chapter.

It should be noted that the purpose of the LOFC results for the MHTGR-350 presented here is not to certify the safety of the MHTGR-350 for immediate licensing but rather to highlight the importance of accurate fuel assembly and whole core modeling. Several aspects of this method should be improved to further increase the accuracy of the calculations prior to submitting a proposed safety design basis to regulatory agencies. Future work and possible improvements to the method are discussed in Chapter 7. Discussions of the LOFC results follow.

5.1 P-LOFC Results

The P-LOFC simulation was terminated after 48 hours once both core and peak and average temperatures began to decrease over time. Core peak and average temperatures over time are plotted in Figure 5.1.

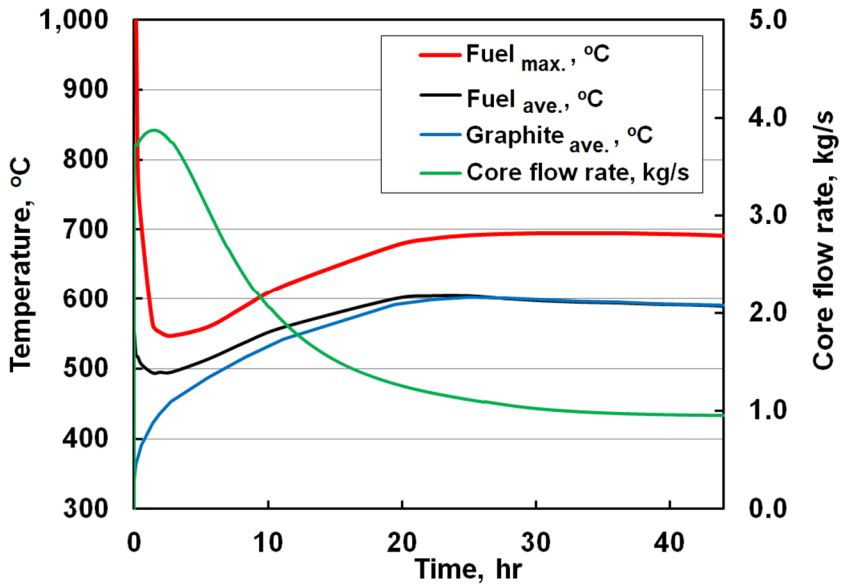

Figure 5.1 P-LOFC Core Peak and Average Temperatures

The transient can be separated into three separate phases: (1) initial cool-down, (2) core heat-up, and (3) safe shutdown phase. The initial cool-down occurs starting when the control rods insert at t = 0, which causes the core power to quickly decrease to a fraction of the normal operating power (< 5%). This in-turn causes the temperature gradient

between the local graphite and fuel compact to dramatically decrease. Temperature gradients within the fuel assemblies decrease accordingly. Additionally, during this phase, heat is redistributed from high temperature regions of the core to lower temperature regions. The initial cool-down phase lasts approximately from t = 0 to t = 1 hr. The P-LOFC fuel temperature distribution at the end of the initial cool-down phase is shown in Figure 5.2.

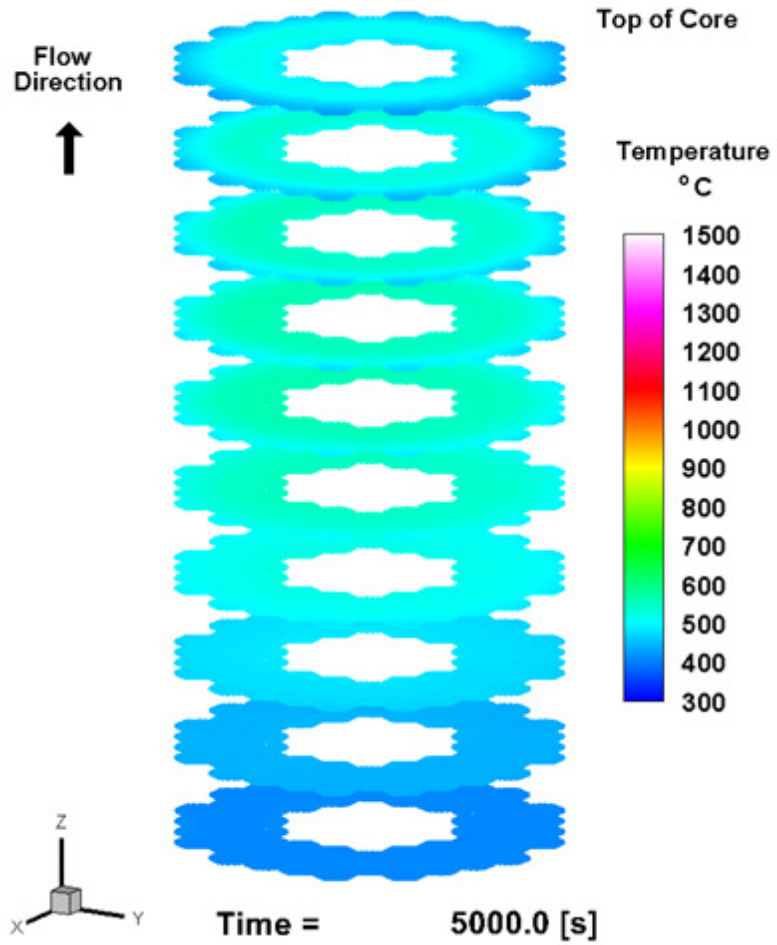

Figure 5.2 P-LOFC Fuel Temperature Distribution at the Beginning of the Core Heat-up Phase

The flow direction arrow in Figure 5.2 is now opposite to that at steady state. During an LOFC transient, the flow reverses direction due to buoyancy forces. The core heats up the helium causing it to rise. The vessel wall then cools the helium causing it to fall in the direction of the natural circulation flow. The peak fuel temperature at this time is around 550°C.

Once a new thermal equilibrium is reached for the new power level, the core heat-up phase begins. This is due an energy mismatch between core heat removal and heat generation. Figure 5.3 shows the energy balance over time for the P-LOFC.

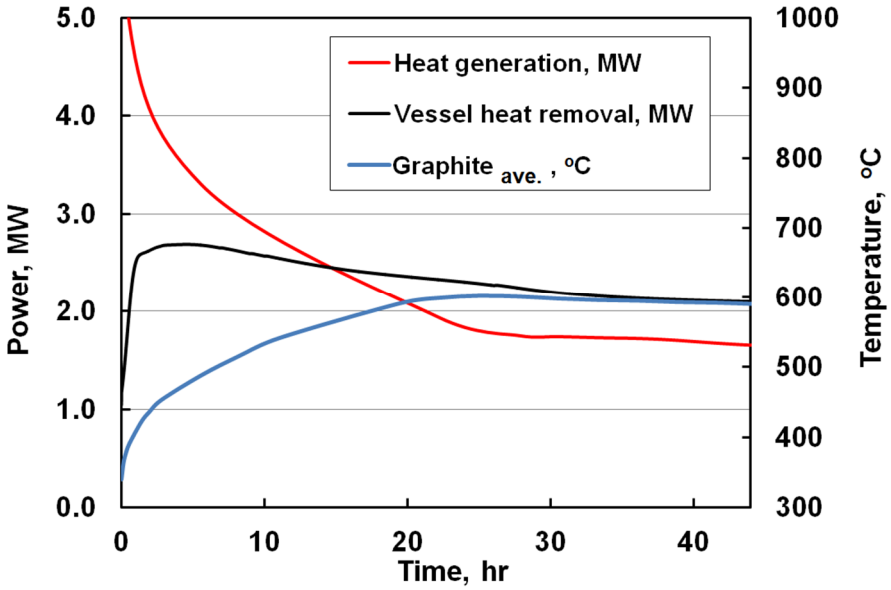

Figure 5.3 P-LOFC Transient Energy Balance

The core heat-up phase for the P-LOFC accident lasts approximately from t = 1 hr to t = 20 hrs. This is observed in Figure 5.3 when heat generation rate is greater than the vessel heat removal rate. The vessel heat removal rate surpasses the heat generation rate at about t = 16 hrs. However, even when the vessel heat removal rate is greater than the heat generation rate, average core temperatures still rise slightly until t = 20 hrs. This lag is primarily associated to stored heat removal in the helium and the vessel wall.

Additionally, peak fuel temperatures do not reach a maximum until slightly later, *i.e.*, at around t = 30 hrs. This is due to different heat generation rates at different core

locations. This time-dependent, spatially dependent phenomenon does not contribute significantly to peak fuel temperature rise as the peak fuel temperature at t = 30 hrs is only 12°C hotter than at t = 20 hrs. The fuel temperature distribution at the end of the core heat-up phase is shown in Figure 5.4.

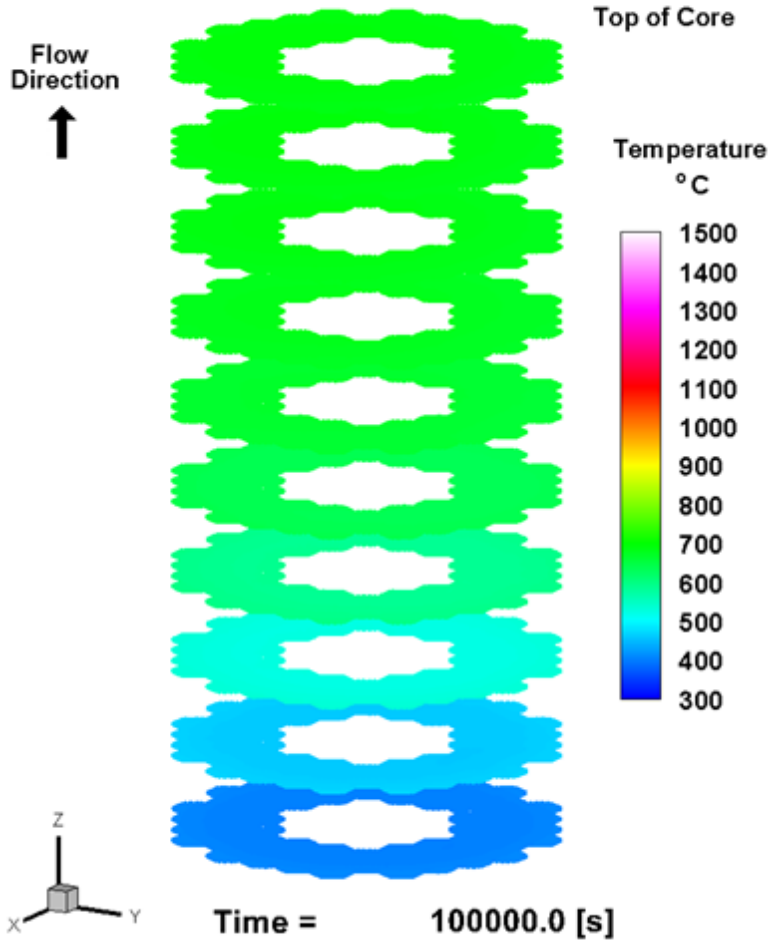

Figure 5.4 P-LOFC Fuel Temperature Distribution at the End of the Core Heat-up Phase

The fuel temperature is peaked toward the top due to the coolant entering the bottom of the core and exiting at the top of the core. This is in contrast to normal operation for which the opposite trend is observed. It is at this time the core can begin to cool-down because sufficient recirculation has been established. The peak core coolant flow rate

during the P-LOFC is 4 kg/s. This is in comparison to the normal operation flow rate of 151 kg/s. Once the core begins to cool-down from the distribution shown in Figure 5.4, the core mass flow rate decreases due to decreasing fluid temperature difference between the upper and lower plenums. This leads into the safe shut-down phase since peak fuel temperatures have not exceeded their design failure limit (1600°C) and will only decrease beyond this time due to decreasing heat generation rate. The final fuel temperature distribution for the P-LOFC accident is shown in Figure 5.5.

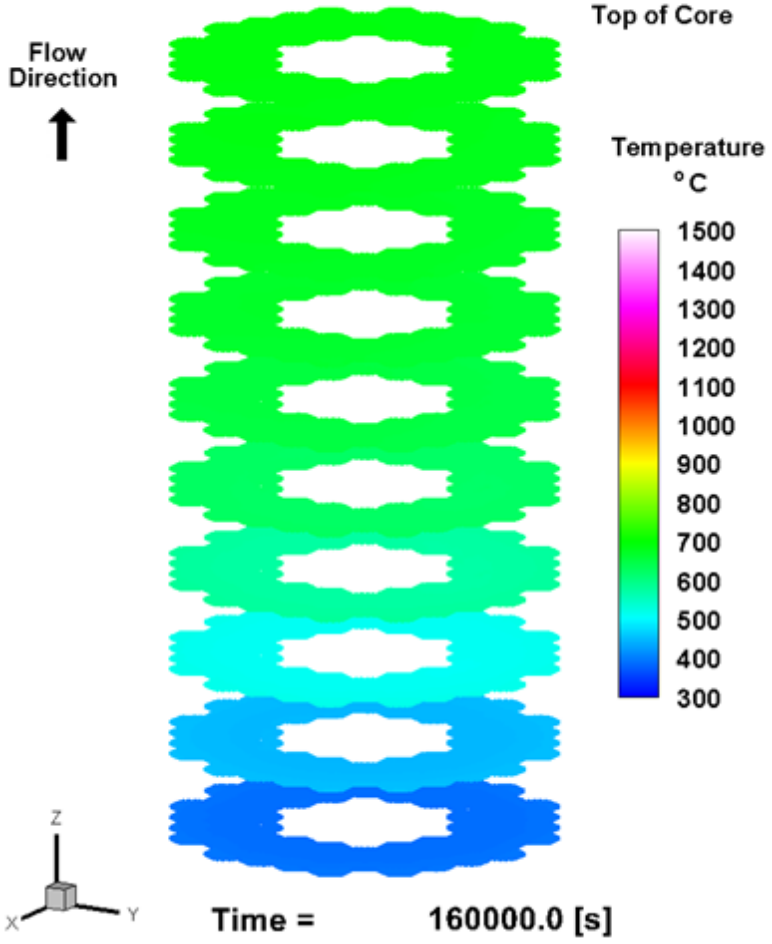

Figure 5.5 P-LOFC Fuel Temperature Distribution during the Safe Shut-down Phase

Although the temperature distribution shown in Figure 5.5 does not appear to be dramatically different than the distribution shown in Figure 5.4, it is clear that the lowest elevation axial slice is cooler than the lowest axial slice in Figure 5.4. Similarly, the highest elevation axial slice is also slightly cooler. This indicates that the core is in-fact cooling down to a safe and stable configuration without the need for any operator action or external electrical power source.

5.2 D-LOFC Results

The D-LOFC simulation was terminated after 60 hours once peak and average core temperatures begin to decrease over time. Core peak and average temperatures over time are plotted in Figure 5.6.

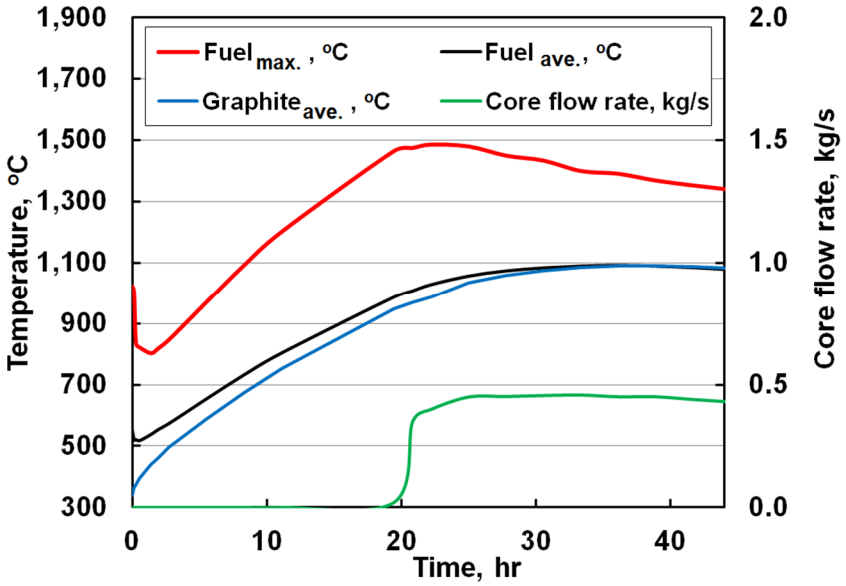

Figure 5.6 D-LOFC Core Peak and Average Temperatures

There is an immediate difference between the D-LOFC simulation and P-LOFC simulation results presented in Figure 5.1. The temperatures for the D-LOFC are significantly higher than for the P-LOFC. However, there are still three distinct phases similar to the case for the P-LOFC. These phases are: the (1) initial cool-down, (2) core heat-up, and (3) safe shutdown phase.

Similar to the P-LOFC, the initial cool down extends from t = 0 to about t = 0.75 hr. This occurs because the insertion of the control rods drops the normal operation power of 350 MW to only a few megawatts over the course of a few minutes. It is slightly shorter for the D-LOFC than for the P-LOFC because the helium density is significantly lower, which prevents helium recirculation that aids in the redistribution of heat from the lower portion of the core to the upper, cooler regions. Since this redistribution does not occur, the heat-up phase begins earlier. The fuel temperature distribution at the end of the initial cool-down phase is shown in Figure 5.7.

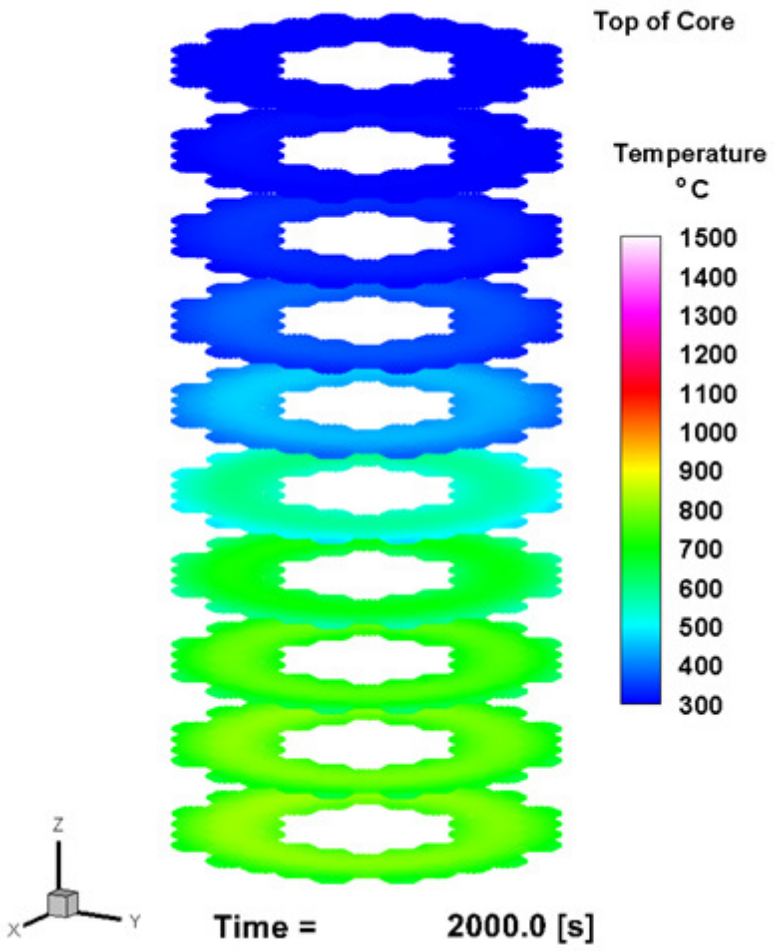

Figure 5.7 D-LOFC Fuel Temperature Distribution at the Beginning of the Core Heat-up Phase

The initial cool-down fuel temperature distribution shown in Figure 5.7 is only slightly cooler than the initial temperature distribution shown in Figure 3.5. This is because the core power decreases significantly and some heat is redistributed into the inner and outer reflector blocks. During this phase, there is no helium recirculation. Figure 5.8 shows the overall D-LOFC energy balance.

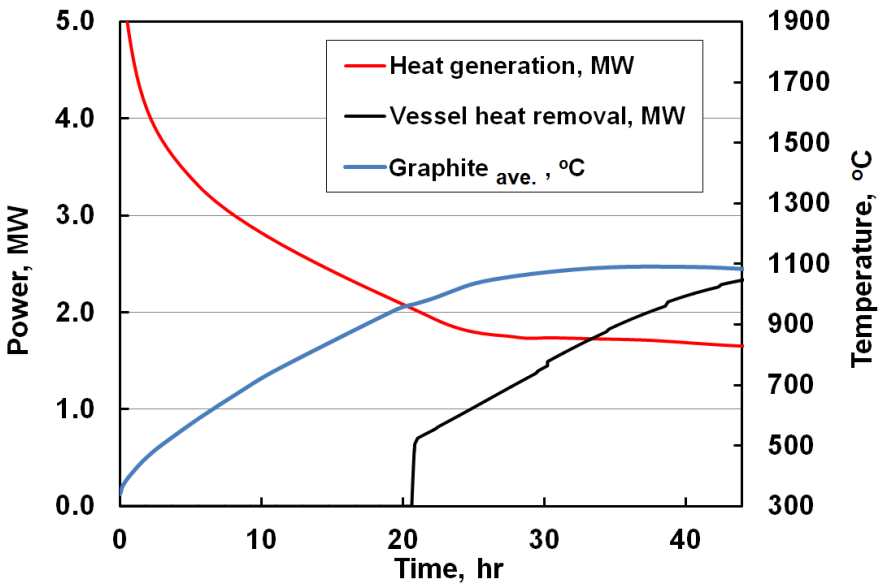

Figure 5.8 D-LOFC Transient Energy Balance

The core heat-up phase for the D-LOFC extends much longer than for the P-LOFC case. This is expected since recirculation and heat removal are much lower; therefore, more time is needed to reduce the heat generation. At about 20 hours, there is nearly zero vessel heat removal. This is due to no core recirculation during this time preventing the core high temperature helium from contacting the vessel wall. Stagnant, low temperature helium rests between the core and the vessel wall preventing vessel heat removal. It is only after the core heats up significantly that the helium density gradient is sufficient to drive some small core flow allowing for the vessel wall to heat up.

The core heat-up phase lasts from about t = 0.75 hrs to about t = 33 hrs. This is observed in Figure 5.8 when vessel heat removal becomes larger than heat generation. For the P-LOFC case, the core heat-up phase is defined as the time from when the core average temperature is at a minimum post-SCRAM to the time for which the fuel temperature reaches a maximum. If a similar definition is used for the D-LOFC case, the fuel temperature reaches a maximum around t = 21 hrs. However, the average temperatures are still increasing at this point and do not begin to drop until t = 33 hrs, when the heat removal becomes greater than the heat generation.

This leads to a regulatory safety question of which parameter to use as the definition for core heat-up and when safe shut-down is reached. For LWRs, the classification of safe shut-down or "safe-and-stable" configuration has certain reactor operator implications, U.S. Nuclear Regulatory Commision (2009). It is advantageous from a reactor operator perspective to have the core in a safe shut-down configuration as soon as possible. Taking the most conservative approach for LOFC accidents, safe shut-down is defined as the time when both the peak and average fuel temperatures begin to decrease.

On the one hand, if peak fuel temperatures begin to decrease and fuel failure limits have not been exceeded, it is very unlikely that peak fuel temperatures could exceed fuel failure limits later in the accident. However, if average temperatures are still increasing, it may not be immediately clear if the RCCS would be able to remove decay heat indefinitely. Therefore, it is the best safety decision to define safe shut-down as the time when both peak and average fuel temperatures are decreasing.

A more important question may be, "For the D-LOFC, why does the peak fuel temperature decrease before the average temperature?" This is in contrast to the P-LOFC accident for which the peak fuel temperature was not observed to decrease until a few hours after the average temperatures began to decrease. This was due to a thermal lag associated with the cooling of the graphite along the coolant channels, which was not observed in the fuel until later. This question is answered upon investigation of the channel mass flow rates between the P- and D-LOFC accidents.

For the P-LOFC case, the channel mass flow rates are nearly uniform with a total core flow rate between 2 – 4 kg/s. For the D-LOFC accident, channel mass flow rates are negligible for times less than t = 20 hrs due to the lack of sufficient density gradient for natural circulation. This is ultimately due to the reduced vessel pressure associated with the primary system break, which does not occur for the P-LOFC case. After this time, a very small recirculation flow begins to develop. The total core flow rate after t = 20 hrs is between 0.40 – 0.45 kg/s. Like the P-LOFC accident, the flow is in the upward direction

through the core. Peak fuel temperatures are initially located at the base of the core. As the lower portion of the core cools, the upper portions begin to heat-up and a reverse axial temperature profile develops. As this axial redistribution of heat due to late recirculation flow forms, the peak fuel temperature is fluctuating based on the core location. The overall trend of the peak fuel temperature is decreasing during this time primarily due to the lower core power density in the upper portions of the core.

Another important question is: "Why is there negligible vessel heat removal prior to t=20 hrs?" This is principally due to two factors: (1) thermal modeling within the riser channel and between the core barrel is limited to convective heat transfer (due to recirculation if any), and (2) there is no recirculation flow prior to t = 20 hrs. The first factor is a conservative assumption since there will be some heat conduction across the riser channel as well as radiation heat transfer. Without knowing the specific vessel geometry beyond the core region, it is unclear how much conduction or radiation occurs within this region. Without coolant flow through the riser channel, the vessel wall stays near its initial temperature and thus no heat is removed by the RCCS. This is an important area of improvement for future HTGR LOFC accident modeling as there will be some additional heat removed. Figure 5.9 shows the fuel temperature distribution at the peak time (t = 22 hrs).

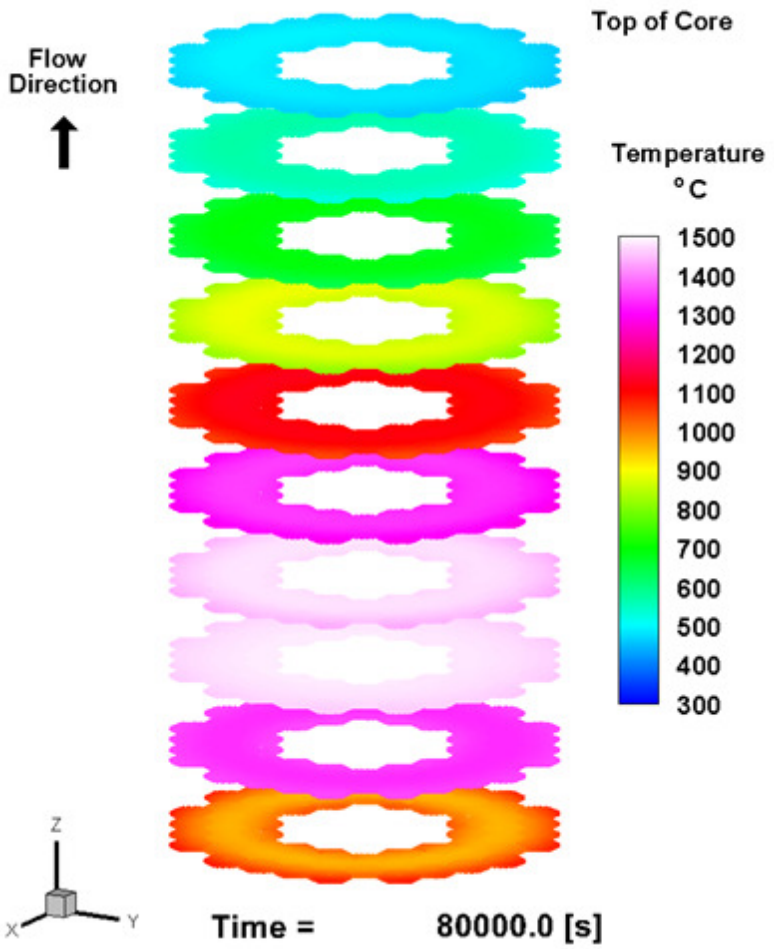

Figure 5.9 D-LOFC Fuel Temperature Distribution at the Time when Fuel Temperature Reaches a Maximum

In Figure 5.9, peak fuel temperatures are observed in the third and fourth axial slice from the bottom of the core. This corresponds to the same location as the peak power density as shown in Figure 3.4. Therefore, it can be concluded that the initial power distribution does play a role during the LOFC accident after reactor SCRAM has occurred. After this time, core recirculation, although very small (~0.4 kg/s), begins to slowly carry heat away from the lower portion of the core to the upper portions. This is physically observed in the fuel as a peak temperature wave traveling upward through the core. This

wave gradually decreases in magnitude since the power density is lower in the upper regions of the core.

Once the peak fuel temperatures reach the top of the vessel and vessel heat removal rate outpaces heat generation, the safe shut-down or cooldown phase begins. This occurs at approximately t = 33 hrs. The final fuel temperature during the safe shut-down phase is shown in Figure 5.10.

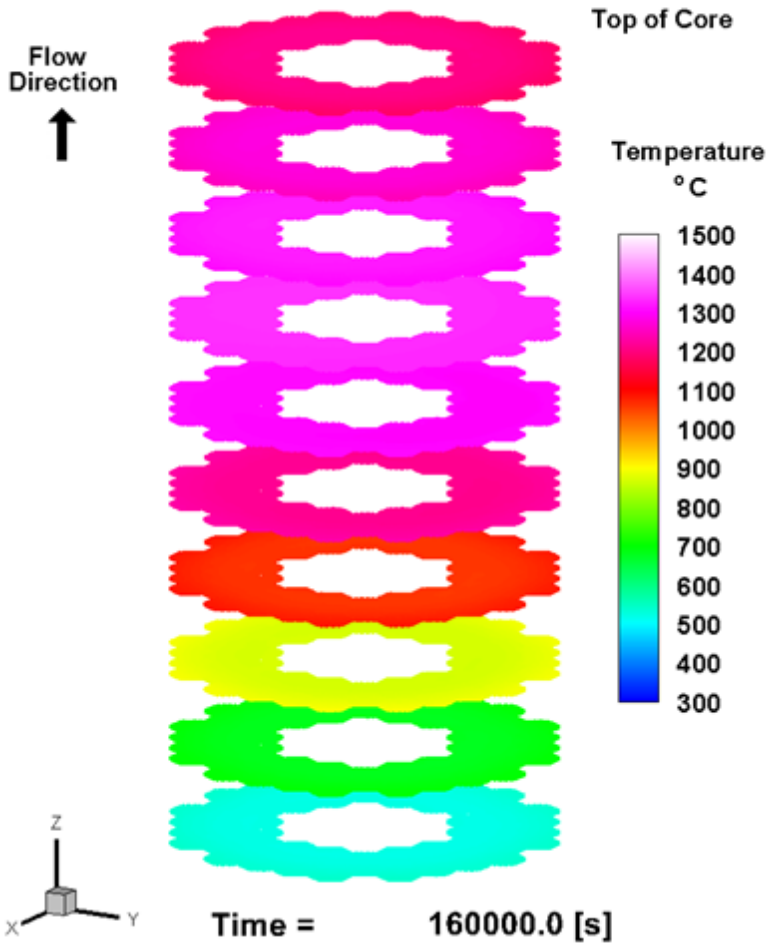

Figure 5.10 D-LOFC Fuel Temperature Distribution during the Safe Shut-down Phase

From Figure 5.10, the bottom of the core is much cooler than in Figure 5.9. This is due to cooler helium entering the base of the core after being cooled by the vessel wall,

which is cooled by the RCCS. For later times, heat generation will continue to decrease, and RCCS heat removal remains fairly constant at around 2.1 MW. This leads to decreasing fuel and graphite temperatures beyond t = 33 hrs.

While fuel failure is not predicted for either the P-LOFC or D-LOFC case, fuel temperatures could exceed 1600°C for some of the more extreme D-LOFC cases with containment failure. This would lead to a loss of the 1 MPa back-pressure assumed in these analyses. However, several improvements could be made to increase the safety margin for HTGRs. Since natural circulation is dependent on the height between the cooler helium along the vessel wall and the hot helium in the core region, it would be beneficial to increase the vessel height above the core region. Currently, there is an upper reflector (0.79 m) above the core, as well as the upper plenum. Adding another reflector (total 1.58 m) to the top of the core would increase the graphite mass available to absorb heat during an accident, as well as add natural circulation height.

However, it is unlikely that any safety improvement could be made without some economic trade-off. Considering that the economic cost of a nuclear plant is closely tied to the cost of the vessel diameter, it would ultimately be cheaper to increase the vessel height than to add to the core radial dimensions (*i.e.*, have a lower power density). This optimization and economic trade-off should be considered for future HTGR design efforts with input from design basis, LOFC analyses.

6. RELAP5-3D COMPARISON RESULTS

The previous chapter presented results using the transient HTGR thermal-fluid analysis method developed in the present study to compute core temperature distributions for the P-LOFC and D-LOFC accident simulations. This chapter presents results for the same reactor design and accident scenarios using the fuel models available within the RELAP5-3D computer code. RELAP is used extensively in the LWR nuclear industry for its high reliability, accuracy, and availability. RELAP has also been used for some select HTGR studies such as the NGNP point design (MacDonald 2003). The typical fuel models used in RELAP are investigated for HTGRs in this Chapter.

The purpose of performing these HTGR RELAP simulations is primarily to highlight the differences associated with the fuel models available in RELAP to those previously described using the approach developed here in Chapter 3. These differences lead to critically different transient results for the P- and D-LOFC accidents. The RELAP simulation results presented here demonstrate the need for a transient method capable of whole-core level modeling with pin-level resolution and an accurate power distribution.

The same vessel geometry and initial fluid conditions assumed in the previous Chapters are also used for the RELAP analyses presented here. The next section discusses the discretization of the core and fuel assemblies.

6.1 RELAP MHTGR Fuel Model

Two principal fuel models are investigated. The first is a typical LWR fuel model that considers the fuel, cladding and surrounding moderator to be concentric cylinders with a convective heat transfer outer radius boundary condition and a symmetric temperature boundary condition at r = 0. For non-concentric cylinder fuel geometry, this model is often called an “Equivalent Cylindrical Model”, Todreas and Kazimi (2001), because the fuel and other surrounding materials are artificially modeled as cylinders with their respective

radii computed from a mass balance between the physical and model geometry. For the HTGR, the order of the fuel, graphite and helium as equivalent cylinders is not immediately intuitive. A representation of this model for the HTGR is shown in Figure 6.1.

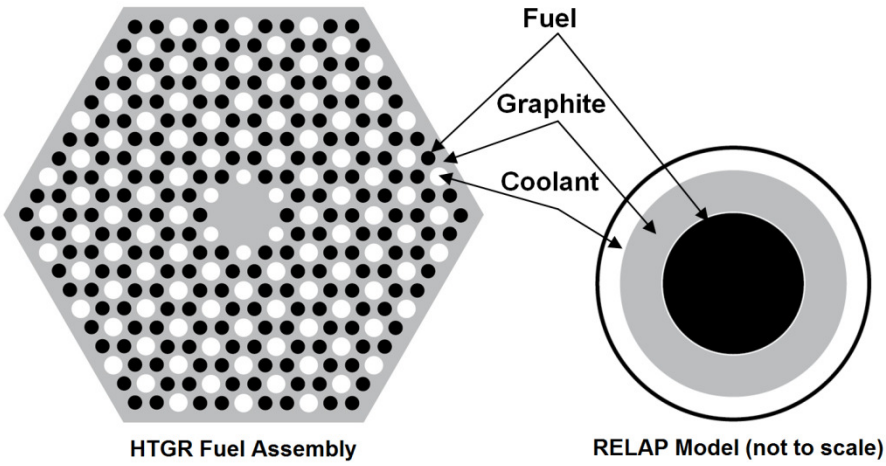

Figure 6.1 Equivalent Cylinder Fuel RELAP Model

There is also a small gap (helium) space between the fuel compact and graphite in both the HTGR fuel assembly and the RELAP Model. The coolant in the RELAP model is not physically contained in the fuel heat structure (RELAP fuel model) but is in a defined hydrodynamic volume connected to the heat structure. The fuel diameter in the RELAP model has been greatly exaggerated for illustration purposes in Figure 6.1. The mass of both the fuel and graphite have been conserved between the HTGR fuel assembly and the RELAP model.

There are several obvious drawbacks to this model. The first is that because the radii are determined from conserving the mass, the thermal resistance of the graphite between the fuel and coolant may be significantly overestimated due to all of the graphite in the HTGR fuel assembly being placed between the fuel and coolant. This enlarged resistance also causes the transient response in the fuel due to changing coolant conditions to be delayed or slowed. The second drawback is that only a single fuel compact is modeled for an entire assembly. There are approximately 210 fuel compacts per assembly, each with

their own power density. To ensure that the same core power is used for the RELAP model and the assembly, this leads to only a fuel compact with an average power density being modeled. This can be slightly mitigated by modeling several assemblies as equivalent cylinders with each fuel cylinder having a different assembly power. However, this still limits any intra-assembly power peaking, which leads to lower predicted peak fuel temperatures. Another drawback is that this model does not allow for bypass gap heat removal from the assembly. Only a single hydrodynamic volume can be coupled to the equivalent cylinder model. From previous steady state calculations, it is expected that bypass gap heat removal could account for as much as 10% of the total core heat removal. Without this heat removal, helium temperatures could be slightly overestimated, leading to an overestimation of the graphite temperature and subsequent fuel temperature. If the bypass gaps are neglected all together, core flow rates will be higher than predicted, leading to an underestimation of graphite temperature.

Due to these complications associated with the equivalent cylinder model for HTGR fuel, a new fuel model that alleviates some of these concerns was constructed for the HTGR. The new model uses 2-D slabs (x-z geometry) to represent the graphite, fuel, and gap space. This also allows for bypass flow to contribute to core heat removal. The hydrodynamic volumes can remain in their particular geometry: circular tubes for assembly coolant channels, and flat bypass flow channels. This new model allows for some intra-assembly power peaking to be simulated. Although not every fuel compact can be modeled, which is possible with the method developed in this study, this new model can compute up to five fuel compacts per assembly. This new fuel model is represented schematically in Figure 6.2.

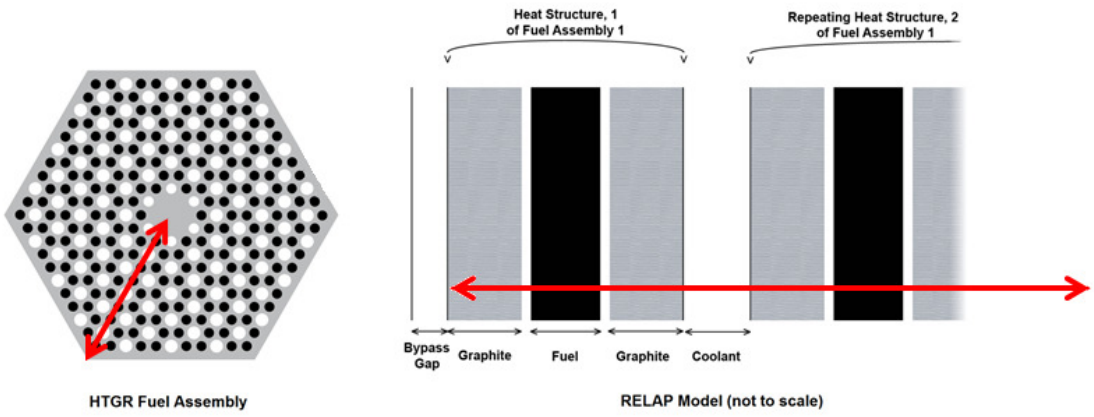

Figure 6.2 Advanced Slab Fuel RELAP Model

Two heat structures are shown in Figure 6.2. However, along the fuel assembly diagonal shown in red, there are four heat structures containing a total of seven fuel compacts and space for four hydrodynamic volumes. Each heat structure is bounded by two hydrodynamic volumes except for the inner surface of the inner most slab. This surface is an insulated or symmetric boundary condition. When all four of these heat structures are lined up, the resulting fuel assembly model looks similar to that shown in Figure 6.3.

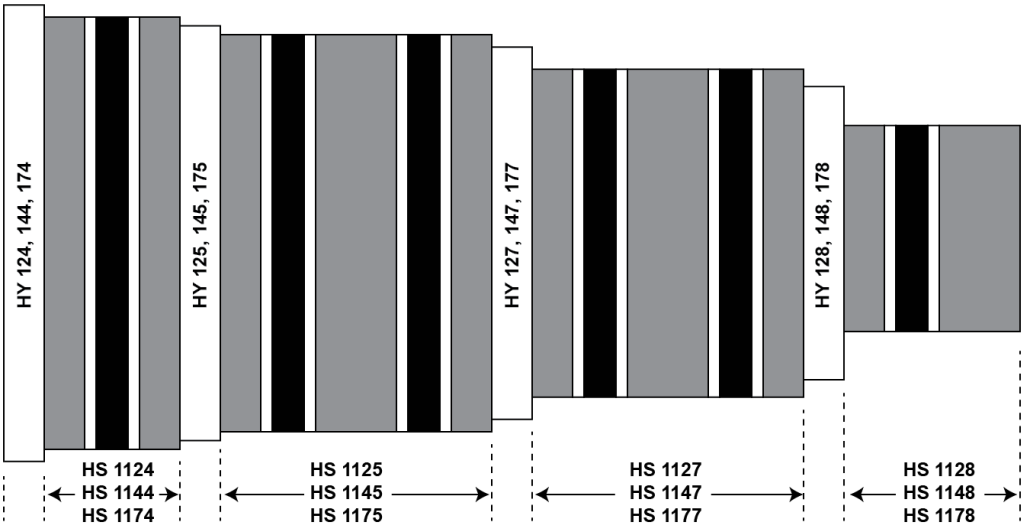

Figure 6.3 Top-down View of the Advanced Slab Fuel RELAP Model

This fuel model is used to represent three different assemblies within the core. Each fuel assembly is for a different active fuel assembly ring around the core. The three heat structure (HS) numbers and hydrodynamic (HY) numbers are for each of these fuel assemblies. Additionally, the fuel heat structures and core coolant hydrodynamic volumes are axially divided into ten segments. Within each assembly heat structure, the fuel and graphite volumes are further discretized into three to seven different sub-slabs. This leads to a total of 210 fuel compacts modeled with 630 unique fuel temperature points.

Unlike the equivalent cylinder model, which only has one flexible dimension (radius), the slab fuel model has two (width and length). The height for each model is fixed at the active core height of the MHTGR, which is 7.93 m. Figure 6.3 shows the width of each fuel or graphite slab to be the same, but the length of each heat structure decreases as the slabs move inward. The slab length is fixed to conserve fuel and graphite mass between the physical assembly and the model. This allows for the slab width to be set relative to its actual dimensions within the hexagonal assembly block. For example, the cylindrical fuel compact diameter is 12.45 mm. The equivalent slab width for a similar thermal resistance is 5.9 mm. The graphite slab width used is an approximate average distance between the fuel and coolant channel.

For the inner and outer core reflector blocks, these are approximated as similar slabs to the fuel model but only contain one graphite volume. Bypass flow hydrodynamic volumes connect to each reflector slab face.

One drawback common to both the advanced slab fuel model and the equivalent cylinder mode is that heat transfer between assembly blocks is limited. No heat conduction can occur between the inner assembly ring heat structures (HS 1124) and the outer ones (HS 1144 and HS 1174). On a similar note, no heat conduction can occur into the inner and outer reflector blocks. This large mass of graphite is needed during an LOFC to absorb heat early in the accident. Heat transfer into these regions can only occur due to helium flow

and mixing in the lower and upper plenum vessel regions. The specific MHTGR fluid nodalization is discussed in the next section.

Finally, the power distribution assumed is the same as what is used for the LOFC analyses presented in the previous chapter (see Figure 3.4). Since less fuel compacts are modeled in RELAP, some pin-power averaging is required to maintain a constant power level. The averaging procedure is as follows: (1) compute the total power for each fuel ring and axial location from Figure 3.4, (2) compute the fuel mass fraction for each fuel ring and axial location, (3) within each fuel ring and axial location, compute the fuel mass fraction for each heat structure (e.g., for the inner-most fuel ring, 26% of the fuel is in HS 1124, 43% in 1125, 25% in 1127 and 6% in 1128), (4) apply these heat structure specific fractions to the total power for that particular fuel ring and axial location, and finally (5) verify that the total core power sums to the design power (*i.e.*, 350 MW). See Appendix B for the specific power factors used for each heat structure.

6.2 Fluid Nodalization

A diagram of the fluid nodalization used for the MHTGR LOFC simulations is shown in Figure 6.4.

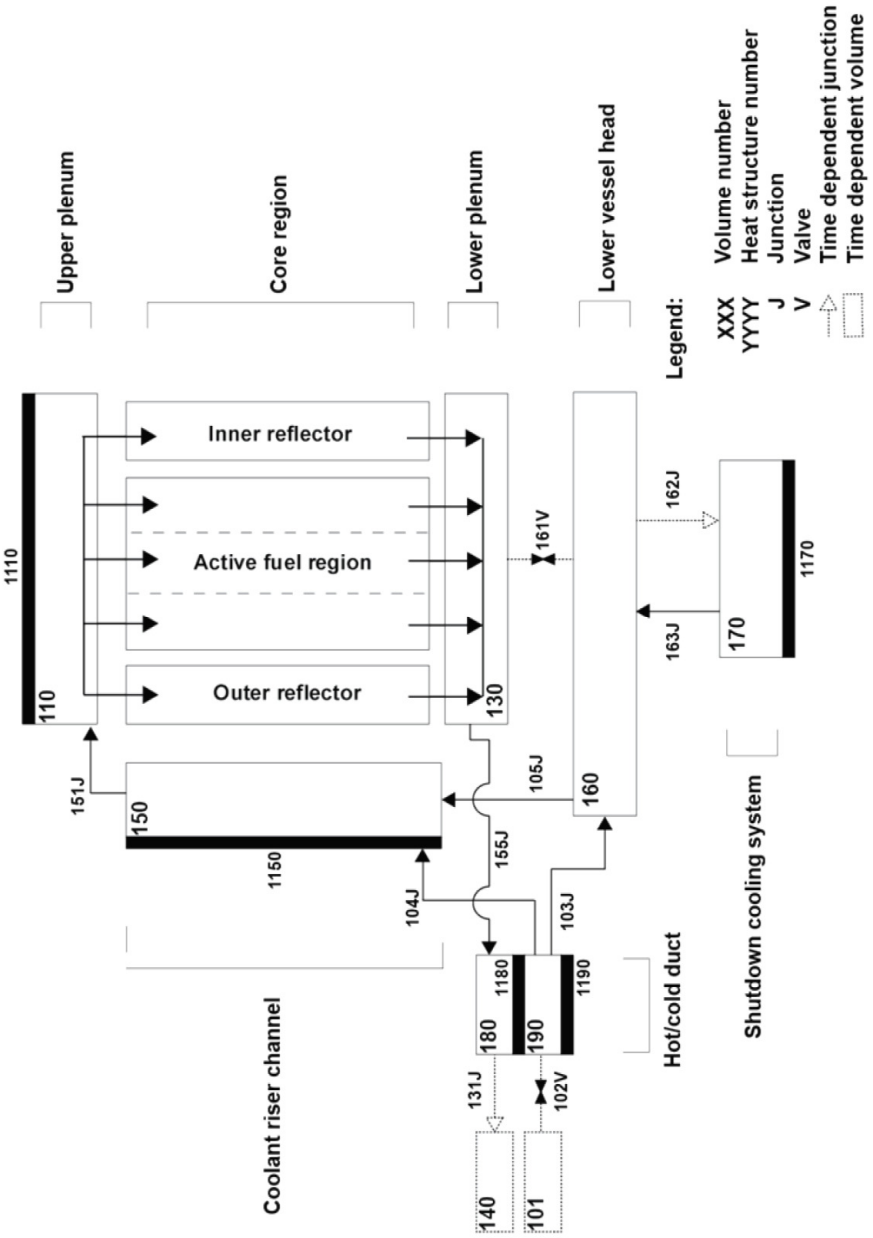

Figure 6.4 RELAP Nodalization for the MHTGR-350

The core region shown in Figure 6.4 consists of the fuel and graphite heat structures described in the previous section. It also contains the appropriate hydrodynamic volumes linked to those heat structures. For each hydrodynamic volume, there is an adjoining inlet and outlet junction. Each hydrodynamic volume within the core also consists of 10 different axial nodes to match the axial discretization of the heat structures.

With the exception of the core region and coolant riser channels, all other fluid volumes are classified as “single volumes” within RELAP. The core region and the coolant riser channels are “pipe volumes”. The coolant riser channel is also discretized into 10 axial segments to improve the RCCS heat removal calculations.

Heat removal from the vessel wall to the RCCS is modeled as a convective boundary condition on the outer vessel wall heat structure (HS 1150 in Figure 6.4). The convective heat transfer coefficient is supplied by a look-up table for specific vessel wall temperatures. The specific value for this heat transfer coefficient is identical to the RCCS performance curve shown in Figure 3.9.

Fluid volumes 101 and 140 in Figure 6.4 represent large boundary volumes not critical to the transient simulation. These volumes, along with the time-dependent junction and valve 131 and 102 respectively, control whether normal operating (steady state) boundary conditions exist or if a LOFC occurs. LOFC is only set to occur once a steady state temperature distribution within the core is formed. At this point, the mass flow rate through these junctions is set to zero for the P-LOFC case, or set to a specific down-stream pressure for the D-LOFC. Additionally, the junction connecting the lower plenum and the riser channels (131 in Figure 6.4) is normally closed but opens once the LOFC occurs.

Although the Shut-down Cooling System (SCS) is present in the developed RELAP model, it is not used and/or is assumed to have failed for the LOFC accidents.

Material properties for steel, graphite, and fuel-compact are supplied by user tables and are the same for those used in the method presented in the previous chapter. A complete listing of the material property values can be found in Appendix A.

6.3 RELAP P-LOFC Simulation Results

The basic approach for both the P-LOFC and D-LOFC simulations is to initialize the fuel and core materials to the inlet helium temperature (259^{o}C), and let the core approach some steady state temperature distribution at full power and core flow. Steady

state is reached 20,000 s into the simulation. The steady state fuel temperature distribution is shown in Figure 6.5.

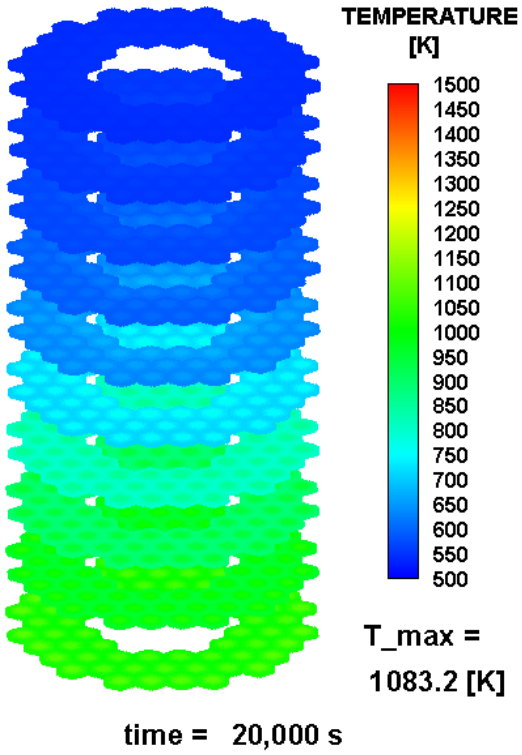

Figure 6.5 RELAP Steady State Fuel Temperature Distribution

Since RELAP cannot model every fuel compact, power averaging leads to under predicted steady state fuel temperatures compared to the temperature profile in Figure 3.5. The peak steady state fuel temperature here is around 810°C compared to the results presented earlier, which estimated the peak steady state fuel temperature to be near 950°C.

After 20,000 s, the LOFC is initiated by reducing core powers according to the decay heat curve, isolating the vessel from the power conversion system, and opening the lower plenum recirculation valve. Similar to Figure 5.3, the transient energy balance for the RELAP P-LOFC simulation is shown in Figure 6.6.

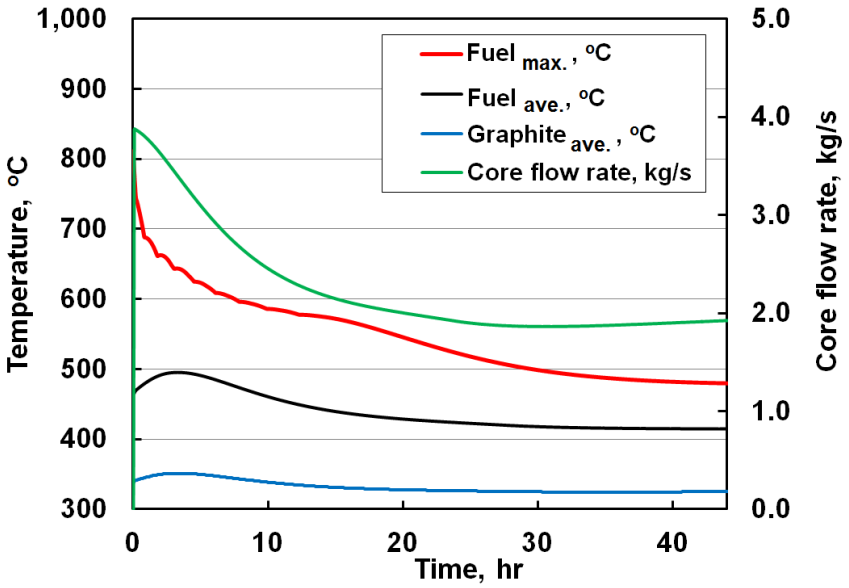

Figure 6.6 RELAP P-LOFC Transient Energy Balance

The key difference in Figure 6.6 compared to the P-LOFC results presented earlier in Figure 5.3, is that vessel heat removal by the RCCS is stronger. This is due to higher vessel surface temperatures, which are caused by a slightly higher estimated natural recirculation flow rate. This occurs due to two key factors: (1) the friction factor values in RELAP are based on smooth tubes, and (2) the elevation difference is slightly larger in the RELAP model due to the inclusion of the lower elevation SCS volume. While the SCS is not assumed to be operational, helium flow still occurs through this volume as no valves or junctions exist to limit the flow. These factors both reduce the pressure drop due to friction and increase the gravitational fluid flow potential. It is clear that for future LOFC calculations, additional care must be given to the specific correlation choice for each individual volume and how/which volumes are selected to be included in the vessel model.

Because of the increased RCCS heat removal, peak and average fuel temperatures are lower. These temperatures are plotted in Figure 6.7.

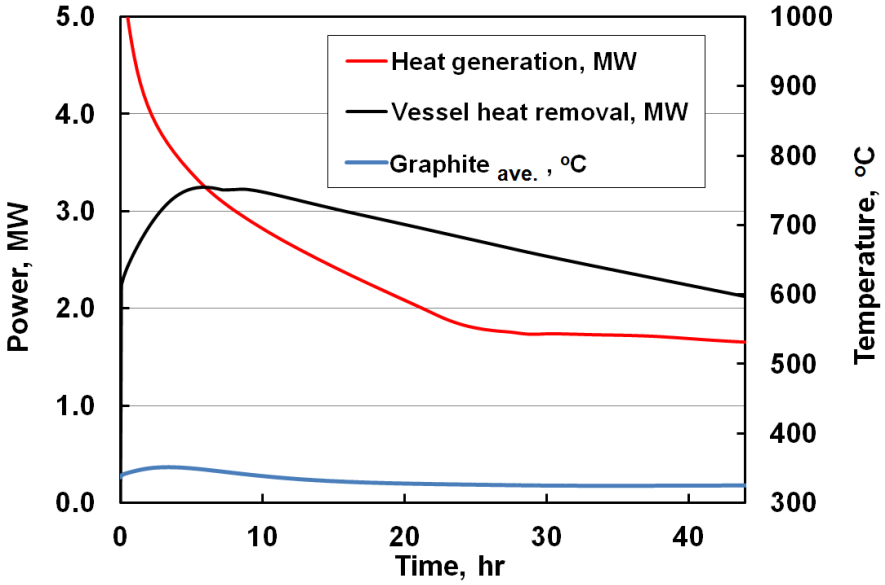

Figure 6.7 RELAP P-LOFC Core Peak and Average Temperatures

As shown in Figure 6.7, the heat-up phase is much shorter (between 5 – 6 hours) compared to earlier estimates (16 – 20 hours). Figure 6.8 shows the 3-D temperature distribution at the end of the core heat-up phase.

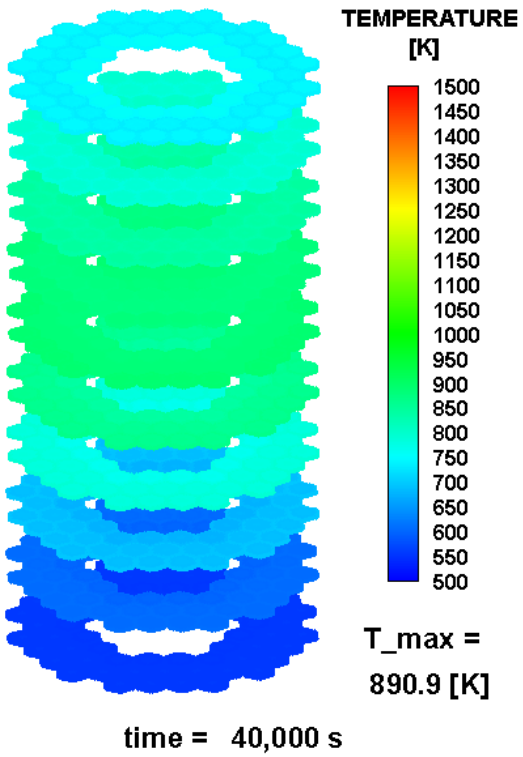

Figure 6.8 RELAP P-LOFC Fuel Temperature Distribution at the End of the Core Heat-up Phase

Although peak and average fuel temperature still appear to be under predicted as compared to previous P-LOFC results, a general transient temperature trend similar to that observed for the whole core simulation is seen here also. Reverse flow through the reactor core removes heat from lower portions to higher core elevations. During this core heat-up phase, helium is continuously removing heat from lower elevations and depositing it at higher elevations until the top of the core reaches a maximum. When this occurs and fuel temperatures have not exceeded their failure temperature (1600^{o}C), the cool-down or safe-shutdown phase of the transient begins. Figure 6.9 shows the fuel temperature distribution during the safe-shutdown phase.

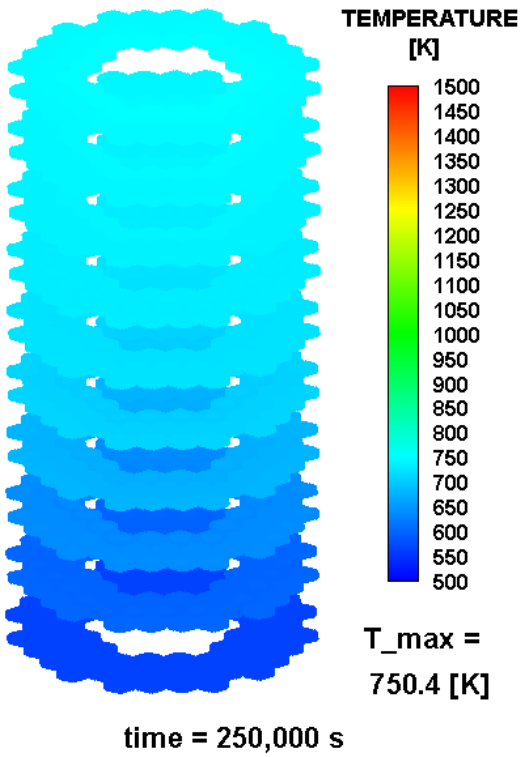

Figure 6.9 RELAP P-LOFC Fuel Temperature Distribution during the Safe-Shutdown Phase

From Figures 6.6 through 6.9, it is clear that for the presented fuel and MHTGR models, fuel temperatures are well below any failure or safety thresholds. This is expected for the P-LOFC simulation since helium recirculation is strong at elevated pressures. It should be noted however that there are several aspects inherent to any RELAP fuel assembly model that may contribute to the under-prediction of fuel temperatures. These primarily include: (1) modeling a limited number of fuel pins by averaging pin-powers to conserve total core power, and (2) the neglecting of core-level heat transfer effects such as inter-assembly heat conduction across bypass gaps. While for the P-LOFC simulation this is not as dire, the D-LOFC simulation may require or demand a different core transient tool than RELAP. Results for the D-LOFC simulation using the presented RELAP model are discussed in the next section.

6.4 RELAP D-LOFC Simulation Results

Similar to the P-LOFC simulation, the same steady state temperature distribution is reached at 20,000 s. All of the other transient and model parameters are the same for D-LOFC except that a break junction and volume are introduced. A large break area is introduced on the cross-duct. The break area/size, orientation, and location are not as important for HTGRs as they are for LWRs. For LWRs, these parameters will determine how much coolant is lost and the time to fuel failure can vary significantly. For the HTGR, pressure reaches equilibrium with the containment volume quickly. Containment design will be critical for the HTGR to maintain as much pressure as possible in the vessel.

The LOFC accident initiates in the same manner as for the P-LOFC with exception of a break and break volume held at a constant pressure (1 MPa). Figure 6.10 shows the energy balance over time for the D-LOFC.

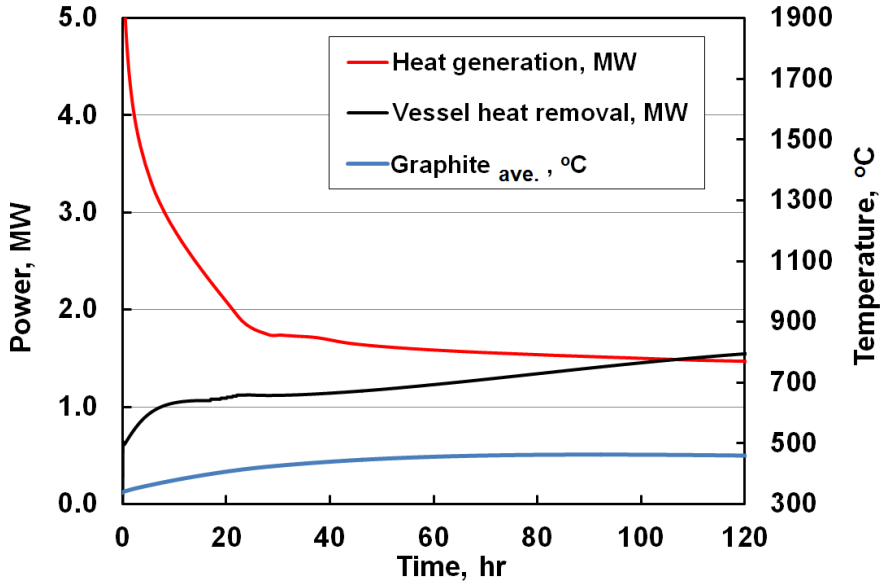

Figure 6.10 RELAP D-LOFC Transient Energy Balance

One key difference between the RELAP results in Figure 6.10 and those presented in Figure 5.8 is that the time required for the RCCS heat removal to surpass heat generation is much longer, *i.e.*, 108 hrs. This is principally due to the lack of adequate heat

redistribution into large inner and outer reflector block regions. This is different for the RELAP P-LOFC simulation because in that scenario, there is enough recirculation and mixing in the upper and lower plenums to distribute heat quickly. For the D-LOFC scenario, there is minimal recirculation. In reality, heat will be redistributed into these reflector block regions due to heat conduction across gap spaces which is absent in the RELAP fuel models. As the core heats-up, some minor recirculation flow develops and heat is slowly redistributed into the upper core region. Figure 6.11 shows the core temperature over time.

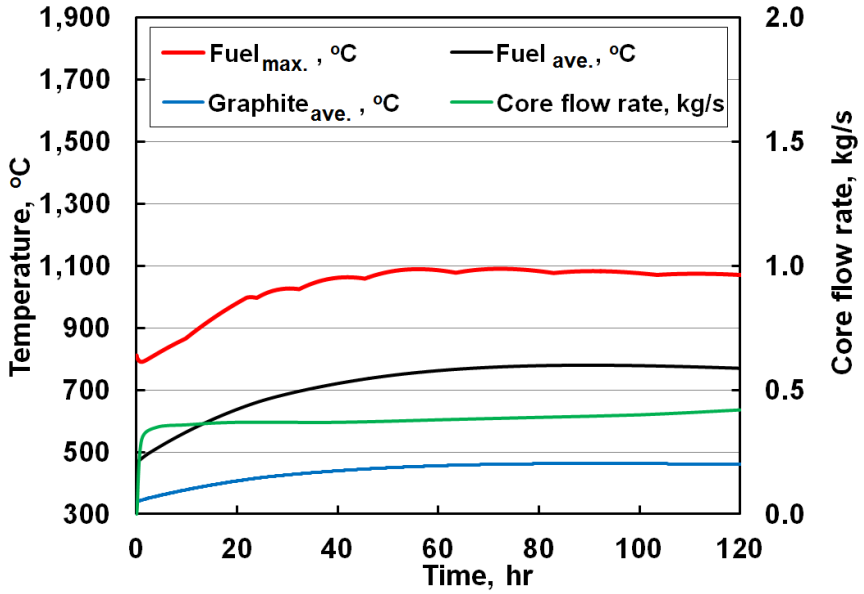

Figure 6.11 RELAP D-LOFC Core Peak and Average Temperatures

From Figure 6.10 and 6.11, it can be seen that the core heat-up phase lasts until about t = 108 hrs. Peak temperatures gradually level off as some recirculation begins to develop within the vessel. Average graphite temperatures remain low because the inner and outer graphite reflector blocks do not absorb core heat as expected. Graphite temperatures in the active core region are near the average fuel temperature shown in Figure 6.11. For reasons similar to those discussed for the P-LOFC RELAP simulation, peak fuel temperatures do not appear to approach any fuel failure temperature limit. Fuel

temperatures at the end of the core heat-up phase for the D-LOFC are shown in Figure 6.12.

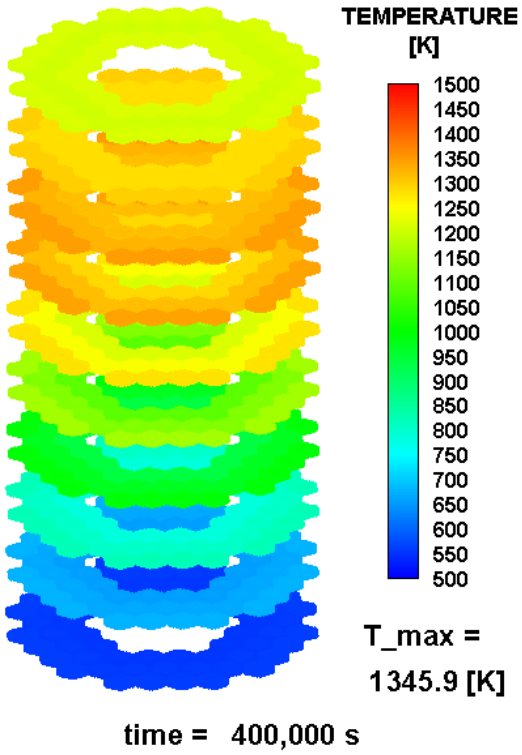

Figure 6.12 RELAP D-LOFC Fuel Temperature Distribution at the End of the Core Heat-up Phase

After the core heat-up phase, the vessel heat removal out-paces the heat generation. Consequently, the average fuel and graphite temperatures begin to decrease from those observed in Figure 6.12. Figure 6.13 shows the late-term D-LOFC fuel temperature distribution during the safe shut-down phase.

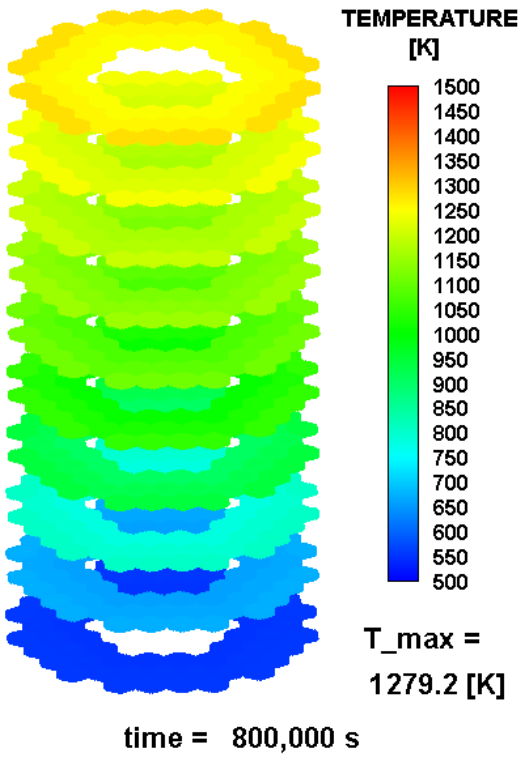

Figure 6.13 RELAP D-LOFC Fuel Temperature Distribution during the Safe Shut-down Phase

While the RELAP D-LOFC results appear acceptable from a safety standpoint, there are concerns about the RELAP fuel modeling capabilities for HTGRs. Some of these concerns have been discussed throughout this chapter. A list of these shortcomings and their importance is outlined in Table 6.1.

Table 6.1. RELAP HTGR, LOFC Modeling Concerns

#	Description	Importance*
1.	Limited number of fuel heat structures, requires pin-power averaging, leads to lower peak fuel temperatures	**High**
2.	Heat transfer coupling between assembly blocks at the core-level is difficult to adequately capture, leads to non-physical heat isolation within active fuel assemblies, can contribute to overly long transients	**High**
3.	Accurate core power distribution is needed prior to any averaging, to compute peak fuel temperatures	**Medium**
4.	Due to low gravitational flow potential during a D-LOFC, friction factor correlations and other flow resistances should be carefully selected to match expected conditions	**Medium**
5.	Hexagonal assembly geometry is not a standard heat structure model option	**Medium**
6.	RCCS heat removal from vessel wall is difficult to implement with existing heat structure boundary condition options	**Low**
7.	Careful modeling of vessel volumes, in particular the elevation values, is required	**Low**
8.	Matching boundary conditions beyond the vessel wall (*i.e.*, containment or environment) will introduce additional modeling concerns such as developing a detailed and accurate RELAP RCCS model as well as capturing non-RCCS heat transfer to the environment and other structures	**Low**

*This is estimated, qualitative importance based on the presented RELAP results and those shown in the literature using CFD, experiments, or other reliable data source for the particular factor or phenomenon

For the RELAP simulations presented in here, Item 5 in Table 6.1 was mitigated by introducing an advanced slab fuel model that better matches the hexagonal geometry than the equivalent cylinder model. This also partially alleviated Item 1 as more unique

fuel compacts were modeled. However, 210 fuel compacts is still much smaller than the 100,000+ fuel compacts that are all modeled using the whole core methods developed in this study. Item 3 was directly eliminated in the presented RELAP model by using a detailed, realistic, coupled thermal-hydraulic neutronic power distribution.

Remaining concerns pertinent to the RELAP model and results presented here and most if not all other HTGR RELAP simulations are Items 1, 2, 4 and 6 through 8. Items 1 and 2 are the most important since the P- and D-LOFC transient results are clearly impacted when compared to the results in Chapter 6, which relies on a more robust fuel and whole-core model. Item 4 can be mitigated by accurately specifying the friction factor correlation to use for each hydrodynamic volume if it is determined that the standard RELAP values are incorrect. Items 6 through 8 could be critical for overly simplified models but are ultimately judged to be of low importance since HTGR vendors will likely devote significant resources toward developing a computational model for their specific RCCS and containment design.

7. CONCLUSIONS

A new transient thermal hydraulic method for simulating prismatic HTGRs during a loss-of-forced-circulation accident either pressurized (P-LOFC) or depressurized (D-LOFC) was described in this study. The work presented here extends the steady state HTGR thermal hydraulic work published in Huning (2014), Connolly *et al.* (2016), Huning *et al.* (2016), and others. The principal contributions include: (1) a well-documented transient fluid method and implementation, (2) consideration of vessel volumes such as the upper plenum, lower plenum, and riser channel, (3) RCCS heat removal from the vessel wall, (4) transient heat generation, and (5) the corresponding transient initial and boundary conditions for the P- and D-LOFC accident scenarios.

New HTGR safety methods are needed because exiting methods either cannot model the whole core (CFD) or do not model fuel assembly with appropriate fidelity (homogenized unit cell and porous media techniques). A commonly used nuclear industry safety analysis code, RELAP5-3D, is investigated here for HTGR LOFC analysis. However, much like the other LOFC analyses in the literature, significant fuel modeling concerns lead to under-predicted fuel temperatures, and overly long transient simulations. Many improvements could be made, however, to improve RELAP for simulating LOFC accidents.

The whole core transient thermal hydraulic method developed here addresses two key concerns with existing methods: (1) computes whole-core temperature distributions, and (2) models the fuel assembly blocks in complete detail with every fuel-pin being modeled. This allows for critical key core-level transient phenomena, including heat redistribution and bypass flow, to be simulated. This also allows for detailed fuel assembly temperature distributions to be calculated, which retains accurate peak temperature estimations.

One other important aspect of the method developed here is the inclusion of a detailed, realistic core power distribution determined from a coupled thermal hydraulic and neutronics analysis. This power distribution affects the locations of the transient peak fuel temperatures. It also affects the initial temperature distribution that governs the heat redistribution after reactor SCRAM and ultimately the peak fuel temperatures over the transient.

Other important aspects of the newly developed model include the methods for RCCS heat removal estimation and the treatment of transient heat generation. Based on RCCS experiment data published in the literature, it is determined that RCCS heat removal is primarily a function of vessel wall temperature. This assumption neglects any thermal capacitance within the containment gas space and containment structures. For sufficiently long transients, this is an appropriate assumption. For heat generation, the supplied initial power distribution governs the heat generation in each fuel compact. The total core power as a function of time is determined from an ANSI decay heat curve for low-enriched UO_2 fuel. This is also a valid assumption considering that the expected HTGR fuel will be composed of low-enriched UO_2 fuel.

It should be noted that this newly developed method is designed to simulate certain reactor transients, mainly the LOFC accidents, and predict if or when fuel failure occurs. It can also predict steady state temperature and flow distributions if desired. If this distribution is not determined at the start of the transient, then it must be supplied by the user.

If fuel temperatures exceed their assumed failure limit of 1600^{o}C, then the transient simulation will terminate since the method is not capable of predicting heat transfer effects due to fuel geometry changes, or geometry different than a solid cylinder due to fuel failure. Although the specific fuel compact dimensions, assembly flat-to-flat diameter, fuel-coolant pitch, coolant channel dimensions, assembly, and core heights can be changed, the triangular pitch, and cylindrical geometry of the fuel and coolant channels cannot be altered

within the present method. Only one type of fuel dimensions and two types of circular channels can be assumed. This is due to the similarity and repeated fuel assembly design used across several conceptual prismatic HTGRs.

Likewise, graphite and helium temperatures that exceed 1600°C will terminate the LOFC simulations. This is due to expected fuel failure associated with graphite and helium temperatures above 1600°C. Should fuel failure temperatures be increased (*i.e.,* due to new experimental data or regulatory justification), then material property data for fuel and graphite beyond 1600°C should be added to the existing material property data structures used in the method. This is not an inherent limit of the method but rather a numerical implementation to prevent the simulation from consuming unneeded computational resources. One important thing to note, although there is no limit within the newly developed method to what core power can be used, is that if any portion of the fuel or graphite exceeds 1600°C due to excessive power peaking or too high of core power, the simulation will terminate.

There are no restrictions on the dimensions of the other vessel volumes. There are also no inherent restrictions on time-step size, length of the transient, or when to output data. All of these parameters are selected by the user to ensure numerical stability in the output, no hardware or memory limits are breached, and are physical to the specific HTGR design under investigation.

Considering these restrictions of applicability, using this newly developed method transient results including whole-core fuel temperature distributions were computed and discussed for the two key design basis accidents for the HTGR, namely the P-LOFC and D-LOFC accidents. The reactor design of interest is the MHTGR-350, since it has the most openly published design documents and initial LOFC analysis data.

The LOFC results confirm the preeminent safety design feature of HTGRs, which is that in the event of an SBO and a large coolant break, the reactor can safely shutdown to a safe temperature without the need for any active safety systems or operator actions. This

is a generational safety improvement over existing LWR designs including Gen 3+ systems such as the AP-1000 by Westinghouse, which require operator action or forced circulation after ~3 days. For LWRs such the Fukushima BWR Mark-1, this time till operator action is required can be as short as 6-8 hours after the initiating event. For the HTGR, a similar accident will not require any operator action or active system at any time.

The improvements associated with the method developed here over conventional safety analysis methods are clearly observed when similar RELAP5-3D simulations are conducted. Despite the noted fuel modeling improvements (advanced slab model) over conventional fuel models (equivalent cylinder models), there are still some irregularities in the results, which indicate or highlight the drawbacks of many existing safety analysis methods for HTGRs. These irregularities principally include: (1) during the P-LOFC, the recirculation flow rate may be too strong leading to an over estimation of RCCS heat removal and reduced peak fuel temperature, (2) during the D-LOFC, heat transfer into the reflector block regions, in the absence of any significant helium recirculation, is lower than expected, and (3) during the D-LOFC, the safe-shutdown phase does not being until very late into the transient. All three of these irregularities can be traced back to one of two factors, either or both of: (a) inadequate heat transfer estimations into the reflector assemblies and between fuel assemblies at the core-level, or (b) pin-power averaging leading to lower predicted peak fuel temperatures.

There are other minor factors associated with using RELAP to simulate LOFC accidents; however, these are judged to be of only medium or low importance. It is expected that HTGR vendors could rectify these minor factors in preparation for design certification. The major factors discussed above, (a) and (b), are unlikely to be remedied with current RELAP or similar method capabilities.

Despite the improvements over RELAP and other methods cited in the literature, there are many possible improvements which could be made to the method developed in this study as well. Of course, without experimental data using the current prismatic HTGR

fuel assembly design, it is difficult to quantitatively estimate the magnitude each improvement could bring to the overall method. A list of some potential future method improvements is shown in Table 7.1.

Table 7.1 Potential Improvements for the Presented Method

#	Description	Importance*
1.	Improve the riser channel heat transfer from the core barrel to the vessel wall	**High**
2.	Develop a containment model that would provide more accurate boundary conditions for the D-LOFC accident	**High**
3.	Add additional vessel volumes (the SCS) to provide more gravitational potential for natural recirculation	**Medium**
4.	Develop heat transfer models for other regions of the vessel like the vessel upper and lower head	**Medium**
5.	Develop a specific RCCS model similar to those described in the literature	**Low**
6.	Develop capabilities for additional fluids such as air, CO_2, and N_2 for the possibility that the containment breaks or is not filled with helium	**Low**
7.	Include a fuel swelling/fuel performance model to more accurately capture the fuel temperature profile	**Low**

* Like Table 6.1, this is estimated, qualitative importance based on the diverse information presented in the literature

All of the items except for Item 7 in Table 7.1 should only act to reduce the peak temperatures presented in Chapter 5. The first two items could be exceedingly difficult without a reference design to use as a template. For the MHTGR-350 and other HTGR designs, it is not clear in the literature what the particular riser geometry and containment geometry will be. Starting from scratch, it could take several design iterations to optimize the containment and riser design. These tasks have similar design tradeoffs common to the design of any other reactor system or component. While an arbitrary or initial design guess

could be made, if it is too conservative, an unrealistic or a very high peak fuel temperature could be predicted during LOFC accident simulations.

Items 3 and 4 are not expected to be as difficult but it is unlikely that they would contribute significantly to vessel heat removal. The dominant heat transfer area between the vessel and the RCCS is the vessel wall connected to the riser channel, which is already modeled.

Items 5 and 6 are aspects that would be desirable to have but do not improve the accuracy under the current modeling assumptions. Including an RCCS model would allow for additional accidents to be considered where the RCCS or containment could be impacted. Including non-helium coolant models would allow for additional accidents where the containment could be broken. It would also allow for containment designs with non-helium environments.

It should be noted that all of the items except for Item 7 are not related to the fuel or core model. Although it is unlikely that fuel performance effects such as swell/shrink would appreciably alter the fuel temperature profiles, this is the only significant improvement that could be made to the core and fuel model without going to finer unit-cell mesh like that of a CFD calculation. Considering this along with the fact that there are still several open modeling issues related to the vessel-RCCS heat transfer and fluid volumes, it may be advantageous at a later date to couple the fuel and core model to a CFD model of the vessel, containment, and RCCS. This would not be too enterprising since the core requires significantly more modeling detail than these other volumes and materials. A whole-core CFD model is not possible without homogenizing or simplifying the core geometry. However, CFD models for the lower plenum, upper plenum, and other regions have been demonstrated. One of the best possible outcomes of the work presented in this dissertation would be for the core modeling methodology to be adapted into a large computational scheme including CFD for the other vessel and associated volumes. Given

the complex nature of the prismatic HTGR core, this is the most logical path toward establishing a method for design basis safety calculations and licensing the HTGR.

APPENDIX A – REACTOR MATERIAL PROPERTIES, FROM JOHNSON ET AL. (2009)

Table A.1 Fuel Compact Thermal Conductivity

Temperature [ºC]	k [W/m-K]
300	4.62
400	4.98
500	5.33
600	5.69
700	6.08
800	6.41
900	6.77
1000	7.13
1100	7.49
1200	7.85
1300	8.21
1400	8.57
1500	8.93
1600	9.29
1700	9.55

Table A.2 Fuel Compact Fuel Heat Capacity

Temperature [ºC]	$\rho \cdot C_P$ [J/m^3-K]
300	1.3886e6
400	1.3886e6
500	1.3886e6
600	1.5965e6
700	1.7853e6
800	1.8929e6
900	1.9646e6
1000	2.0196e6
1100	2.0530e6
1200	2.0793e6
1300	2.1032e6
1400	2.1247e6
1500	2.1247e6
1600	2.1247e6
1700	2.1247e6

Table A.3 Graphite Thermal Conductivity

Temperature [°C]	k [W/m-K]
300	29.0
800	29.0
900	29.5
1000	30.8
1100	32.4
1200	34.1
1300	35.8
1400	37.4
1500	37.4
1600	37.4
1700	37.4

Table A.4 Graphite Heat Capacity

Temperature [°C]	$\rho \cdot C_P$ [J/m^3-K]
300	1.3015e6
400	1.7487e6
500	2.1106e6
600	2.4029e6
700	2.6326e6
800	2.8153e6
900	3.0659e6
1000	3.1529e6
1100	3.2190e6
1200	3.2729e6
1300	3.3182e6
1400	3.3565e6
1500	3.3565e6
1600	3.3565e6
1700	3.3565e6

Table A.5 Stainless Steel 304 Thermal Conductivity

Temperature [K]	k [W/m-K]
50	17.77
473	17.77
573	19.37
673	20.82
723	18.25
773	19.02
823	19.8
873	20.58
923	21.37
973	22.21
1023	23.03
107	23.83
1123	24.63
1173	25.45
1223	26.28
1273	27.12
1323	27.97

Table A.6 Stainless Steel 304 Heat Capacity

Temperature [^{o}C]	$\rho \cdot C_P$ [J/m^3-K]
50	4.205E+06
473	4.205E+06
573	4.349E+06
673	4.440E+06
723	4.476E+06
773	4.512E+06
823	4.551E+06
873	4.593E+06
923	4.635E+06
973	4.676E+06
1023	4.717E+06
1073	4.758E+06
1123	4.798E+06
1173	4.838E+06
1223	4.877E+06
1273	4.915E+06
1323	4.952E+06

APPENDIX B – RELAP POWER DISTRIBUTION

The power distribution is determined by computing the fraction of core fuel modeled within the fuel heat structures. See Section 6.1 for a description of the averaging method. The power factors given in Tables B.1 through B.3 add to 100% or 1. They are intended to be multiplied by the total core power given at some time after shutdown, during the transient.

Table B.1 Inner Fuel Ring Power Factors

Axial Node	HS 1124	HS 1125	HS 1127	HS 1128
1	1.3236E-03	2.2061E-03	1.3236E-03	2.9414E-04
2	1.8365E-03	3.0609E-03	1.8365E-03	4.0812E-04
3	2.5545E-03	4.2576E-03	2.5546E-03	5.6768E-04
4	3.8047E-03	6.3412E-03	3.8047E-03	8.4550E-04
5	6.2638E-03	1.0440E-02	6.2639E-03	1.3920E-03
6	9.7799E-03	1.6300E-02	9.7801E-03	2.1733E-03
7	1.2026E-02	2.0044E-02	1.2026E-02	2.6725E-03
8	1.2075E-02	2.0126E-02	1.2075E-02	2.6834E-03
9	1.0560E-02	1.7600E-02	1.0560E-02	2.3467E-03
10	8.7481E-03	1.4580E-02	8.7482E-03	1.9441E-03

Table B.2 Center Fuel Ring Power Factors

Axial Node	HS 1144	HS 1145	HS 1147	HS 1148
1	1.5090E-03	2.5149E-03	1.5090E-03	3.3533E-04
2	2.0523E-03	3.4206E-03	2.0524E-03	4.5608E-04
3	2.8677E-03	4.7796E-03	2.8678E-03	6.3728E-04
4	4.3316E-03	7.2195E-03	4.3317E-03	9.6260E-04
5	7.5879E-03	1.2647E-02	7.5880E-03	1.6862E-03
6	1.3340E-02	2.2234E-02	1.3341E-02	2.9646E-03
7	1.6952E-02	2.8253E-02	1.6952E-02	3.7671E-03
8	1.7080E-02	2.8467E-02	1.7080E-02	3.7956E-03
9	1.4925E-02	2.4876E-02	1.4925E-02	3.3168E-03
10	1.2211E-02	2.0351E-02	1.2211E-02	2.7135E-03

Table B.3 Outer Fuel Ring Power Factors

Axial Node	HS 1174	HS 1175	HS 1177	HS 1178
1	1.4183E-03	2.3639E-03	1.4183E-03	3.1519E-04
2	1.9400E-03	3.2333E-03	1.9400E-03	4.3111E-04
3	2.7095E-03	4.5159E-03	2.7095E-03	6.0212E-04
4	4.0979E-03	6.8299E-03	4.0980E-03	9.1066E-04
5	7.3551E-03	1.2259E-02	7.3552E-03	1.6345E-03
6	1.3795E-02	2.2991E-02	1.3795E-02	3.0655E-03
7	1.7786E-02	2.9644E-02	1.7786E-02	3.9525E-03
8	1.7927E-02	2.9878E-02	1.7927E-02	3.9837E-03
9	1.5653E-02	2.6088E-02	1.5653E-02	3.4784E-03
10	1.2630E-02	2.1049E-02	1.2630E-02	2.8066E-03

REFERENCES

1. Anderson, N., Y. Hassan and R. Schultz, *Analysis of the Hot Gas Flow in the Outlet Plenum of the Very High Temperature Reactor Using Coupled RELAP5-3D System Code and a CFD Code*, Nuclear Engineering and Design, 2008, **238**, p. 274-279.
2. ANSYS Inc., *CFX11: User Manual*, 2006.
3. August, J.K., and J.J. Hunter, *Relicensing Fort St. Vrain: How the HTGR Design Basis Was Rediscovered*, Proceedings of the 4th International Topical Meeting on High Temperature Reactor Technology, 2008, (HTR2008-58030).
4. Ball, S. J., *MORECA: A Computer Code for Simulating Modular High-Temperature Gas-Cooled Reactor Core Heat Accidents*, Oak Ridge National Laboratory, NUREG/CR-5712, 1991.
5. Ball, S. J., *Next Generation Nuclear Plant Phenomena Identification and Ranking Tables (PIRTS)*, U.S. NRC., NUREG/CR-6944, Vol. 2, 2008.
6. Bieder, U., and E. Graffard, *Qualification of the CFD Code Trio_U for Full Scale Reactor Applications*, Nuclear Engineering and Design, 2008, **238**, p. 671-679.
7. Cavalier, C., et al., *Presentation of the HTR neutronics code system NEPHTIS,* Societe Francaise d'Energie Nucleaire (SFEN), INIS-FR-4515, 2006.
8. CD-adapco, *Star-CD Version 4.14*, 2014.
9. CD-adapco, *STAR-CCM+ Version 3.06*, 2008.
10. Churchill, S.W., *Comprehensive Correlating Equations For Heat, Mass and Momentum Transfer in Fully Developed Flow in Smooth Tubes,* Industrial & Engineering Chemistry Fundamentals, **16**(1), p. 109-116.
11. Cioni, O., M. Marchand, G. Geffraye, and F. Ducros, *3D Thermal-Hydraulic Calculations of a Modular Block-Type HTR Code*, Nuclear Engineering and Design, 2006, **236**, p. 565-573.
12. Connolly, K.J., A.J. Huning, F. Rahnema, and S. Garimella, *A Coarse Mesh Coupled Neutronics and Thermal Fluids Method for Prismatic Cores*, Nuclear Technology, 2016 (*accepted*).
13. Damian, F., *VHTR Core Preliminary Analysis Using NEPHTIS3 / CAST3M Coupled Modelling*, 4th International Topical Meeting on High Temperature Reactor Technology, HTR 2008, September 28, 2008 - October 1, 2008, Washington, DC, United states.
14. Electric Power Research Institute (EPRI), *MAAP4 Applications Guidance: Desktop Reference for Using MAAP4 Software, Revision 2*, 2010.
15. FLUENT Inc., *FLUENT Version 6.2.16*, 2005.

16. Frisani, A., and Y.A. Hassan, *Computation Fluid Dynamics Analysis of the Reactor Cavity Cooling System for Very High Temperature Gas-Cooled Reactors*, Annals of Nuclear Energy, 2014, **72**, p. 257-267.

17. Futterer, M.A., et al., *Raphael: The European Union's (Very) High Temperature Reactor Technology Project*, American Nuclear Society Embedded Topical Meeting - 2006 International Congress on Advances in Nuclear Power Plants, ICAPP'06, June 4, 2006 - June 8, 2006, Reno, NV, United states.

18. Gauntt, R. O., et al., *MELCOR Computer Code Manuals*, Sandia National Laboratories, NUREG/CR-6119, Rev. 2, 2000.

19. General Atomics, *Gas Turbine-Modular Helium Reactor (GT-MHR) Conceptual Design Description Report*, Report No. 910720, 1996.

20. Haque, H., *Consequences of Delayed Air Ingress Following a Depressurization Accident in a High Temperature Reactor,* Nuclear Engineering and Design, 2007, **238**, p. 3041-3046.

21. Huning, A.J., *A Steady State Thermal Hydraulic Analysis Method for Prismatic Gas Reactors*, Georgia Institute of Technology, Masters of Science, 2014.

22. Huning, A.J., S. Garimella, and F. Rahnema, *A Steady-State Thermal-Hydraulic Analysis Method for Prismatic High-Temperature Gas-Cooled Reactors*, Nuclear Technology, 2016, **193**, p. 234-246.

23. Idaho National Engineering and Environmental Laboratory, *RELAP5-3D Code Manual*, INEEL/EXT-98-00834 Rev. 2.1, 2003.

24. Johnson, R.W., *Modeling Strategies for Unsteady Turbulent Flows in the Lower Plenum of the VHTR*, Nuclear Engineering and Design, 2008, **238**, p. 482-491.

25. Johnson, R.W. and ASME, *Development of a CFD Analysis Plan for the First VHTR Standard Problem*, American Society of Mechanical Engineers, 2009, New York.

26. Johnson, R. W., Sato, H. and Schultz, R. R., *CFD Analysis of Core Bypass Phenomena*, INL/EXT-09-16882, 2009, Idaho National Laboratory.

27. Karaismail, E. and I. Celik, *Numerical and Modeling Issues in Application of CFD to Flow in a Simplified Plenum Relevant to a Prismatic VHTR*, Nuclear Engineering and Design, 2010, **240**, p. 2011-2022.

28. Kim, S., N.-I. Tak, H.-S. Lim, and S.-J. Ha, *Sensitivity Study on Depressurized LOFC Accidents with Failure of RCCS in a Modular Gas-Cooled Reactor*, Annals of Nuclear Energy, 2010, **37**, p. 664-671.

29. Kim, M.H., H.S. Lim and W.J. Lee, *A Thermal-Fluid Assessment of a Cooled-Vessel Concept for a VHTR*, Nuclear Engineering and Design, 2008, **238**, p. 3360-3369.

30. Kissane, M.P., *A Review of Radionuclide Behavior in the Primary System of a Very-High-Temperature-Reactor*, Nuclear Engineering and Design, 2009, **239**, p. 3076-3091.

31. LaBar, M.P., A.S. Shenoy, W.A. Simon, and E.M. Campbell, *Introducing the GT-MHR*, Nuclear Engineering International, 2004, March Issue, p. 19-23.

32. Limaiem, I., F. Damian, X. Raepsaet, and E. Studer, *Very High Temperature Reactor Physics Studies using a 3D Neutronic / Thermal-hydraulics Coupling System for Block Type Gas Cooled Reactors*, PHYSOR-2006 – American Nuclear Society's Topical Meeting on Reactor Physics, Vancouver, BC, Canada, 2006. September 10-14.

33. Lommers, L.J., B.E. Mays, and F. Shahrokhi, *Passive heat removal impact on AREVA HTR design*, Nuclear Engineering and Design, 2014, **271**, p. 569-577.

34. Lommers, L.J., F. Shahrokhi, J.A. Mayer and F.H. Southworth, *AREVA HTR Concept for near-Term Deployment*, Nuclear Engineering and Design, 2012, **251**, p. 292-296.

35. MacDonald, P.E., *NGNP Preliminary Point Design – Results of the Initial Neutronics and Thermal-Hydraulic Assessments*, INEEL/EXT-03-00870 Rev. 1., 2003, Idaho National Engineering and Environmental Laboratory.

36. Matrineau, R.C., and R.A. Berry, *The pressure-corrected ICE finite element method for compressible flows on unstructured meshes,* Journal of Computational Physics, 2004, **198**, p. 659 – 685.

37. McCreery, G.E. and K.G. Condie, *Experimental Modeling of VHTR Plenum Flows During Normal Operation and Pressurized Conduction Cooldown*, Idaho National Laboratory, INL/EXT-06-11760, 2006.

38. *MCNP4B: Monte Carlo N-Particle Transport Code System*, contributed by Los Alamos National Laboratory and distributed as CCC-660 by Oak Ridge National Laboratory, 1997.

39. McVay, K.L., J.-H. Park, S. Lee, Y. A. Hassan, and N.K. Anand, *Preliminary Tests of Particle Image Velocimetry for the Upper Plenum of a Scaled Model of a Very High Temperature Gas Cooled Reactor*, Progress in Nuclear Energy, 2015, **83**, p. 305-317.

40. NGNP Industry Alliance, *NGNP Industry Alliance Announces Nuclear Technology Selection of AREVA Prismatic Block Modular Reactor Design*, Press Release, 2012.

41. NGNP Moisture Ingress Assessment Committee, *Assessment of NGNP Moisture Ingress Events*, Idaho National Laboratory, INL/EXT-11-21397, 2011.

42. Oh, C. H., G. C. Park, C. Davis, *RCCS Experiments and Validation for High-Temperature Gas-Cooled Reactor*, Nuclear Technology, 2009, **167**, p. 107-117.

43. Oh, C.H., and E.S. Kim, *Isothermal Air Ingress Validation Experiments at Idaho National Laboratory: Description and Summary of Data*, Idaho National Laboratory,INL/EXT-10-19727, 2010.

44. Oh, C.H., and E.S. Kim, *Air-Ingress Analysis: Part I. Theoretical Approach*, Nuclear Engineering and Design, 2010, **241**, p. 203-212.

45. Oh, C.H., H.S. Kang, and E.S. Kim, *Air-Ingress Analysis: Part II. Computational Fluid Dynamics Models*, Nuclear Engineering and Design, 2011, **241**, p. 213-225.

46. Rodriguez, S.B. and M.S. El-Genk, *Numerical Investigation of Potential Elimination of 'Hot Streaking' and Stratification in the VHTR Lower Plenum Using Helicoid Inserts*, Nuclear Engineering and Design, 2010, **240**, p. 995-1004.

47. Ryskamp, J. M., *Next Generation Nuclear Plant High-Level Functions and Requirements*, Idaho National Engineering and Environmental Laboratory, INEEL/EXT-03-01163, 2003.

48. Salko, R. K., and M. N. Avramova, *COBRA-TF Subchannel Thermal-Hydraulics Code (CTF) Theory Manual: Revision 0*, Pennsylvania State University, CASL-U-2015-0054-000, 2015.

49. Sandia National Laboratories, Sierra/Fuego 2.7 User's Manual, SAND 2006 6084P, 2008.

50. Sato, H., R. Johnson, and R. Schultz, *Computational Fluid Dynamic Analysis of Core Bypass Flow Phenomena in a Prismatic VHTR*, Annals of Nuclear Energy, 2010, **37**, p. 1172-1185.

51. Sato, H., et al., *Transient Analysis of Depressurized Loss-of-Forced-Circulation Accident Without SCRAM in High-Temperature Gas-Cooled Reactor*, Nuclear Technology, 2013, **185**, p.227-238.

52. Shenoy, A.S., D.W. McEachern, *HTGR Core Thermal Design Methods and Analysis*, General Atomics, GA-A12985, 1974.

53. Studer, E., et al., *CAST3M/ARCTURUS: A coupled heat transfer CFD code for thermal–hydraulic analyzes of gas cooled reactors*, Nuclear Engineering and Design, 2007, **237**, p. 1814–1828.

54. T.A.C Technologies, *NEVADA Software Package Quick Reference Series*, T.A.C. Technologies USA, 2000.

55. Tak, N.-I., M.-H. Kim, and W. J. Lee, *Numerical Investigation of a Heat Transfer within the Prismatic Fuel Assembly of a Very High Temperature Reactor*, Annals of Nuclear Energy, 2008, **35**, p. 1892-1899.

56. Thielman, J., P. Ge, Q. Wu and L. Parme, *Evaluation and Optimization of General Atomics' GT-MHR Reactor Cavity Cooling System Using an Axiomatic Design Approach*, Nuclear Engineering and Design, 2005, **235**, p. 1389-1402.

57. Todreas, N. E., and M. S. Kazimi, *Nuclear Systems II: Elements of Thermal Hydraulic Design*, 0th Edition, Taylor and Francis, ISBN 1560320796, 2001.

58. Tsvetkov, P.V., *"Used fuel" Vectors and Waste Minimization Strategies for VHTRs Operating Without Refueling*, Nuclear Engineering and Design, 2010, **240**, p. 2458-2465.

59. U.S. Department of Energy, *Preliminary Safety Information Document for the Standard MHTGR*, DOE Report HTGR-86-024, Vol. 1, 1986.

60. U.S. Nuclear Regulatory Commission, *TRAC-M/FORTRAN 90(Version 3.0) Theory Manual*, U.S. NRC, NUREG/CR-6724, 2001.

61. U.S. Nuclear Regulatory Commision, *Regulatory Guide 1.200: An Approach for Determining the Technical Adequacy of Probabilistic Risk Assessment Results for Risk-Informed Activities,* U.S. NRC*,* Office of Nuclear Regulatory Research, 2009.

62. Vaghetto, R., C. Luigi, Y. A. Hassan, *Experimental Study of the Effect of Graphite Dispersion on the Heat Transfer Phenomena in a Reactor Cavity Cooling System*, Nuclear Technology, 2012, **177**, p. 217-230.

63. Vaghetto, R. and Y.A. Hassan, *Experimental Investigation of a Scaled Water-Cooled Reactor Cavity Cooling System*, Nuclear Technology, 2014, **187**, p. 282-293.

64. Vaghetto, R. and Y.A. Hassan, *Modeling the Thermal-Hydraulic Behavior of the Reactor Cavity Cooling System Using RELAP5-3D*, Annals of Nuclear Energy, 2014, **73**, p. 74-83.

65. Wang, H.H., E. Dominguez-Ontiveros, and Y.A. Hassan, *Computational Fluid Dynamics Analysis of Core Bypass Flow and Crossflow in a Prismatic Very High Temperature Gas-Cooled Nuclear Reactor Based on a Two-Layer Block Model*, Nuclear Engineering and Design, 2014, **268**, p. 64-76.

66. Williams, P.M., T.L. King, and J.N. Wilson, *Draft Preapplication Safety Evaluation Report for the Modular High-Temperature Gas-Cooled Reactor,* U.S. NRC, NUREG-1338, 1989.

67. Yanhua, Z., S. Lei, and W. Yan, *Water-Ingress Analysis for the 200 MWe Pebble-bed Modular High Temperature Gas-Cooled Reactor*, Nuclear Engineering and Design, 2010, **240**, P. 3095-3107.

68. Zhang, Z., Y. Dong, and W, Schere, *Assessments of Water Ingress Accidents in a Modular High Temperature Gas Cooled Reactor,* Nuclear Technology, 2005, **149**, p. 253-264.